Università di Firenze, Università di Perugia, INdAM consorziate nel CIAFM

DOTTORATO DI RICERCA
IN MATEMATICA, INFORMATICA, STATISTICA

CURRICULUM IN MATEMATICA
CICLO XXXVII

Sede amministrativa Università degli Studi di Firenze
Coordinatrice Prof.ssa Alessandra Sestini

Spectral Collocation Methods for Two-Dimensional non-Newtonian Flows

Settore Scientifico Disciplinare MATH-04/A

Dottorando:
Antonio Giovinetto

Tutore
Prof. Lorenzo Fusi

Coordinatrice
Prof.ssa Alessandra Sestini

Anni 2021/2023

Contents

List of Figures

List of Tables

Abstract

This dissertation is organized into an introductory chapter followed by two research articles that form its core. Both contributions focus on incompressible non-Newtonian fluids, studied through mathematical models and high-accuracy numerical techniques (Spectral Collocation Methods), with particular attention to fluids exhibiting viscoplastic and piezo-viscous behavior.

In Chapter 2, the study focuses on the flow of regularized viscoplastic fluids—specifically of Bingham and Casson type—inside symmetric planar channels. A spectral collocation method is developed using a velocity–stress–pressure formulation. Compared to conventional finite element or finite volume approaches, this method combines low computational cost with high accuracy. Numerical tests, including comparisons with semi-analytical lubrication solutions, confirm the reliability of the approach. The study addresses both the generalized Stokes problem and the Navier–Stokes system in steady and unsteady regimes. The novelty lies in applying spectral collocation methods to viscoplastic fluids, an area not previously explored.

Chapter 3 deals with fluids whose viscosity explicitly depends on pressure, commonly known as piezo-viscous fluids. Such materials are relevant in geophysical, industrial, and lubrication contexts. In this model, viscosity follows an exponential law. This dependence fundamentally alters the Navier–Stokes equations.The study considers both steady and unsteady flows in 2D non-symmetric and 3D geometries, with slip boundary conditions on solid walls. Semi-analytical lubrication solutions are obtained and compared with numerical results using spectral collocation methods. The study addresses the Stokes, steady and unsteady Navier–Stokes problems in non-symmetric planar channels, as well as the Stokes and steady Navier–Stokes problems in axisymmetric cylindrical conduits. The simulations highlight the robustness of the method and the influence of both the pressure coefficient and the slip parameter on the velocity field.

Overall, these two studies contribute to the theoretical and computational understanding of non-Newtonian fluids with yield-stress or piezo-viscous characteristics. The spectral approach represents an efficient and flexible alternative to

classical discretization methods and can be adapted to a wide range of generalized Newtonian models.

1 Classification of Non-Newtonia Fluids

1.1 Introduction

The present thesis comprises a total of four chapters. The first chapter aims to provide a brief, but not exhaustive, overview of the various types of non-Newtonian fluids, while some of the non-Newtonian cases examined are discussed in the subsequent chapters. The second focuses more extensively on the article *A spectral collocation scheme for the two-dimensional flow of a regularized viscoplastic fluid: numerical results and comparison with analytical solution* ([FG24b]) and its subsequent developments. In that paper, a numerical scheme based on the spectral collocation method (SCM) is presented for the two-dimensional incompressible Stokes flow of a non-Newtonian fluid in a symmetric channel of variable width. After a suitable scaling of the governing equations and the boundary conditions, the problem is discretized, resulting in a nonlinear system that is solved via the Newton-Raphson method. The focus is on two regularized viscoplastic fluids (Bingham, Casson), but the method can be applied to any fluid in which the apparent viscosity depends on the modulus of the strain rate tensor. In the case of a small aspect ratio of the channel, the lubrication solution at the leading order is explicitly determined, and some symmetry properties are proven. The numerical scheme is validated through a comparison with the analytical solution, demonstrating excellent agreement between the latter and the numerical solution. Three types of wall functions (convergent, divergent, and non-monotone) are considered, and numerical simulations are performed for channels with a general aspect ratio. It is observed that the symmetries of the lubrication solution are maintained even when the characteristic length and width of the channel are of the same order. It has also been proven that the monotonicity of the yield surface follows that of the channel profile when the aspect ratio of the channel is "sufficiently small." This is no longer true when this hypothesis is removed. Subsequently, both the steady and unsteady Navier-Stokes problems are solved, and comparisons are made between the solutions of the steady problem and the Stokes problem as the Reynolds number increases. Thus, with the same Reynolds numbers, a comparison is made between the steady and unsteady Navier-Stokes problems.

The third chapter presents a numerical scheme based on spectral collocation methods to study the flow of a piezo-viscous fluid, i.e. a fluid in which the rheological parameters depend on pressure. This chapter is also an extension of the corresponding article *A spectral collocation scheme for the flow of a piezo-viscous fluid in ducts with slip conditions* ([FG24a]. In particular, an incompressible Navier-Stokes fluid with pressure-dependent viscosity is considered, flowing in: i) a two-dimensional non-symmetric planar channel; ii) a three-dimensional axisymmetric non-straight conduit. For both cases, Navier slip boundary conditions are imposed, which can be reduced to the classical no-slip condition with an appropriate choice of the slip parameter. The dependence of the viscosity on the pressure is assumed to be of exponential type (Barus law), although the model can be replaced by any other viscosity function. The mathematical problem (stress-based formulation) is formulated, and the governing equations are discretized using a spectral collocation scheme. The advantage of this numerical procedure, which to the authors' knowledge has never been used before for this class of fluids, lies in the ease of implementation and in the accuracy of the solution. To validate our model we compare the numerical solution with the one that can be obtained in the case of small aspect ratio, i.e. the leading order lubrication solution. Numerical simulations are performed to investigate the effects of pressure-dependent viscosity on the flow. Various wall functions are considered to gain insight into the role played by the channel/duct geometry. In both cases, (i) and (ii), it is found that an increase in the coefficient appearing in the viscosity function results in a global reduction of the flow, as physically expected. The final chapter, succinctly, describes the general and common conclusions drawn from the two previous sections and outlines some possible directions for future work. The idea is to extend the analysis to flows with complex rheology and to very general domains.

It concludes with an appendix that explicitly presents the terms of the Jacobian matrix used in the numerical Newton–Raphson algorithms implemented in MATLAB.

1.2 Classification of Non-Newtonian Fluids

In this section, without claiming exhaustiveness, we aim to classify non-Newtonian fluids, particularly focusing on incompressible fluids. A non-Newtonian fluid is one whose shear stress versus shear rate relation is nonlinear or is indeterminate at the zero shear rate (viscoplastic fluid). In the nonlinear case, it implies that the slope of the tangent to the curve, and more broadly, the apparent viscosity (the ratio between the stress modulus and the shear rate modulus), is not constant and varies due to changes in temperature, pressure, or shear rate.

A classification of non-Newtonian fluids can be provided as follows [CR11]:

1 ⧫ fluids where the local shear stress is determined solely by the local shear rate value at the given instant. These fluids are known as "time-independent," "purely viscous," "inelastic," or "generalized Newtonian fluids" (GNF);

2 ⧫ more complex fluids than the previous ones, where the relationship between shear stress and local shear rate also depends on the deformation duration and kinematic history; these are called "time-dependent" fluids;

3 ⧫ fluids with characteristics common to both ideal fluids and elastic solids, exhibiting partial elastic recovery after deformation; these are categorized as "viscoelastic fluids".

The schematization just presented following [CR11] is arbitrary since there are generally combinations of two or all three types of non-Newtonian characteristics. However, it is often possible to identify the dominant non-Newtonian mode and consider the fluid solely with that peculiarity, reducing it to one of the previous cases. Moreover, it is convenient to define an apparent viscosity for these materials, which as previously mentioned, is the ratio of the shear stress modulus to the shear rate modulus. In the following sections, we will delve into the behaviors of non-Newtonian fluids in more detail, placing particular emphasis on generalized Newtonian fluids, the subject of chapters (2) and (3).

1.3 Time-independent fluid behaviour

Given that the velocity field in Cartesian coordinates is $\mathbf{v}^{*T} = (u^*(x^*, y^*, z^*), v^*(x^*, y^*, z^*), w^*(x^*, y^*, z^*))$[1], the rate-of-strain tensor is the symmetric part of the velocity gradient, and is defined as follows:

$$\mathbb{D}^* := \frac{\nabla^*\mathbf{v}^* + \nabla^*\mathbf{v}^{*T}}{2}, \quad \left(\dot{\gamma}^* := \|\mathbb{D}^*\| = \sqrt{\frac{\mathbb{D}^* : \mathbb{D}^*}{2}}\right). \tag{1}$$

If we consider the shear stress $\mathbb{T}^*$ $\left(\tau^* := \|\mathbb{T}^*\| = \sqrt{\frac{\mathbb{T}^* : \mathbb{T}^*}{2}}\right)$, we will have the functional relationship expressible in the most general case of isotropic *viscous simple fluids* through:

$$\mathbb{T}^* = \alpha_1^*\mathbb{I} + \alpha_2^*\mathbb{D}^* + \alpha_3^*\mathbb{D}^{*2}, \tag{2}$$

where the $\alpha_k^* = \alpha_k^*(\rho^*, i_1, i_2, i_3), \quad k = 1, 2, 3$ are scalar functions depending on density ρ and the three principal invariants of $\mathbb{D}^*$ ($i_1 = \mathrm{tr}((\mathbb{D}^*); \quad i_2 = [(\mathrm{tr}(\mathbb{D}^*))^2 - \mathrm{tr}(\mathbb{D}^{*2})]/2; \quad i_3 = \det(\mathbb{D}^*)$ respectively).

In the incompressible and homogeneus case ($\nabla^* \cdot \mathbf{v}^* = \mathrm{tr}(\mathbb{D}^*) = 0$ and $\rho^* = constant$ respectively) we have the *Stokesian fluids*, where $\alpha_1^* = -p^*(\mathbf{x}^*, t^*)$ is the Lagrange multiplier due to the incompressibility constraint and $\alpha_2^* = \alpha_2^*(i_2, i_3), \quad \alpha_3^* = \alpha_3^*(i_2, i_3)$, meaning that α_2^* and α_3^* are independent of the first principal invariant of $\mathbb{D}^*$. In this case, we have the so-called *Reiner-Rivlin fluids* [TR00], where in the particular case of $\alpha_3^* = 0$, $\alpha_2^* =$ constant and $\rho^* = constant$, they define the subclass of incompressible Newtonian fluids. Generalized Newtonian fluids will be the subject of study for much of this work[2], i.e. fluid in which $i_3 = 0, \quad \alpha_1^* = -p^*, \quad \alpha_2^* = \alpha_2^*(i_2), \quad \alpha_3^* = 0$ and $\rho^* = constant$. Their constitutive law is ([AM74], [Hui15]):

$$\mathbb{T}^* = -p^*\mathbb{I} + \left[\alpha_2^*\left(-\frac{\mathrm{tr}(\mathbb{D}^{*2})}{2}\right)\right]\mathbb{D}^*. \tag{3}$$

[1] Quantities marked with "*" represent *dimensional* quantities.

[2] Many experiments on real fluids show that the nullification of the first normal stress is always accompanied by the nullification of the second; in industrial liquids (such as molten polymers) this is seldom the case [AM74]. In this discussion, we consider the very common case where $\alpha_3^* = 0$ and $\det(\mathbb{D}^*) = 0$.

More commonly, (3) is written in the following equivalent form:

$$\mathbb{T}^* = -p^*\mathbb{I} + 2\mu^*_{app}\,(\dot{\gamma}^*)\,\mathbb{D}^*, \tag{4}$$

where $\dot{\gamma}^* = \sqrt{\dfrac{\mathrm{tr}(\mathbb{D}^{*2})}{2}}$, μ^*_{app} is the *apparent viscosity.* In this manner, $\mathbb{T}^*$ is decomposed into its *spherica part* $(-p^*\mathbb{I})$ and the so-called *deviatoric part* denoted by $\mathbb{S}^* := 2\mu^*_{app}\,(\dot{\gamma}^*)\,\mathbb{D}^*$. Depending on the characterization of the latter, we have different types of fluid behaviour. The qualitative *shear rate-shear stress* and *shear rate-apparent viscosity* diagrams are shown below to characterize the so-called *pseudo-plastic fluid* and *dilatant fluid*, depending on whether μ^*_{app} is monotonically decreasing or increasing.

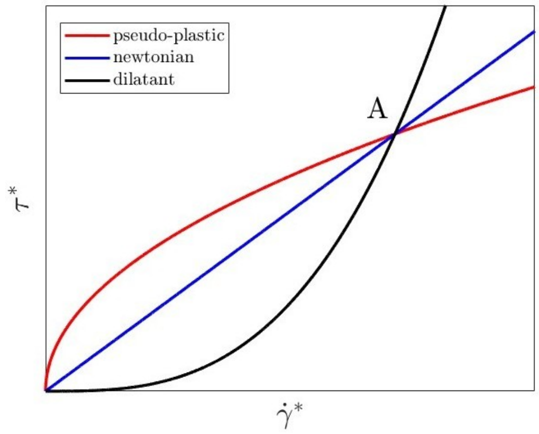

Figure 1: Shear rate-shear stress diagram.

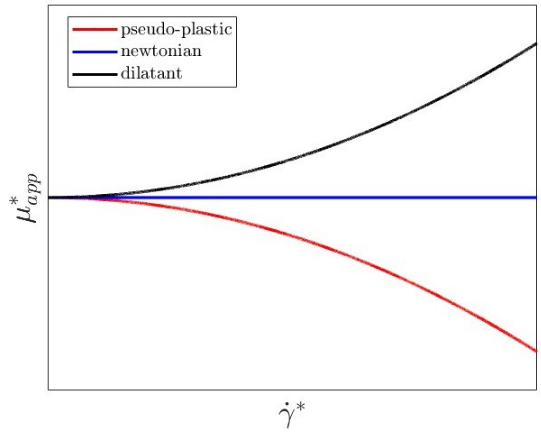

Figure 2: Shear rate-apparent viscosity diagram.

From Fig. (1), we observe that, compared to a purely Newtonian fluid, at the same shear rate, *dilatant* fluids are characterised by a higher level of shear rate when they pass point A. Similarly, Fig. (2) shows an opposite monotonic trend of μ^*_{app} for the two cases. Below, some types of *viscoplastic fluids* will be illustrated, which unlike the fluids just seen above, have a *yield stress* level τ^*_0 below which they do not deform, and only when this level is exceeded they show a possible *dilatant* or *pseudo-plastic* behaviour (see Fig. (3)). The first studies based on *yield stress* date back to at least the early 1900s [Sch00], and have intensified in the years that followed, leading to increasingly complex mathematical models. Obviously, and without claiming to be exhaustive, in the following subsections some of the most important mathematical models of GNF fluids will be examined. Some of those considered here can be derived as special cases of the *Herschel-Bulkley model* [Her26], [Sar16], which is characterized by the following constitutive relationship:

$$\begin{cases} \mathbb{S}^* = \left(2k^* \left(\dot{\gamma}^*\right)^{n-1} + \dfrac{\tau_y^*}{\dot{\gamma}^*}\right) \mathbb{D}^*, & \text{if} \quad \tau^* > \tau_y^*; \\ \mathbb{D}^* = \mathbb{O}^*, & \text{if} \quad \tau^* \leq \tau_y^*, \end{cases} \tag{5}$$

where n is called the fluid behavior index (or *power-law* index), k^* is the so-called consistency index, and τ_y^* is the yield stress.

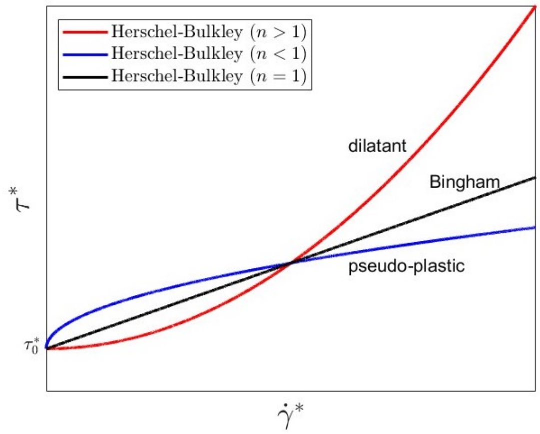

Figure 3: Shear rate-shear stress diagram.

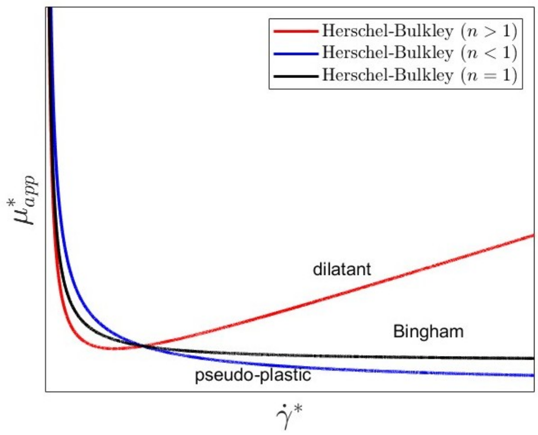

Figure 4: Shear rate-apparent viscosity diagram.

1.3.1 Power-law fluids

When $\tau_0^* = 0$ in (5), we have $\mu_{app}^* = k^*(\dot{\gamma}^*)^{n-1}$, and (4) becomes:

$$\mathbb{T}^* = -p^*\mathbb{I} + 2k^*(\dot{\gamma}^*)^{n-1}\mathbb{D}^*. \tag{6}$$

Two cases are distinguished:

- $0 < n < 1$ pseudo-plastic (or *shear thinning*)

$$\lim_{\dot{\gamma}^* \to 0} \mu_{app}^*(\dot{\gamma}^*) = \infty \quad \text{and} \quad \lim_{\dot{\gamma}^* \to \infty} \mu_{app}^*(\dot{\gamma}^*) = 0;$$

- $n > 1$ dilatant (or *shear thickening*)

$$\lim_{\dot{\gamma}^* \to 0} \mu^*_{app}(\dot{\gamma}^*) = 0 \quad \text{and} \quad \lim_{\dot{\gamma}^* \to \infty} \mu^*_{app}(\dot{\gamma}^*) = \infty.$$

This model effectively interprets the types of nonlinearity of (4) shown in Fig. (3) and Fig. (4) (where there is a qualitative comparison with Newtonian fluids). For greater clarity, Figures (5) and (6) depict the two cases for $n \lessgtr 1$.

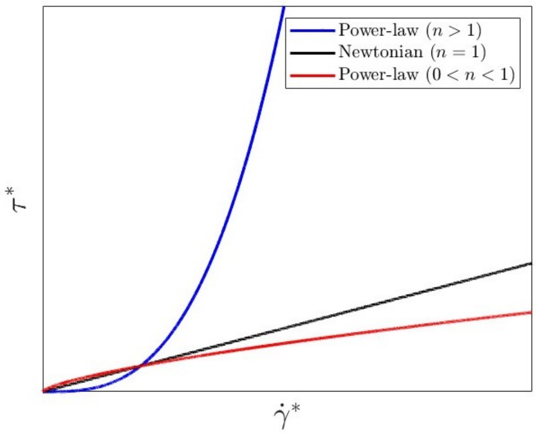

Figure 5: Shear rate-shear stress diagram.

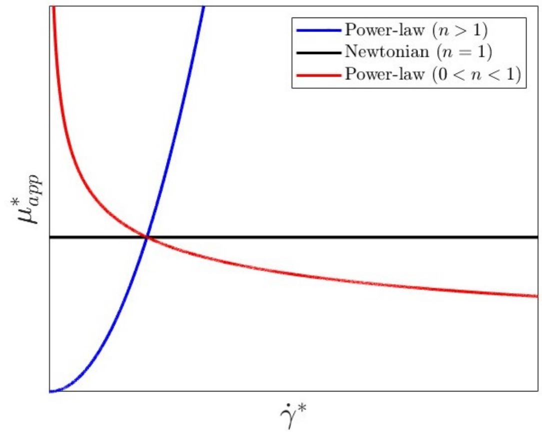

Figure 6: Shear rate-apparent viscosity diagram.

In the next model, a nonlinearity of a different nature will be shown, namely of the *visco-plastic* type, with a level of *yield stress* to be overcome to exhibit "fluid-like" behaviour.

1.3.2 Bingham fluids

This model can also be seen as a special case of the *Herschel-Bulkley model* [Her26], [HB26], [Bin22]. In fact, it suffices to consider $n = 1$ and $\tau^*_y > 0$ in Eq. (5). The resulting constitutive relationship, seemingly simple, turns out to be particularly challenging both analytically and numerically. In this case, $\mathbb{T}^* = -p^*\mathbb{I} + \mathbb{S}^*$ is defined as follows:

$$\begin{cases} \mathbb{S}^* = \left(2\mu^*_B + \dfrac{\tau^*_y}{\dot{\gamma}^*}\right)\mathbb{D}^*; & \text{if } \tau^* > \tau^*_y; \\ \mathbb{D}^* = \mathbb{O}^*; & \text{if } \tau^* \leq \tau^*_y, \end{cases} \tag{7}$$

where μ^*_B is the Bingham viscosity and τ^*_y is the yield stress.

Figures (7) and (8), to which the Bingham regularised fluids diagram (dis-

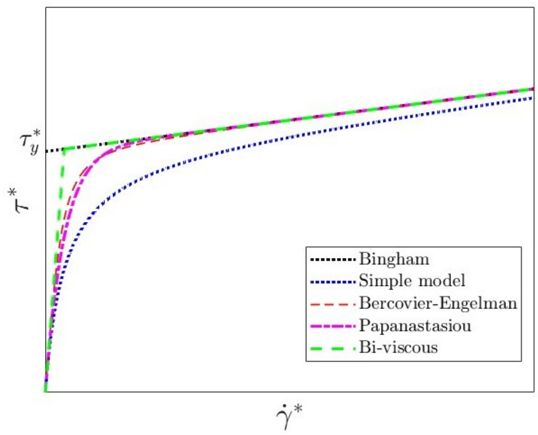

Figure 7: Shear rate-shear stress diagram.

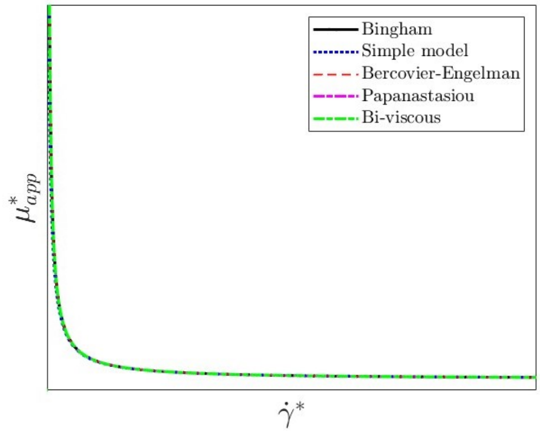

Figure 8: Shear rate-apparent viscosity diagram.

cussed later) has also been overlaid, illustrate the qualitative behaviour of the Shear rate-shear stress diagram and the Shear rate-apparent viscosity diagram.

1.3.3 Regularised models

As mentioned earlier, the shear rate-shear stress relationship for the Bingham model (or more generally for the Herschel-Bulkley model) is not a function but a graph (due to the initial singularity). To avoid the inherent singularity at zero shear rate, several regularized models have been proposed, such as the *simple model* [AFS00],[FN05], the *Bercovier-Engelman model.* [BE80], as well as the *Papanastasiou model* [Pap87], the *bi-viscous model* [TM83], just to name a few. Most of these propose a smooth shear rate-apparent viscosity law, thus avoiding problems at singular points (as will be seen later in the differential equations, where differential operators act on the apparent viscosity).

Below are the various formulations of μ^*_{app} for the mentioned models:

$$\mu^*_{\mathrm{app}} = 2\mu^*_{\mathrm{B}} + \frac{\tau^*_y}{(\dot{\gamma}^* + \epsilon^*)}, \qquad \textit{(Simple model)}; \tag{8}$$

$$\mu^*_{\mathrm{app}} = 2\mu^*_{\mathrm{B}} + \frac{\tau^*_y}{\sqrt{(\dot{\gamma}^{*2} + \epsilon^{*2})}}, \qquad \textit{(Bercovier-Engelman model)}; \tag{9}$$

$$\mu^*_{\mathrm{app}} = 2\mu^*_{\mathrm{B}} + \tau^*_y \frac{1 - e^{-\dot{\gamma}^*/\epsilon^*}}{\dot{\gamma}^*}, \qquad \textit{(Papanastasiou model)}; \tag{10}$$

$$\begin{cases} \mu^*_{\text{app}} &= \dfrac{1}{\epsilon^*}, \qquad \text{if } \ \tau^* \le \tau^*_1, \qquad \left(\mu^*_1 > \mu^*_{\text{Bg}}, \ \ \tau^*_y < \tau^*_1 = \dfrac{\tau^*_y}{1-2\epsilon^*\mu_{\text{B}}{}^*}\right), \\ \mu^*_{\text{app}} &= 2\mu^*_{\text{B}}, \quad \text{if } \ \tau^* > \tau^*_1, \qquad \textit{(bi-viscous model)}, \end{cases} \tag{11}$$

where $0 < \epsilon^* \ll 1$ is a parameter such that the smaller it is, the better it approximates the Bingham model. Often, the term *Bingham regularised model* will be used to refer to the *Simple model.* Qualitatively, the above models are depicted in Figures (7) and (8). It can be observed in Fig. (7) that the qualitative behaviour of all models is almost identical (for small ϵ^*): by decreasing ϵ^* appropriately, all curves uniformly tend towards the Bingham model. In Fig. (8), it should be noted that all regularizing models are defined for $\dot{\gamma}^* = 0$ (unlike the Bingham model, which is not defined for $\gamma^* = 0$), so that the apparent viscosity is infinite for $\dot{\gamma}^* \longrightarrow 0^+$ only in the Bingham model and then for $\dot{\gamma}^* \to +\infty$, all models tend to $2\mu^*_{\text{B}}$. One of the main properties of these regularized models lies in the possibility of numerically treating very efficiently the systems of nonlinear differential equations governing the motion (see chapter 2, Sections 2.3, 2.4, 2.5 and 2.6). Of course, in all of the regularized models a "*pure rigid domain*" does not exist.

1.3.4 Casson model and Casson regularised model

The *Casson model* is a viscoplastic fluid characterized by an apparent viscosity given by:

$$\mu^*_{\text{app}}(\dot{\gamma}^*) = \left(\sqrt{2\mu^*_{\text{B}}} + \frac{\sqrt{\tau^*_y}}{\sqrt{\dot{\gamma}^*}}\right)^2. \tag{12}$$

A possible *regularized* version [Cas59] is:

$$\mu^*_{\text{app}}(\dot{\gamma}^*) = \left(\sqrt{2\mu^*_{\text{B}}} + \frac{\sqrt{\tau^*_y}}{\left(\sqrt{\dot{\gamma}^*} + \sqrt{\epsilon^*}\right)}\right)^2, \tag{13}$$

where $0 < \epsilon^* \ll 1$ is a parameter that, the smaller it is, the closer the regularized model approaches the original (see Figs. (9) and (10)). Consequently, (4) becomes:

$$\mathbb{T}^* = -p^*\mathbb{I} + \left(\sqrt{2\mu_{\mathrm{B}}^*} + \frac{\sqrt{\tau_y^*}}{\left(\sqrt{\dot{\gamma}^*} + \sqrt{\epsilon^*}\right)} \right)^2 \mathbb{D}^*. \tag{14}$$

Regarding Figures (9), it is observed that, unlike Bingham models (regularized or pure), in this case, there is no oblique asymptote in the Shear rate-shear stress diagram, which characterizes the growth of the shear stress. Furthermore, from Figure (10), we observe a *qualitative* trend always along a hyperbolic branch for the *pure Casson model* and the *regularized Casson model*, always equal to $\mu^*_{app} = 2\mu^*_B$ when $\dot{\gamma}^* = +\infty$.

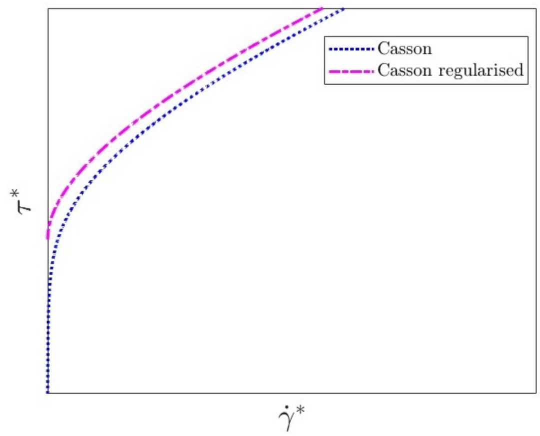

Figure 9: Shear rate-shear stress diagram.

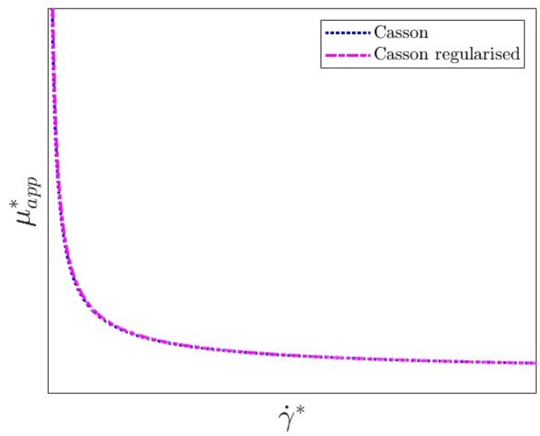

Figure 10: Shear rate-apparent viscosity diagram.

1.4 Time-dependent fluid behavior

For some types of fluids, the apparent viscosity may depend not only on the rate of shear but also on the time the fluid has been subjected to shear. It happens, for example, that the apparent viscosity gradually decreases due to the progressive breakdown of the internal structure. Therefore, the rate of change of apparent viscosity decreases, but simultaneously, the rate of formation of the bonds increases. At some point, a state of dynamic equilibrium is reached when the rates of build-up and breakdown are balanced (e.g., in a red mud suspension, several different gels, and colloids). However, other types of materials may exhibit the opposite behavior regarding apparent viscosity, i.e., an increase in the latter is observed (e.g., chalk paste). Depending on the increasing or decreasing behavior of apparent viscosity, two particular categories are distinguished: *thixotropic fluids* and *rheopectic or negative thixotropic fluids.* In this context, materials of this type will not be considered further; however, for a more comprehensive examination, references [CR11], [Sch94], [Bar97], [SK65], [KKJ90], [PR77], [Mew79], [MBM02], [Hou81], [CC89], [DM05], [DM06], [GA72] are recommended.

1.5 Viscoelastic fluid behavior

Viscoelastic fluids exhibit an intermediate behavior between viscous fluids and elastic materials depending on the duration of the applied stress they are subjected to. When an elastic solid deformed, it regains its original shape after the stress is removed. However, if the applied stress exceeds the characteristic yield stress of the material, complete recovery will not occur, and "creep" will occur, meaning the initial "solid" behaves like a fluid (e.g., polymer melts, polymer and soap solutions, synovial fluid, etc.). This type of fluid will also not be further investigated, and for further insights, references [BW12], [Sch78], [BB87], [CDKC21], [TW98], [Lar99], [Mor01] are recommended.

1.6 Pressure-dependent viscosity

The initial studies on this type of fluids can be traced back to [Bri31], and it is known that while high pressure decreases the volume of liquids, the effect of increasing pressure produces significant changes in the properties of liquids, such as viscosity, thermal conductivity, etc., while maintaining, for a wide class of fluids, the density nearly unchanged. This allows treating these materials as incompressible [SR10]. One of the earliest analyses on this type of fluids is found in [Bar93], which established the following relationship between pressure and viscosity:

$$\mu^*(p^*) = \mu_0^* e^{\beta^* p^*}, \tag{15}$$

where μ^* represents viscosity, p^* denotes pressure, while μ_0^* and β^* are positive constants. It can be noticed that the increase in pressure affects viscosity exponentially, leading to a considerable increase in viscosity by several orders of magnitude. Subsequently, more general pressure-viscosity relationships have been proposed, including temperature θ^* and density ρ^*. For instance, as early as 1930, [And30] proposed:

$$\mu^*(p^*, \rho^*, \theta^*) = A^* \sqrt{\rho^*} e^{\left(p^* + \rho^{*2} r^*\right) \dfrac{s^*}{\theta^*}}, \tag{16}$$

where A^*, r^*, and s^* are constants. From 1958 to 2008, articles of particular interest regarding this type of fluids undoubtedly include the following: [CMWS58], [GWS58], [JT77], [JG80], [BFS01], [PDR99], [BK03], [CB08], [HB07].
In chapter (3), this type of fluid will be analyzed in a channel with non-straight walls and then in a tube with a variable cross-section (where it will be possible to reduce to the two-dimensional case using the momentum balance equation formulated in cylindrical coordinates). Since these problems will be addressed under isothermal conditions, formulation (15) will be used regarding the pressure-viscosity law.

1.7 Description of the assumptions of the present thesis

In this thesis, the *temperature* will be neglected, as the models to be analyzed subsequently are all in an isothermal setting. However, it is important to emphasize that, often, for some materials, temperature variation can significantly influence rheological parameters. Therefore, in these cases, it is essential to consider the crucial role of temperature.

2 A spectral collocation scheme for the two dimensional flow of a regularized viscoplastic fluid: numerical results and comparison with analytical solution

The material of this section constitutes an extended version of the corresponding article [FG24b]. As already mentioned, viscoplastic fluids are characterized by a yield stress that must be overcome for the flow to start , see [Hui15]. The constitutive equation of a viscoplastic material allows one to divide the domain in yielded and unyielded regions. In the unyielded region the modulus of the deviatoric stress is below the critical threshold so that no deformation is possible and the fluid behaves as a rigid body. The surface that divides the yielded and the unyielded domain, called the yield surface, is a priori unknown and must be determined by imposing appropriate boundary conditions (free boundary problem). The simplest viscoplastic fluid is the so-called Bingham fluid [Bin22], which is characterized by a linear stress/strain-rate relation above the critical threshold. More complex models with nonlinear stress/strain-rate relation can also be considered (Herschel-Bulkley, Casson, etc., see [HB26],[Cas59]).

In a viscoplastic fluid, when the rate of deformation is zero the rheological model presents a singularity due to the apparent viscosity that becomes infinite (rigid body behaviour). This singularity produces significant numerical and analytical problems in the solution of the mathematical problem, in particular in the detection of the yield surface. The inspiration for this work comes from the necessity of finding appropriate approximations (regularized models) capable of smoothing such singularity. In this optics, one can consider regularized models, such as the Papanastasiou or the Bercovier-Engelman models, see [Pap87],[BE80]. The idea of regularization is natural, from both physical and mathematical perspectives. In the regularized models the singularity is smoothed through a sufficiently regular viscosity function that approximates the exact model. Of course, one has an infinity of suitable choices for the approximating function. There is an ongoing debate on whether the regularized models are of some help or not, since it is well known that some of the properties of the exact viscoplastic fluid are not recovered when the approximated model tends to the exact one, see for instance [FN05], [FFRV22]. Other strategies aimed at overcoming the singularity issues of the exact model are also possible. Among these, we mention the one in which the unyielded region is treated as an elastic or viscoelastic solid, [FF04], [FFR16].

The Stokes flow of viscoplastic fluids in a two-dimensional channel of varying width has been widely studied in the past decades, see [Hui15] and the references therein. Analytical solutions can be obtained for particular geometrical settings (e.g. lubrication flows) for both "true" viscoplastic and regularized flows, [FR04], [FFRR15], [PDGH18], [FFRV22], [YHM08], [PFM09]. Many numerical methods have been employed to investigate the flow behaviour of exact and regularized viscoplastic fluids in more general geometrical settings, [GW11], [Hui15], [HG20].

In this part of the thesis, a spectral collocation scheme is presented to investigate the two-dimensional Stokes flow of a "regularized viscoplastic fluid" in a symmetric channel of non-uniform width driven by an applied pressure gradient (plane Poiseuille flow). This approach, which is much simpler than other methods such as finite element methods or finite volume methods, and also requires less CPU time, has not been employed so far for this type of problem. The analysis is limited to a regularized Bingham fluid and a regularized Casson fluid, but the scheme can also be applied to any generalized Newtonian fluid, i.e., any fluid in which the apparent viscosity depends on the modulus of the strain rate tensor (Power-law, Cross, Carreau, etc.). To the authors' knowledge spectral methods have never been employed for the channel flow of viscoplastic fluids. The main numerical approaches, i.e. regularization and augmented Lagrangian methods are typically implemented in finite elements/volume discretization, [SW17].

From the point of view of possible applications, this work can be useful in all the situations in which one has to solve flow problems that can be approximated by a non uniform 2D geometry, e.g. flow of muds, slurries, waxy oils or any industrial viscoplastic fluids in closed channels. The importance of this study is not tied therefore to any particular application.

The mathematical problem consists of mass and momentum balance to which we add no-slip wall conditions plus inlet/outlet pressure conditions. In a 2D non-uniform channel this problem is well posed, see [BCM91]. The problem is reformulated in a dimensionless form and the flow domain is mapped in the square $[-1, 1]^2$ so that the discretized spectral differentiation operators can be applied. The problem is written in the first-order velocity-stress-pressure formulation in which the stress components are treated as unknowns. The discretized problem consists of a nonlinear system plus boundary conditions. The adding of the boundary conditions to the discretized problem leads to a nonlinear overdetermined system that is solved via least-squares and exploiting Newton's method, see [Hei04], [Hei06]. The advantage of using least-squares is that this method results in a symmetric and positive definite algebraic system which circumvents the well-known LBB (Ladyzhenskaya-Babuška-Brezzi) condition, see [BBF+13]. To validate the numerical model, a comparison is made between the numerical solution and the analytical solution, which can be explicitly obtained if the aspect ratio of the channel is sufficiently small (lubrication approximation). Indeed, in the case of small aspect ratio, the solution can be sought in the form of an asymptotic expansion around the small ratio parameter, in which each term of the expansion can be determined by an iterative process.

In particular, the "leading order" solution will be compared with the general numerical solution obtained through the least-square spectral collocation method. It will be shown that the agreement between the two is excellent. Additionally, some properties of symmetry of the analytical solution (small aspect ratio solution) will be proven, which also hold for the general numerical solution (any aspect ratio).

The main novelty is the adoption of a numerical scheme based on spectral collocation methods, which are more flexible and of easy implementation than other methods (e.g. finite differences, finite elements and finite volumes). The focus has been on regularized viscoplastic fluids because the approximated models allow one to overcome the singularity issues inherently present in this type of fluid.

It should also be noticed that this method is highly versatile, since a simple change of the viscosity function allows one to deal not only with any type of generalized Newtonian fluid, but also with fluids of implicit type, such as fluids with pressure-dependent viscosity [HMR01]. The principal research question this paper sets out to answer is the detection of the yield surface and the dependence of the latter on 1) the rheological parameters; 2) on the geometry of the system; 3) on the applied pressure drop.

2.1 The mathematical model

Let us consider an incompressible generalized Newtonian fluid where the apparent viscosity depends on the strain-rate modulus[3], i.e. $\mu^* := \mu^*(\dot{\gamma}^*)$, where

$$\dot{\gamma}^* := \sqrt{\frac{1}{2}\mathrm{tr}\left(\mathbb{D}^{*2}\right)}, \tag{17}$$

is the Frobenius norm of the symmetric part of the velocity gradient tensor $\mathbb{D}^*$. The Cauchy stress tensor is written as

$$\mathbb{T}^* = -p^*\mathbb{I} + 2\mu^*(\dot{\gamma}^*)\mathbb{D}^*, \tag{18}$$

where $\mathbb{S}^* =: 2\mu^*(\dot{\gamma}^*)\mathbb{D}^*$ is the deviatoric part of the stress and $-p^*\mathbb{I}$ is the spherical part, p^* being the Lagrange multiplier due to the incompressibility constraint (pressure). Mass and momentum balance, in the absence of body forces, yield (see [TNTN04])

$$\begin{cases} \rho^* \dfrac{D\mathbf{v}^*}{Dt^*} = -\nabla^* p^* + \nabla^* \cdot \mathbb{S}^*, \\ \\ \nabla^* \cdot \mathbf{v}^* = 0, \end{cases} \tag{19}$$

ρ^* being the constant density of the fluid and $\mathbf{v}^*$ the velocity field. We consider a 2D flow in a channel of length L^* bounded by the rigid walls $y^* = \pm h^*(x^*)$, $h^*(x^*)$ being a sufficiently regular positive function defined in $[-L^*, L^*]$, see Fig. 11. The function $h^*(x^*)$ that defines the channel profile can be of any type, provided it is sufficiently regular (C^1). Because of this general geometrical setting, our study can be applied to all applications in which the flow can be considered two-dimensional and symmetric.

The flow is driven by the pressure drop $\Delta p^* = p^*_{in} - p^*_{out}$, where p^*_{in} and p^*_{out}

[3] In the thesis the starred quantities denote dimensional variables.

are the pressure at the inlet and outlet respectively. The velocity $\mathbf{v}^*$ is given by

$$\mathbf{v}^*(x^*, y^*, t^*) = u^*(x^*, y^*, t^*)\mathbf{e}_1 + v^*(x^*, y^*, t^*)\mathbf{e}_2. \tag{20}$$

The boundary conditions for the velocity field are no-slip at the channel walls and null transversal velocity at the inlet and outlet. The boundary conditions for the pressure are given imposing the inlet and outlet pressure. With these boundary conditions, problem (19) is well posed, see [BCM91]. We shall limit our study to the following types of apparent viscosities (already considered above in (8), (13) and here rewritten simply by placing $\mu_o^* := 2\mu_B^*$)

$$\mu^*(\dot\gamma^*) = \left(\mu_o^* + \frac{\tau_y^*}{\dot\gamma^* + \varepsilon^*}\right), \qquad \text{(Regularized Bingham)} \tag{21}$$

$$\mu^*(\dot\gamma^*) = \left(\sqrt{\mu_o^*} + \frac{\sqrt{\tau_y^*}}{\sqrt{\dot\gamma^*} + \sqrt{\varepsilon^*}}\right)^2, \qquad \text{(Regularized Casson)} \tag{22}$$

where μ_o^* is a characteristic viscosity, τ_y^* is the yield stress and ε^* is a regularization parameter with the dimension of a strain rate. The constitutive laws (21), (22) are those of a regularized Bingham fluid and of a regularized Casson fluid. From (21), (22) we notice that for $\varepsilon^* \to 0$ we recover the exact Bingham and Casson models, while for $\varepsilon^* \to \infty$ we recover the classical Navier-Stokes incompressible model.

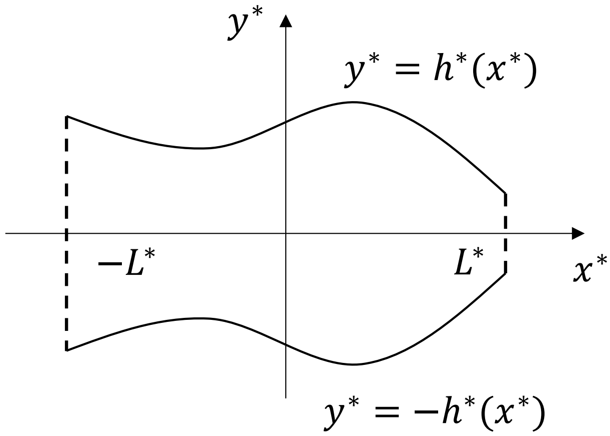

Figure 11: Sketch of the domain of the problem. A symmetric two-dimensional channel with non-flat walls. The channel profile is assumed to be C^1.

2.2 Non-dimensional formulation

We define

$$H^* = \sup_{x^* \in [-L^*,\ L^*]} h^*(x^*), \qquad \delta = \frac{H^*}{L^*}, \tag{23}$$

and rescale the variables as follows

$$\begin{cases} x = \dfrac{x^*}{L^*},\ y = \dfrac{y^*}{H^*},\ t = \left(\dfrac{U^*}{L^*}\right) t^*,\ u = \dfrac{u^*}{U^*},\ v = \dfrac{v^*}{\delta U^*};\ p = \dfrac{p^* - p^*_{out}}{P^*}, \\ \\ \mathbb{D} = \left(\dfrac{H^*}{U^*}\right) \mathbb{D}^*,\quad \mathbb{S} = \left(\dfrac{H^*}{\mu^*_o U^*}\right) \mathbb{S}^*,\ \dot{\gamma} = \left(\dfrac{H^*}{U^*}\right) \dot{\gamma}^*,\ \mu = \dfrac{\mu^*(\dot{\gamma})}{\mu^*_o}, \end{cases} \tag{24}$$

where U^* and P^* are the characteristic velocity and pressure respectively. The following expressions are obtained:

$$\mathbb{D} = \frac{1}{2} \begin{bmatrix} 2\delta u_x & u_y + \delta^2 v_x \\ \\ u_y + \delta^2 v_x & 2\delta v_y \end{bmatrix}, \quad \mathbb{S} = 2\mu(\dot{\gamma})\,\mathbb{D} = \begin{bmatrix} S_{11} & S_{12} \\ \\ S_{21} & S_{22} \end{bmatrix},$$

$$\dot{\gamma} = \sqrt{\delta^2 (u_x)^2 + \frac{1}{4} (u_y + \delta^2 v_x)^2}. \tag{25}$$

The non dimensional versions of (21), (22) are

$$\mu(\dot{\gamma}) = \left(1 + \frac{B}{\dot{\gamma} + \varepsilon}\right), \qquad \text{(Regularized Bingham)} \tag{26}$$

$$\mu(\dot{\gamma}) = \left(1 + \frac{\sqrt{B}}{\sqrt{\dot{\gamma}} + \sqrt{\varepsilon}}\right)^2, \qquad \text{(Regularized Casson)} \tag{27}$$

where

$$B = \left(\frac{\tau^*_y H^*}{\mu_o U^*}\right), \qquad \varepsilon = \left(\frac{H^*}{U^*}\right) \varepsilon^*, \tag{28}$$

B being the Bingham number. Selecting $P^* = \frac{\mu_o^* U^* L^*}{{H^*}^2}$, the momentum balance can be written component-wise as shown below:

$$\begin{cases} Re\delta\left(u_t + u_x u + u_y v\right) = -p_x + \delta(S_{11})_x + (S_{12})_y, \\ \\ Re\delta^3\left(v_t + v_x u + v_y v\right) = -p_y + \delta^2(S_{12})_x + \delta(S_{22})_y, \end{cases} \tag{29}$$

where $Re := (\rho^* U^* H^*)/\mu_o^*$ is the Reynolds number. Finally, assuming $Re \ll 1$ (creeping flow) and rescaling $h^*(x^*)$ with H^* we write the complete system in the stress-based formulation

$$\begin{cases} -p_x + \delta(S_{11})_x + (S_{12})_y = 0, \\ \\ -p_y + \delta^2(S_{12})_x + \delta(S_{22})_y = 0, \\ \\ S_{11} = 2\delta\mu\left(\dot{\gamma}\right) u_x, \\ \\ S_{12} = \mu\left(\dot{\gamma}\right)\left(u_y + \delta^2 v_x\right), \\ \\ S_{22} = 2\delta\mu\left(\dot{\gamma}\right) v_y, \\ \\ u_x + v_y = 0, \\ \\ u|_{y=\pm h(x)} = v|_{y=\pm h(x)} = 0, \qquad p|_{x=-1} = p_{in}, \qquad p|_{x=1} = 0, \qquad v|_{x=\pm 1} = 0, \end{cases} \tag{30}$$

where

$$p_{in} = \frac{p_{in}^* - p_{out}^*}{\left(\dfrac{\mu_o U^*}{\delta H^*}\right)} > 0. \tag{31}$$

The system (30) is well posed (see [BCM91]) in the unknowns $S_{11},\ S_{12},\ S_{22},\ u,\ v,\ p$ and will be solved numerically in the next section.

Remark 1. *In the Bingham (or Casson) model the unyielded regions are those for which $|\mathbb{S}| \leqslant B$ or equivalently those for which $\mathbb{D} \equiv 0$. In the regularized models the unyielded regions are approximated by those for which $|\mathbb{S}| \leqslant B$ even if*

$\mathbb{D} \neq 0$ in such regions. Indeed, the regularized models are "seemingly" viscoplastic (they do not have a real yield stress) and not "truly viscoplastic".

Let us now focus on the third condition of $(30)_8$*. We observe that* $v(\pm 1, y) = 0$*, so that*

$$v_y(\pm 1, y) \underbrace{=}_{\textit{mass balance}} -u_x(\pm 1, y) = 0. \tag{32}$$

Moreover, because of symmetry with respect to the central plane $y = 0$, we also have

$$u_y(x, 0) = v(x, 0) = v_x(x, 0) = 0. \tag{33}$$

Hence, recalling the definition (25) *we get*

$$\dot{\gamma}(\pm 1, 0) = 0, \tag{34}$$

so that $(\pm 1, 0)$ *are points with zero shear rate. This means that there exist neighborhoods of* $(\pm 1, 0)$ *in which the fluid is unyielded in the sense explained above* $(|\mathbb{S}| \leqslant B)$*. When $B = 0$ these regions reduce to the points* $(\pm 1, 0)$*.*

2.3 Numerical scheme

The basic domain for the application of the Spectral Collocation Method is the square centered at the origin of the Cartesian system with side length two, i.e. $[-1, 1]^2$. To map the flow domain into the computational domain $[-1, 1]^2$, the following coordinate transformation is considered:

$$\xi = x, \qquad \eta = \frac{y}{h(x)} \in [-1,\ 1]. \tag{35}$$

The system (30) can be written for the new coordinates (ξ, η), introducing the new variables:

$$u(x, y) = \widehat{u}(\xi, \eta), \quad v(x, y) = \widehat{v}(\xi, \eta), \quad p(x, y) = \widehat{p}(\xi, \eta), \tag{36}$$

$$S_{11}(x, y) = \widehat{S}_{11}(\xi, \eta), \quad S_{12}(x, y) = \widehat{S}_{12}(\xi, \eta), \quad S_{22}(x, y) = \widehat{S}_{22}(\xi, \eta). \tag{37}$$

The following differential operators are also introduced

$$P_1 := \partial_\xi + \left(\frac{\eta}{h(\xi)} h_\xi(\xi) \right) \partial_\eta, \qquad P_2 := \frac{1}{h(\xi)} \partial_\eta, \tag{38}$$

both defined on the functional space

$$\mathcal{L}_d = \left\{ f \ : \ [-1,\ 1]^2 \to \ \mathbb{R} \ : \ f \in C^1 \left([-1,\ 1]^2 \right) \right\}. \tag{39}$$

Consequently, for a generic function $g(x,y) = \widehat{g}(\xi,\eta)$ defined in the domain (x,y), the transformation of its derivatives with respect to x and y in the computational domain (ξ,η) becomes simply

$$g_x = P_1 \widehat{g}, \qquad \text{and} \qquad g_y = P_2 \widehat{g}. \tag{40}$$

Thus, the entire problem can be reformulated in terms of the new coordinate system (ξ,η) using operators P_1 and P_2. The strain rate tensor, its magnitude, and the stress tensor are computed as follows:

$$\widehat{\mathbb{D}}(\xi,\eta) = \frac{1}{2} \begin{bmatrix} 2\delta P_1 \widehat{u} & P_2 \widehat{u} + \delta^2 P_1 \widehat{v} \\ & \\ P_2 \widehat{u} + \delta^2 P_1 \widehat{v} & 2\delta P_2 \widehat{v} \end{bmatrix}, \tag{41}$$

$$\widehat{\dot\gamma}(\xi,\eta) = \sqrt{\delta^2 \left(P_1 \widehat{u}\right)^2 + \frac{1}{4} \left(P_2 \widehat{u} + \delta^2 P_1 \widehat{v}\right)^2}, \tag{42}$$

$$\widehat{\mathbb{S}}(\xi,\eta) = \widehat{\mu}(\widehat{\dot\gamma}) \begin{bmatrix} 2\delta P_1 \widehat{u} & P_2 \widehat{u} + \delta^2 P_1 \widehat{v} \\ & \\ P_2 \widehat{u} + \delta^2 P_1 \widehat{v} & 2\delta P_2 \widehat{v} \end{bmatrix}. \tag{43}$$

The system (30) can be rewritten in the following form:

$$\begin{bmatrix} \delta P_1 & P_2 & 0 & 0 & 0 & -P_1 \\ 0 & \delta^2 P_1 & \delta P_2 & 0 & 0 & -P_2 \\ 1 & 0 & 0 & -2\widehat{\mu}\delta P_1 & 0 & 0 \\ 0 & 1 & 0 & -\widehat{\mu} P_2 & -\widehat{\mu}\delta^2 P_1 & 0 \\ 0 & 0 & 1 & 0 & -2\widehat{\mu}\delta P_2 & 0 \\ 0 & 0 & 0 & P_1 & P_2 & 0 \end{bmatrix} \begin{bmatrix} \widehat{S}_{11} \\ \widehat{S}_{12} \\ \widehat{S}_{22} \\ \widehat{u} \\ \widehat{v} \\ \widehat{p} \end{bmatrix} = 0, \tag{44}$$

to which we add the boundary conditions

$$\begin{cases} \widehat{u}|_{\eta=\pm 1} = \widehat{v}|_{\eta=\pm 1} = 0, \\ \widehat{p}|_{\xi=-1} = p_{in}, \\ \widehat{p}|_{\xi=1} = 0, \\ \widehat{v}|_{\xi=\pm 1} = 0. \end{cases} \tag{45}$$

In order to discretise the non-linear system (44), the following Chebyshev Gauss-Lobatto collocation nodes are introduced (GL nodes):

$$(\xi_i, \eta_j) = \left(\cos\frac{(i-1)\pi}{N}, \cos\frac{(i-1)\pi}{N}\right), \qquad i, j = 1, \ldots\ldots\ldots\ldots, N+1. \tag{46}$$

GL points are considered in a "lexicographic" order as in [Tre00], see Fig. 12. This means that the $(N+1)\times(N+1)$ array of nodes is transformed in a $(N+1)^2$ vector ordered following the red pattern indicated in Fig. 12. Denoting by b_{in} the indices[4] of the inlet nodes except corners, by b_{out} the indices of the outlet nodes except corners, by b_{up} the indices of the upper edge nodes and by b_{down} the indices of the lower edge nodes. The spectral partial derivatives in the (ξ, η) coordinate are given by

$$\partial_\xi \approx D_\xi = D \otimes_K I, \qquad \partial_\eta \approx D_\eta = I \otimes_K D, \tag{47}$$

where D is the $(N+1)\times(N+1)$ differentiation matrix defined in [Tre00] and $\otimes_K$ is the Kronecker product. Notice that the dimensions of the differentiation matrices differentiation matrices D_ξ, D_η are $(N+1)^2 \times (N+1)^2$. These matrices operate on functions defined on grid nodes put in the lexicographic order, i.e., they operate on vectors. Approximating the differential operators (38) using (47)

[4] Here the indices are considered with respect to the lexicographic order.

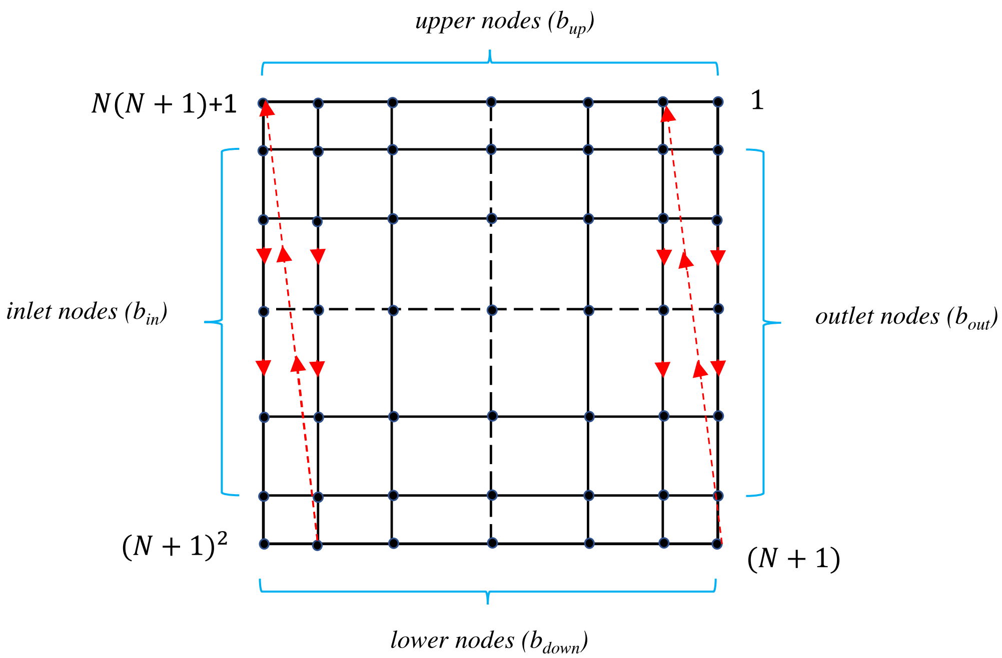

Figure 12: Computational grid.The black circles represent the nodes of the grid.

and substituting into (44) we get the following nonlinear square system

$$\begin{bmatrix} \delta P_{1,N} & P_{2,N} & 0 & 0 & 0 & -P_{1,N} \\ 0 & \delta^2 P_{1,N} & \delta P_{2,N} & 0 & 0 & -P_{2,N} \\ I & 0 & 0 & -2\widehat{\mu}_N \delta P_{1,N} & 0 & 0 \\ 0 & I & 0 & -\widehat{\mu}_N P_{2,N} & -\widehat{\mu}_N \delta^2 P_{1,N} & 0 \\ 0 & 0 & I & 0 & -2\widehat{\mu}_N \delta P_{2,N} & 0 \\ 0 & 0 & 0 & P_{1,N} & P_{2,N} & 0 \end{bmatrix} \begin{bmatrix} \widehat{S}_{11,N} \\ \widehat{S}_{12,N} \\ \widehat{S}_{22,N} \\ \widehat{u}_N \\ \widehat{v}_N \\ \widehat{p}_N \end{bmatrix} = 0, \tag{48}$$

where the pedix N indicates we are considering the discretized form of the operators and variables. Notice that each of the unknowns $\widehat{S}_{11,N}$, $\widehat{S}_{12,N}$, $\widehat{S}_{22,N}$, $\widehat{u}_N$, $\widehat{v}_N$, $\widehat{p}_N$ are in the form of a vector of $(N+1)^2$ elements, coherently with the lexicographic order of Fig. 12.

The boundary conditions must be added to the system (48) (which has dimensions $6(N+1)^2 \times 6(N+1)^2$). To this end, following [Hei04], the BC operator

B_N is defined in the following manner.

$$\underbrace{\begin{bmatrix} 0 & 0 & 0 & B_{ud,N} & 0 & 0 \\ 0 & 0 & 0 & 0 & B_{ud,N} & 0 \\ 0 & 0 & 0 & 0 & B_{io,N} & 0 \\ 0 & 0 & 0 & 0 & 0 & B_{in,N} \\ 0 & 0 & 0 & 0 & 0 & B_{out,N} \end{bmatrix}}_{=B_N} \begin{bmatrix} \widehat{S}_{11,N} \\ \widehat{S}_{12,N} \\ \widehat{S}_{22,N} \\ \widehat{u}_N \\ \widehat{v}_N \\ \widehat{p}_N \end{bmatrix} = \begin{bmatrix} 0 \\ 0 \\ 0 \\ p_{in} \\ 0 \end{bmatrix}, \qquad (49)$$

where:

- $B_{ud,N}$ is the $2(N+1) \times (N+1)^2$ matrix whose entries are equal to one at (i,i), with $i \in b_{up} \cup b_{down}$, and zero elsewhere;
- $B_{io,N}$ is the $2(N-1) \times (N+1)^2$ matrix whose entries are equal to one at (i,i), with $i \in b_{in} \cup b_{out}$, and zero elsewhere;
- $B_{in,N}$ is the $(N-1) \times (N+1)^2$ matrix whose entries are equal to one at (i,i), with $i \in b_{in}$, and zero elsewhere;
- $B_{out,N}$ is the $(N-1) \times (N+1)^2$ matrix whose entries are equal to one at (i,i), with $i \in b_{out}$, and zero elsewhere.

The matrix B_N has dimension $8N \times 6(N+1)^2$. On juxtaposing systems (48) and (49) we obtain an overdetermined nonlinear system of $6(N+1)^2 + 8N$ equations in $6(N+1)^2$ unknowns. Schematically this system can be written as

$$\mathbf{F}(\mathbf{X}) = \mathbf{0}, \qquad (50)$$

and it is solved via the Newton–Raphson algorithm.

$$\Big[\mathbf{J}(\mathbf{X}^n)\Big]\Delta\mathbf{X}^n = -\mathbf{F}(\mathbf{X}^n), \qquad \mathbf{X}^{n+1} = \mathbf{X}^n + \Delta\mathbf{X}^n, \qquad (51)$$

where $\mathbf{J}(\mathbf{X}^n)$ is the Jacobian of $\mathbf{F}(\mathbf{X})$ evaluated at iteration n. The matrix $\mathbf{J}(\mathbf{X}^n)$ is not square and $\Delta\mathbf{X}^n$ is a least-square solution of $(51)_1$. For convenience, the elements of the Jacobian matrix are reported in the appendix (see Section 5, page 92) . As initial guess for the Newton's method we take the rectilinear one dimensional axial flow (null transversal velocity) in the (ξ, η) domain, namely

$$\hat{u}(\xi, \eta) = \frac{1-\eta^2}{4}, \qquad \hat{v}(\xi, \eta) \equiv 0, \qquad \hat{p}(\xi, \eta) = p_{in}\frac{(1-\xi)}{2}. \tag{52}$$

It is worth remarking that $(51)_1$ can also be solved in the following way. Multiply the equation $(51)_1$ by $[\mathbf{J}(\mathbf{X}^n)]^T$ in order to obtain a square system whose solution can be sought by any iterative or direct method.

2.4 Lubrication approximation

When the aspect ratio δ is sufficiently "small" we may look for a solution of (30) that can be expressed as a power series of δ. Following [FFRV22] it is easy to check that at the leading order the momentum equation reduces to

$$(S_{12})_y = p_x = \Big[\mu(\dot{\gamma}) u_y\Big]_y, \qquad p_y = 0. \tag{53}$$

Hence

$$p = p(x), \qquad \dot{\gamma} = \frac{1}{2}\left|u_y\right|. \tag{54}$$

In what follows we shall limit our study to the upper part of the channel where

$$u_y \leqslant 0, \tag{55}$$

provided $p_{in} > 0$. The constitutive laws (26) and (27) are considered, and the zeroth-order solution in the original (x, y) coordinate system is determined. It is observed that, due to symmetry,

$$S_{12} = y\, p_x. \tag{56}$$

2.4.1 Case 1: regularized Bingham fluid

The Bingham apparent viscosity (26) is given by

$$\mu(\dot{\gamma}) = \left(1 + \frac{B}{-\dfrac{u_y}{2} + \varepsilon}\right). \tag{57}$$

Rearranging (53) with $\mu(\dot{\gamma})$ taken from (57) we get

$$(u_y)^2 - (2\varepsilon + 2B + yp_x)\, u_y + 2\varepsilon y p_x = 0, \tag{58}$$

which admits as solutions

$$(u_y)_{(1,2)} = f_{1,2}\,(p_x, y)\,, \tag{59}$$

$$f_{1,2} = \frac{1}{2}\left[(2\varepsilon + 2B + yp_x) \pm \sqrt{(2\varepsilon + 2B + yp_x)^2 - 8\varepsilon y p_x}\right]. \tag{60}$$

Nevertheless, the only physically acceptable solution is (in (55) we require that $u_y = 0$ when $y = 0$)

$$u_y = f_1\,(p_x, y) := f\,(p_x, y)\,, \tag{61}$$

$$f\,(p_x, y) := \frac{1}{2}\left[(2\varepsilon + 2B + yp_x) - \sqrt{(2\varepsilon + 2B + yp_x)^2 - 8\varepsilon y p_x}\right]. \tag{62}$$

Integration of (61) with the no-slip condition $(u(x, h(x)) = 0)$ provides the longitudinal velocity

$$u(x, y) = -\int_y^{h(x)} f\,(p_x, \tilde{y})\, d\tilde{y}, \qquad y \in [0, h(x)]. \tag{63}$$

Notice that in (63), the pressure is unknown at this stage. Exploiting mass balance and $(54)_1$ we find

$$v_y = -u_x = f\,(p_x, h)\, h_x + p_{xx} \int_y^{h(x)} \partial f(p_x, \tilde{y})\; d\tilde{y}, \tag{64}$$

where ∂f denotes the derivative of f with respect to p_x. Integrating (64) between 0 and $h(x)$ (given the no-slip condition at $y = h(x)$ and the symmetry condition on $y = 0$ for the transversal velocity v) we find:

$$0 = f\,(p_x, h)\, h h_x + p_{xx}\left[\int_0^{h(x)} \left(\int_y^{h(x)} \partial f(p_x, \tilde{y})\; d\tilde{y}\right) dy\right], \tag{65}$$

which is a second-order nonlinear integro-differential equation for the pressure. In conclusion, the task at hand is to solve the following nonlinear integro-differential boundary value problem (BVP):

$$
\begin{cases}
p_{xx} = -\dfrac{f\left(p_x,h\right)hh_x}{\left[\int_0^{h(x)}\left(\int_y^{h(x)}\partial f(p_x,\tilde{y})\;d\tilde{y}\right)dy\right]}, \\[2em]
p|_{x=-1} = p_{in}, \\[2em]
p|_{x=1} = 0.
\end{cases}
\tag{66}
$$

Once the pressure is found, the velocity components in the whole domain are given by

$$
u(x,y) = -\int_{|y|}^{h(x)} f\left(p_x,\tilde{y}\right)d\tilde{y}, \tag{67}
$$

$$
v(x,y) = \mathrm{sign}(y)\left[f(p_x,h)h_x(|y|-h) - p_{xx}\int_{|y|}^{h(x)}\left(\int_{\tilde{y}}^{h(x)}\partial f(p_x,\tilde{z})\;d\tilde{z}\right)d\tilde{y}\right]. \tag{68}
$$

2.4.2 Case 2: regularized Casson fluid

When the constitutive law is that of a Casson fluid (22), we proceed as in Bingham's case and find the equation equivalent to (58). Remembering (53), (54) and (55) we find:

$$
\left(\sqrt{-\frac{u_y}{2}}\right)^2 + \left(\sqrt{\epsilon}+\sqrt{B}-\sqrt{-\frac{p_x y}{2}}\right)\left(\sqrt{-\frac{u_y}{2}}\right) - \sqrt{-\frac{p_x\epsilon y}{2}} = 0. \tag{69}
$$

Here again, the possible solutions are

$$
\left(u_y\right)_{1,2} = g_{1,2}\left(p_x,y\right), \tag{70}
$$

where

$$g_{1,2}\left(p_x, y\right) = -\frac{1}{2}\left(\sqrt{\varepsilon} + \sqrt{B} - \sqrt{-\frac{p_x y}{2}}\right) + \\ \pm\frac{1}{2}\sqrt{\left(\sqrt{\varepsilon} + \sqrt{B} - \sqrt{-\frac{p_x y}{2}}\right)^2 + 4\sqrt{-\frac{p_x \varepsilon y}{2}}}. \tag{71}$$

As before, the only physically acceptable solution is

$$u_y = g_1(p_x, y) := g(p_x, y), \tag{72}$$

with

$$g := \frac{1}{2}\left[\left(\sqrt{\varepsilon} + \sqrt{B} - \sqrt{-\frac{y p_x}{2}}\right) + \right. \\ \left. - \sqrt{\left(\sqrt{\varepsilon} + \sqrt{B} - \sqrt{-\frac{y p_x}{2}}\right)^2 + 4\sqrt{-\frac{y \varepsilon p_x}{2}}}\right]^2. \tag{73}$$

Proceeding exactly as in (63), (64), (65) and considering the no-slip condition, the BVP for pressure now becomes:

$$\begin{cases} p_{xx} = -\dfrac{g\left(p_x, h_x\right) h h_x}{\left[\int_0^{h(x)} \left(\int_y^{h(x)} \partial g(p_x, \tilde{y})\, d\tilde{y}\right) dy\right]}, \\ \\ p|_{x=-1} = p_{in}, \\ \\ p|_{x=1} = 0. \end{cases} \tag{74}$$

The velocity field is again given by (67), (68) provided f is replaced by g, Both integro-differential systems (66), (74) are solved via spectral collocation exploiting Newton's iterative method.

Recalling (56) we may define the approximating yield surfaces $y = \pm\sigma$ imposing that $|S_{12}| = B$, i.e.

$$\pm\sigma(x) = \mp\frac{B}{p_x(x)}, \qquad \sigma(x) > 0. \tag{75}$$

2.4.3 Symmetry properties of the analytical solution

In this subsection we prove some properties of the analytical solution, i.e. for the zero order solution of the lubrication approximation. Although these properties are proved for the analytical solution, we shall see that they are maintained also for the general case of a channel with an aspect ratio not necessarily small (see the results in the numerical section). Moreover, the properties proved here are independent of the particular viscosity function, i.e. they hold true for any choice of $\mu(\dot\gamma)$. Indeed, all the propositions below are proved using the function f (which is related to the Bingham fluid viscosity), but they remain valid for any other regular viscosity function. We begin by proving the following:

Proposition 1. *At any cross section $\bar{x}$ such that $h_x(\bar{x}) = 0$, the transversal velocity v is such that $v(\bar{x}, y) \equiv 0$ for all $y \in [-h(\bar{x}), h(\bar{x})]$.*

Proof. From (65) we notice that, at any point $\bar{x}$ such that $h_x = 0$, we have that necessarily $p_{xx} = 0$. Hence, from (64) $v_y \equiv 0$ for any y at such a point. Recalling that $v = 0$ at $y = h$ we find that $v \equiv 0$ at any cross section $\bar{x}$ such that $h_x = 0$. In other words we can say that, at any cross section in which the channel profile changes its monotonicity (or simply becomes flat) the transversal velocity must be null. This is confirmed by numerical simulations. □

Proposition 2. *If the channel profile $h(x)$ is an even function, then the pressure gradient $p_x(x)$ is also an even function. As a consequence, $u(x, y)$ is even in x and even in y, $v(x, y)$ is odd in x and odd in y, $S_{12}(x, y)$ is even in x and odd in y and $\sigma(x)$ is even in x.*

Proof. Equation (65) can be rewritten as

$$-hh_x = \int_0^h dy \int_y^h \frac{\Big[f(p_x, \tilde{y})\Big]_x}{f(p_x, h)} d\tilde{y}. \tag{76}$$

Since the left hand side of the above is odd in x (h is even and hence h_x is odd), assuming that the quotient under the integral sign is irreducible (we can always eliminate the common factor), we have only two situations:

$$\text{(C1)} \qquad \Big[f(p_x, \tilde{y})\Big]_x \ \ \text{(odd in } x\text{)}, \qquad f(p_x, h) \ \ \text{(even in } x\text{)}, \tag{77}$$

$$\text{(C2)} \qquad \Big[f(p_x, \tilde{y})\Big]_x \ \ \text{(even in } x\text{)}, \qquad f(p_x, h) \ \ \text{(odd in } x\text{)}. \tag{78}$$

In the case (C1), since $f(p_x, h)$ is even, we necessarily have that p_x is even in x and the proof in concluded. In the case (C2) $f(p_x, h)$ is odd, so that

$$f\Big(p_x(-x), h(x)\Big) = -f\Big(p_x(x), h(x)\Big), \tag{79}$$

because $h(-x) = h(x)$. Relation (79) implies that

$$f\Big(p_x(-x), y\Big) = -f\Big(p_x(x), y\Big), \tag{80}$$

i.e. $f(p_x, y)$ is odd (indeed its derivative in x must be even). As a consequence $f(p_x(0), y) = 0$ for all $y \in [-h(0), h(0)]$. Hence from (61) and from the no-slip condition on u we get

$$u_y(0, y) = f(p_x(0), y) \equiv 0, \quad \Longrightarrow \quad u(0, y) = 0, \qquad \forall \ \ y \in [-h(0), h(0)]. \tag{81}$$

It is straightforward to show that the above leads to a contradiction. Indeed, defining the discharge

$$Q(x) = \int_{-h(x)}^{h(x)} u(x, y) dy, \tag{82}$$

and recalling mass balance and the no-slip condition, we find

$$Q_x = \int_{-h(x)}^{h(x)} u_x(x, y) dy = -\int_{-h(x)}^{h(x)} v_y(x, y) dy = 0. \tag{83}$$

Therefore

$$0 = Q(0) = \int_{-h(0)}^{h(0)} \underbrace{u(0, y)}_{=0} dy = Q(x), \tag{84}$$

i.e. the discharge is identically null on each cross section or, in other words, $u(x, y) \equiv 0$ in the whole domain. From (61), (62) we find that, if $u \equiv 0$ then $p_x \equiv$

0, i.e. $p = const$, which is compatible with the boundary conditions $p(-1) = p_{in}$, $p(1) = 0$ only if $p_{in} = 0$. Therefore, for any $p_{in} > 0$ only (C1) can be true. The symmetries for u, v, S_{12} and σ follow from the definitions (67), (68), (56), (75). This concludes the proof of Proposition 2. □

Proposition 3. *Let us consider the problems with channel walls $h(x)$ and $\bar{h}(x)$, with $\bar{h}(x) = h(-x)$ (even reflection). Let us denote by (u, v, p), $(\bar{u}, \bar{v}, \bar{p})$ the relative solutions and let us assume that the boundary conditions for the pressure are the same for both problems, i.e.*

$$p(-1) = p_{in}, \qquad p(1) = 0, \qquad\qquad \bar{p}(-1) = p_{in}, \qquad \bar{p}(1) = 0. \tag{85}$$

Then

$$\begin{cases} \bar{u}(x,y) = u(-x,y), \\ \\ \bar{v}(x,y) = -v(-x,y), \\ \\ \bar{p}(x) = p_{in} - p(-x), \\ \\ \bar{S}_{12}(x,y) = S_{12}(-x,y), \\ \\ \bar{\sigma}(x) = \sigma(-x). \end{cases} \tag{86}$$

Proof. Suppose $p(x)$ is a solution of (66). Then, also $p(x) + k$ (with $k \in \mathbb{R}$) is a solution with boundary conditions $p_{in} + k$ at $x = -1$ and k at $x = 1$. Hence the pressure gradient p_x depends only on the pressure drop $\Delta p = p_{in} - 0 = p_{in}$. The function $\tilde{p}(x) = p(x) - p_{in}$ thus satisfies the problem

$$\begin{cases} \tilde{p}_{xx} = -\dfrac{f\left(\tilde{p}_x, h\right) h h_x}{\left[\int_0^{h(x)} \left(\int_y^{h(x)} \partial f(\tilde{p}_x, \tilde{y})\, d\tilde{y}\right) dy\right]}, \\ \\ \tilde{p}|_{x=-1} = 0, \\ \\ \tilde{p}|_{x=1} = -p_{in}. \end{cases} \tag{87}$$

With respect to the pressure $\tilde{p}(x)$, the velocity components remain unchanged, namely $\tilde{u}(x,y) = u(x,y)$, $\tilde{v}(x,y) = v(x,y)$, since $\tilde{p}_x = p_x$. Now consider the new channel profile and the new pressure

$$\begin{cases} \bar{h}(x) = h(-x), \qquad \text{(even reflection)}, \\ \\ \bar{p}(x) = -\tilde{p}(-x) = p_{in} - p(-x). \end{cases} \tag{88}$$

It is straightforward to verify that

$$\bar{p}_x(x) = \tilde{p}_x(-x) = p_x(-x), \tag{89}$$

$$\bar{p}_{xx}(x) = -\tilde{p}_{xx}(-x) = -p_{xx}(-x), \tag{90}$$

and that $\bar{p}(x)$ satisfies

$$\begin{cases} \bar{p}_{xx} = -\dfrac{f\left(\bar{p}_x, \bar{h}\right) \bar{h} \bar{h}_x}{\left[\int_0^{\bar{h}(x)} \left(\int_y^{\bar{h}(x)} \left(f(\bar{p}_x, \tilde{y})\right)_{\bar{p}_x}\, d\tilde{y}\right) dy\right]}, \\ \\ \bar{p}|_{x=-1} = p_{in}, \\ \\ \bar{p}|_{x=1} = 0. \end{cases} \tag{91}$$

Therefore $\bar{p}(x)$ represents the pressure field for the channel with profile $\bar{h}(x)$ at the zero order approximation. Now consider the solution $\bar{u}(x, y)$ relative to $\bar{p}_x$. We find

$$\bar{u}(x,y) = -\int_{|y|}^{\bar{h}(x)} f\left(\bar{p}_x(x), \tilde{y}\right) d\tilde{y} = -\int_{|y|}^{h(-x)} f\left(p_x(-x), \tilde{y}\right) d\tilde{y} = u(-x, y), \quad (92)$$

which proves that $\bar{u}(x, y) = u(-x, y)$, i.e. the first of (86). Proceeding in the same way for $\bar{v}(x, y)$ (see (68)) one can easily find that $\bar{v}(x, y) = -v(-x, y)$, i.e. the second of (86). Recalling the definition of $\tilde{p}(x)$ and $\bar{p}(x)$ we also verify that $\bar{p}(x) = p_{in} - \tilde{p}(-x) = p_{in} - p(-x)$, i.e. the third of (86). The fourth and fifth of (86) comes directly from (56), (75) and the proof is concluded. $\square$

2.5 Numerical simulations and discussion

In this section, we present the numerical results obtained solving the discretized problem (44), (45) by the spectral collocation method introduced earlier. We also compare the numerical solution with the analytical solution that can be found when the aspect ratio δ is "small" (asymptotic solution). The aim of these numerical simulations is to visualize the position of the yield surfaces within the flow. The identification of these interfaces is of crucial importance, because it allows one to discriminate between the "rigid" and fluid zone. We recall that the yield surface of a regularized viscoplastic fluid is not a "true" yield surface, because in the regularized model a "real" unyielded region does not exist. The comparison with the available analytical solution is also very important, since it allows us to validate our numerical scheme.

In all the simulations the dimension of the collocation grid is $(N+1)\times(N+1)$ with $N = 20$. An increase of N does not affect significantly the accuracy of the solution. In what follows the regularization parameter is $\varepsilon = 0.01$. We consider three different channel profiles, namely:

$$\textit{Profile 1 (non-monotone):} \qquad h = 1 - \frac{1}{5}\sin\left[\frac{\pi}{2}(x+1)\right]; \tag{93}$$

$$\textit{Profile 2 (divergent):} \qquad h = \frac{4}{5} - \frac{1}{5}\cos\left[\frac{\pi}{2}(x+1)\right]; \tag{94}$$

$$\textit{Profile 3 (convergent):} \qquad h = \frac{4}{5} + \frac{1}{5}\cos\left[\frac{\pi}{2}(x+1)\right]. \tag{95}$$

The choice of the three profiles is made to visualize the yield surface behavior in case of a divergent, convergent and non-monotone wall functions. We do not have a specific application in mind, so we try to remain as general as possible considering three different types of monotonicity of the channel walls. Since we are dealing with viscoplastic fluids, we have considered two of the mostly used viscoplastic models: the Bingham and the Casson model. We begin by considering an aspect ratio $\delta = 1$. In Figs 13, 15, 17 we plot the yield surfaces $|\mathbb{S}| = B$ for the Bingham flow for $B = 0.1, 0.2, 0.5, 0.8, 1$. In Figs 14, 16, 18 we plot the yield surfaces $|\mathbb{S}| = B$ for the Casson flow with the same values of B. In both cases $p_{in} = 2.5$. Figs 13, 14 are relative to profile 1, Figs 15, 16 are relative to profile 2, Figs 17, 18 are relative to profile 3. We notice that, for fixed B and p_{in} the unyielded region of the Casson fluid is "slightly" larger than that of the Bingham fluid. As observed in Remark 1, there is always an unyielded region in proximity of the points $(\pm 1, 0)$. This is evident in all Figs 13-18. For "small" values of B these regions are not connected (separated isles), but as B is increased they join together becoming a unique unyielded central core. As B is increased further, the unyielded region expands, eventually occupying the whole domain (for sufficiently large values of B). In case $h(x)$ is given by profile 1 (symmetric with respect to the y axis), we notice also the presence of a separated unyielded isle centered in $(0,0)$ for small B, see Figs 13, 14. The presence of this central unyielded isle, which is not present in the case of profiles 2 and 3 no matter how small B is, is due to the fact that $h_x(0) = 0$. Indeed, from Proposition 1, we know that $v(0,y) \equiv 0$ if $h_x(0) = 0$ (actually we have proved this property for δ when it becomes small, but let us suppose here that Proposition 1 holds true for any δ). This means that $v_y(0,y) \equiv -u_x(0,y) \equiv 0$. Recalling that, because of symmetry, $u_y(x,0) \equiv v_x(x,0) \equiv 0$ it is easy to verify that $\dot{\gamma}(0,0) = 0$. Hence, there must

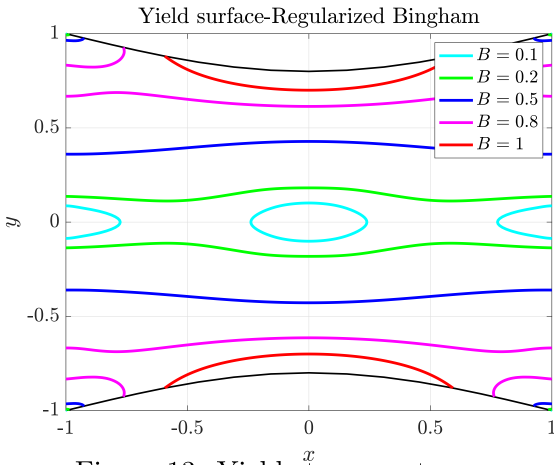

Figure 13: Yield stress contour: profile 1; $p_{in} = 2.5$, $\delta = 1$ (Bingham).

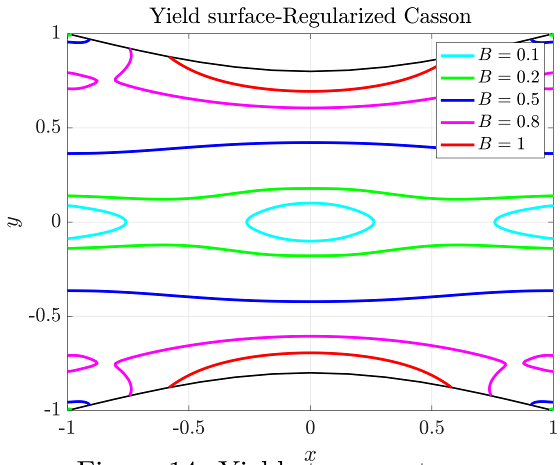

Figure 14: Yield stress contour: profile 1; $p_{in} = 2.5$, $\delta = 1$ (Casson).

be a neighborhood of $(0, 0)$ in which the fluid is seemingly unyielded (as evident from Figs. 13, 14). When considering profiles 2 and 3 the wall function is such that $h_x(x) \neq 0$ for all $x \in (-1, 1)$ and no internal unyielded region is present, irrespectively of the smallness of B.

Indicating the dependence of the tensor $\mathbb{S}$ on the Bingham number B, i.e. $\mathbb{S}(x, y; B)$ (the solution of the flow problem clearly depends on B) and defining the unyielded domain

$$\Omega_B = \Big\{ (x, y) \in \Omega : \ |\mathbb{S}(x, y; B)| \leqslant B \Big\} \subseteq \Omega, \tag{96}$$

with

$$\Omega = \Big\{ (x, y) : \ x \in [-1, 1], \quad y \in [-h(x), h(x)] \Big\}, \tag{97}$$

being the flow domain, we have that the function

$$\mathcal{F}(B) = \text{ measure } (\Omega_B) : [0, \infty) \to [0, \text{measure}(\Omega)], \tag{98}$$

is a non decreasing function of B bounded from above by measure(Ω). Physically, this means that the "unyielded" part of the fluid enlarges as the yield limit τ_y^* increases, and this is physically expected.

In Figs. 19-24 we plot the yield surfaces $|\mathbb{S}| = B$ keeping B fixed and letting p_{in} vary. We take $\delta = 1$ and $B = 0.5$. Figs 19, 20 are relative to profile 1, Figs. 21, 22 are relative to profile 2, Figs. 23, 24 are relative to profile 3. The inlet

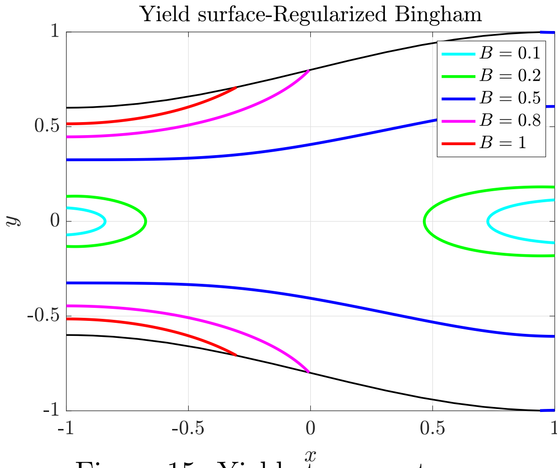

Figure 15: Yield stress contour: profile 2; $p_{in} = 2.5$, $\delta = 1$ (Bingham).

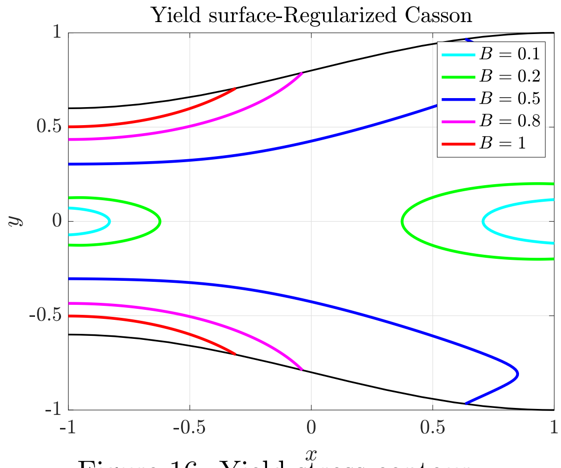

Figure 16: Yield stress contour: profile 2; $p_{in} = 2.5$, $\delta = 1$ (Casson).

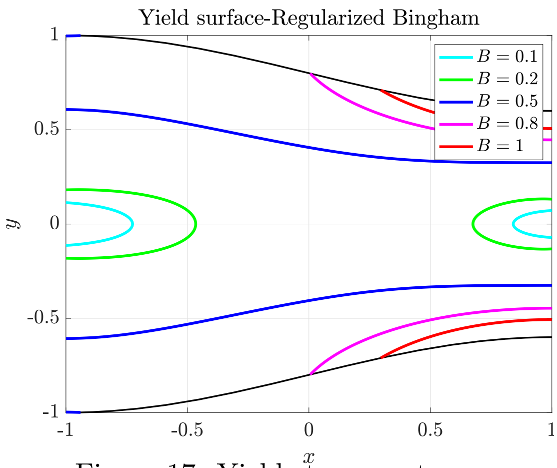

Figure 17: Yield stress contour: profile 3; $p_{in} = 2.5$, $\delta = 1$ (Bingham).

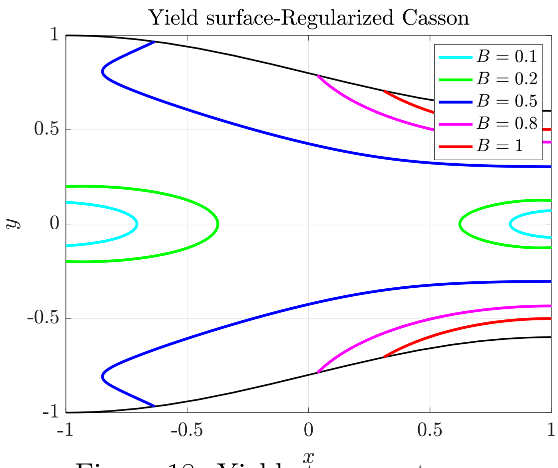

Figure 18: Yield stress contour: profile 3; $p_{in} = 2.5$, $\delta = 1$ (Casson).

pressure values are $p_{in} = 1.2, 3, 5, 8$. Looking at Figs 19-24 we observe that the increase of the pressure results in an expansion of the yielded region, as physically expected (the overall stress becomes larger as the pressure drop p_{in} is increased). The behavior of the unyielded isles centered in $(\pm 1, 0)$ (and also in $(0, 0)$ in the case of profile 1) is the same of that depicted in Figs. 13-18 (i.e. for varying B). These separated isles are formed for "sufficiently" large p_{in}, while for smaller values of p_{in} they are connected in a unique central core. Although the unyielded isles are always present for any value of p_{in} (no matter how large), there exists a threshold value for p_{in} (approximately equal to 1) below which the entire fluid domain becomes unyielded. As in the previous cases, here the unyielded region, for fixed B and p_{in} is larger in the Casson fluid. Analogously to the case of varying B, we may now indicate the dependence of the stress $\mathbb{S}$ on p_{in} and write

$$\Omega_{p_{in}} = \Big\{ (x, y) \in \Omega : \ |\mathbb{S}(x, y; p_{in})| \leqslant B \Big\} \subseteq \Omega, \tag{99}$$

where now B is fixed. The function

$$\mathcal{G}(p_{in}) = \text{ measure } (\Omega_{p_{in}}) : [0, \infty) \to [0, \text{measure}(\Omega)] \tag{100}$$

is now a non-increasing function bounded from above by the value $\hat{F} = \text{measure}(\Omega)$. From the physical point of view, we have proven that when the applied force (pressure drop) is increased the yielded part of the fluid enlarges because the overall stress in the fluid becomes larger. In this case the isles centered at the inlet and outlet of the channel becomes smaller. The critical pressure drop at which the domain becomes essentially yielded depends, of course, on the specific value of the yield stress. In other words, the larger is the yield stress the larger is the pressure drop needed to yield the fluid in the whole domain.

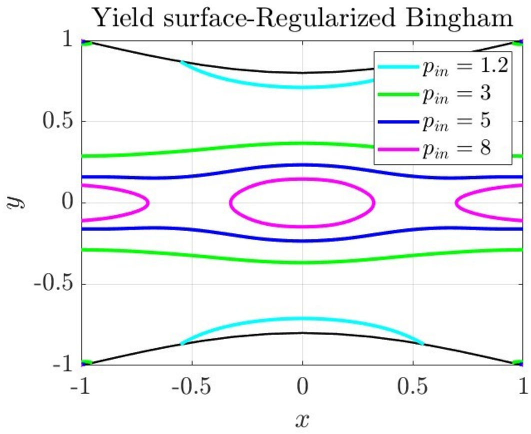

Figure 19: Yield stress contour: profile 1; $B_{in} = 0.5$, $\delta = 1$ (Bingham).

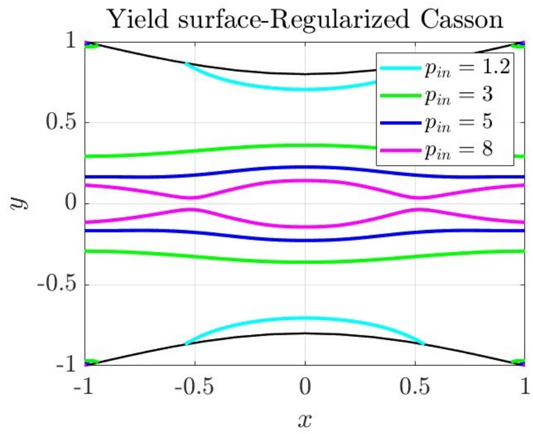

Figure 20: Yield stress contour: profile 1; $B = 0.5$, $\delta = 1$ (Casson).

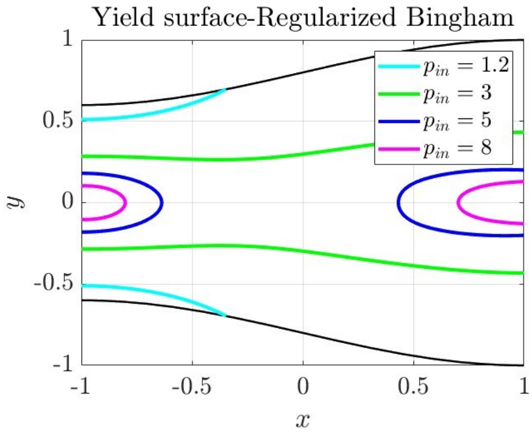

Figure 21: Yield stress contour: profile 2; $B_{in} = 0.5$, $\delta = 1$ (Bingham).

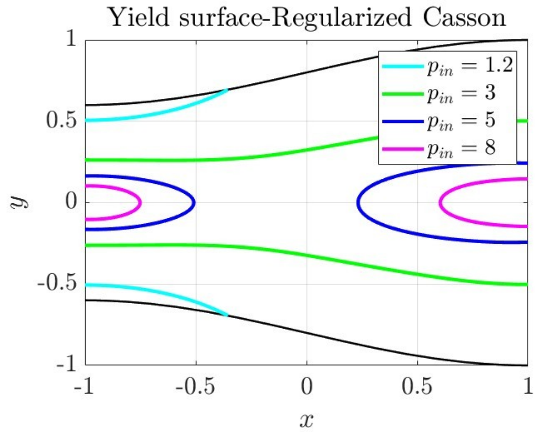

Figure 22: Yield stress contour: profile 2; $B = 0.5$, $\delta = 1$ (Casson).

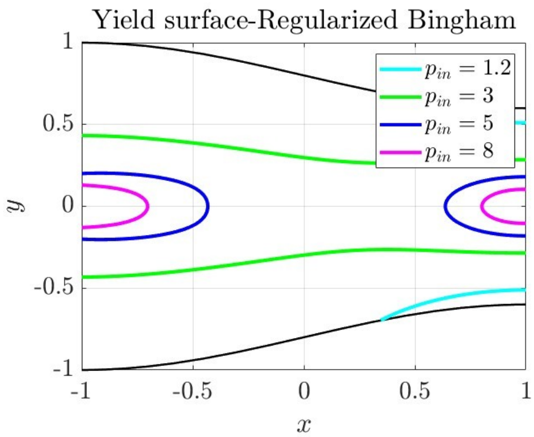

Figure 23: Yield stress contour: profile 3; $B_{in} = 0.5$, $\delta = 1$ (Bingham).

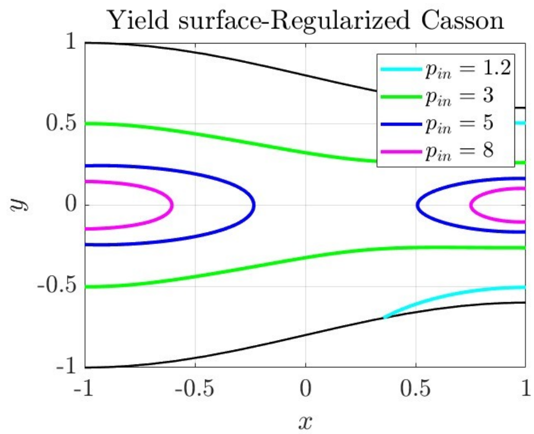

Figure 24: Yield stress contour: profile 3; $B = 0.5$, $\delta = 1$ (Casson).

Finally, the numerical solution will now be juxtaposed with the lubrication solution established in Section 2.4. This comparison aims to validate the numerical scheme. Beginning with an examination of the approximating yield surfaces, we will plot both the numerical (continuous) and analytical (stars) yield surfaces for the Bingham and Casson flows across various values of B (see Figs. 25 and 26). The pressure drop is $p_{in} = 5$. It is immediately noticeable that for small δ (lubrication flow), the monotonicity of the yield surface matches that of the channel profile, as shown in Figs 25 and 26. This is not true if $\delta \in O(1)$, as evident from Figs. 23, 24. From (75), it can be observed that the zero-order solution does not permit the formation of non-connected unyielded regions (isles), and $\sigma(x) > 0$.

In Figs 27 and 28, the numerical (continuous) and analytical (stars) longitudinal velocities are plotted at cross sections $x = -0.5878, 0.1564, 0.8090$. Here, $B = 1$, $p_{in} = 15$, and $\delta = 0.01$ For the sake of simplicity, only one profile has been considered, and comparison plots of the transversal velocity and pressure have not been included, but the results are analogous to those of the axial velocity, see Figs 27 and 28. It is observed that, at any cross-section, the axial velocity resembles the classical 'flat' profile of viscoplastic flows. This is more evident in the Bingham flow than in the Casson flow. The "flatness" of the velocity depends on the pressure drop. The larger the pressure drop p_{in}, the "flatter" the velocity profile in the unyielded region.

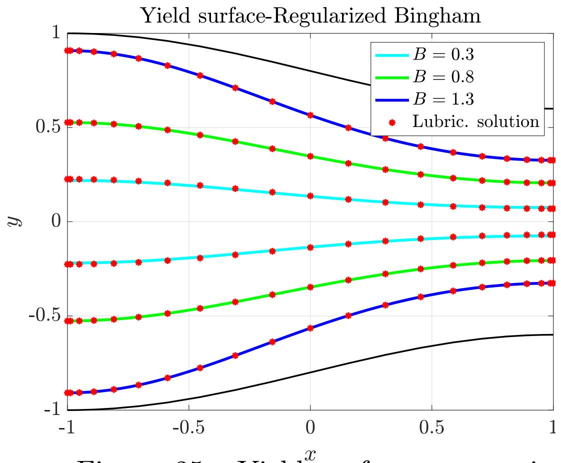

Figure 25: Yield surfaces comparison: numerical (continuous), analytical (starred), profile 3, $p_{in} = 5$, $\delta = 0.01$ (Bingham).

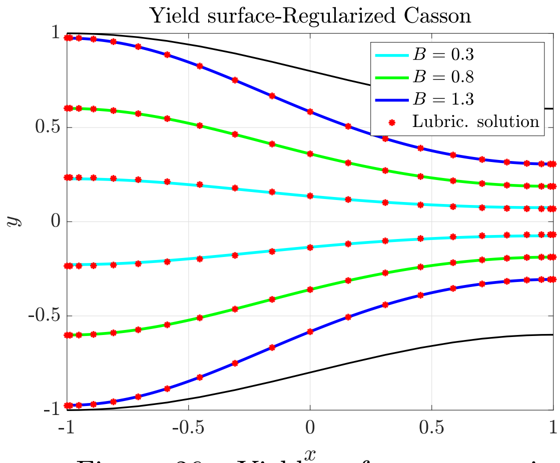

Figure 26: Yield surfaces comparison: numerical (continuous), analytical (starred), profile 3, $p_{in} = 5$, $\delta = 0.01$ (Casson).

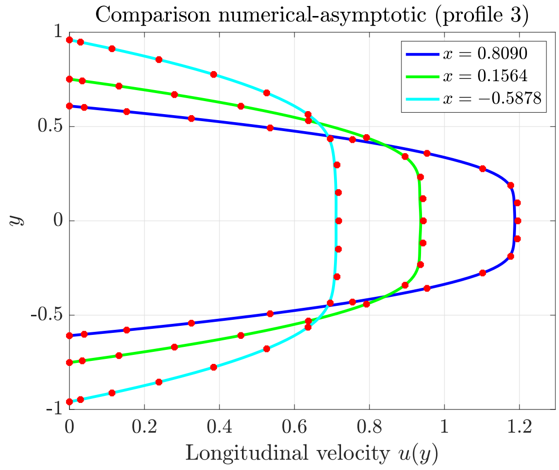

Figure 27: Axial velocity u comparison at different cross sections: numerical (continuous), analytical (starred), profile 3, $p_{in} = 15$, $B = 1$, $\delta = 0.01$, (Bingham).

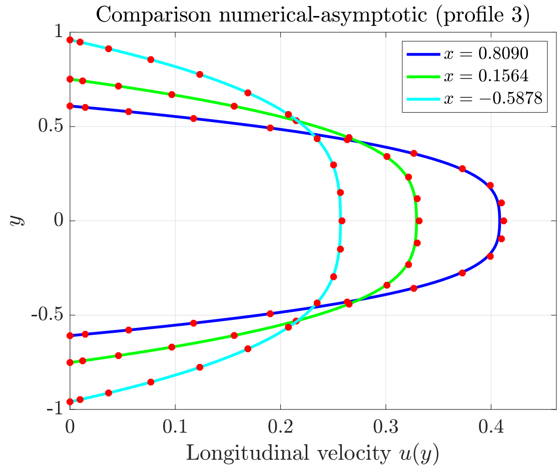

Figure 28: Axial velocity u comparison at different cross sections: numerical (continuous), analytical (starred), profile 3, $p_{in} = 15$, $B = 1$, $\delta = 0.01$, (Casson).

2.6 Extension of the results to the steady and unsteady generalized Navier-Stokes case

In this section, the results previously obtained will be extended. Specifically, the case in which the system (29) is in a steady state ($\partial_t \mathbf{v} = \mathbf{0}$) but includes the nonlinear term $\nabla \mathbf{v}[\mathbf{v}]$ will first be considered. Subsequently, the non-steady state case will also be examined. For this purpose, it is necessary to introduce additional terms into the *Jacobian matrix* to account for the nonlinear component of the generalized Navier-Stokes system. For the sake of clarity, the complete system of governing equations, boundary conditions and initial conditions is presented below:

$$
\begin{cases}
Re\delta\left(u_t + u_x u + u_y v\right) = -p_x + \delta(S_{11})_x + (S_{12})_y, \\
Re\delta^3\left(v_t + v_x u + v_y v\right) = -p_y + \delta^2(S_{12})_x + \delta(S_{22})_y, \\
S_{11} = 2\delta\mu\left(\dot{\gamma}\right) u_x, \\
S_{12} = \mu\left(\dot{\gamma}\right)\left(u_y + \delta^2 v_x\right), \\
S_{22} = 2\delta\mu\left(\dot{\gamma}\right) v_y, \\
u_x + v_y = 0, \\
u|_{y=\pm h(x)} = v|_{y=\pm h(x)} = 0, \\
p|_{x=-1} = p_{in}, \qquad p|_{x=1} = 0, \qquad v|_{x=\pm 1} = 0, \\
u(x,y,t)|_{t=0} = u_0(x,y), \quad v(x,y,t)|_{t=0} = v_0(x,y),
\end{cases}
\tag{101}
$$

where Re represents the Reynolds number defined immediately after equation (29). Consider the steady-state case of (101), in which $\partial_t \mathbf{v} = \left(u_t,\ v_t\right)^T = \mathbf{0}$. The system (44) can no longer be reformulated in a simple manner (keeping the intrinsic nonlinearity of the system solely in the viscosity μ). Indeed, at most, we can only rewrite the system (101) by replacing the partial derivatives with respect to x and y with the operators P_1 and P_2 respectively (see equations (38)). It is evident that the Jacobian matrix (see Section 5) is enriched with terms due to partial derivatives with respect to u and v in the first two equations (specifically, there will be three additional terms on element J_{14} and one additional term on element J_{15}, and similarly, three additional terms on element J_{25} and one additional term on element J_{24}). The overall complexity of the system increases, also from the perspective of the application of spectral collocation methods. For everything else (implementation of boundary conditions, matrix block sizes, etc.), what was stated in Section 2.3 still holds true. To validate the new code, reference was made to Reynolds numbers $Re = 0.1,\ 1,\ 10,\ 100,\ 150$, and the relative difference between the solution of the Stokes problem (Sp) obtained with the code used in the previous sections, and that of the steady Navier-Stokes problem ($sNSp$) was calculated.

The *maximum relative percentage difference* was calculated for the fundamental components of the velocity field u and v, and for the pressure p, excluding the boundary nodes where boundary conditions are assigned. Specifically, the following sup norm was used:

$$\left\| \frac{(u_{(Sp)}, v_{(Sp)}, p_{(Sp)}) - (u_{(sNSp)}, v_{(sNSp)}, p_{(sNSp)})}{(u_{(Sp)}, v_{(Sp)}, p_{(Sp)})} \right\|_\infty \cdot 100, \tag{102}$$

In particular, to evaluate the relative norm for the velocity component v, boundary nodes and nodes where, due to the antisymmetry proven in Section 2.4.3, $v(x, y) = 0$ were not considered (typically on the $y = 0$ axis and in the case of *profile 1*, doubly symmetric, also the $x = 0$ axis); for the velocity component u, nodes on $y = \pm h(x)$ were not considered; for the pressure p, nodes on the $x = \pm 1$ axes were not considered. In light of these considerations, and for the sake of brevity, the results of the maximum relative percentage differences of the velocity components u, v, and pressure p as the Reynolds number varies for Bingham and then Casson fluids are given below, with parameters $B = 0.1$, $\delta = 0.1$, $p_{in} = 1$ and $p_{out} = 0$. To compute the components mentioned above, the formula (102) will be used.

Re	u-relative error	v-relative error	p-relative error
0.1	$1.3 \cdot 10^{-2}$	$7.6 \cdot 10^{-2}$	$4.1 \cdot 10^{-2}$
1	$1.4 \cdot 10^{-1}$	$7.5 \cdot 10^{-1}$	$4.0 \cdot 10^{-1}$
10	1.3	8.0	3.9
100	$1.4 \cdot 10$	$1.1 \cdot 10^2$	$6.3 \cdot 10$
150	$2.0 \cdot 10$	$1.3 \cdot 10^2$	$1.1 \cdot 10^2$

Table 1: Relative error between Sp and sNSp in the regularized Bingham fluid case: *Profile 1*

Re	u-relative error	v-relative error	p-relative error
0.1	$2.2 \cdot 10^{-2}$	$6.9 \cdot 10^{-2}$	$2.6 \cdot 10^{-2}$
1	$2.1 \cdot 10^{-1}$	$7.0 \cdot 10^{-1}$	$2.4 \cdot 10^{-2}$
10	2.3	7.3	2.7
100	$3.3 \cdot 10$	$9.9 \cdot 10$	$5.5 \cdot 10$
150	$4.1 \cdot 10$	$1.5 \cdot 10^{2}$	$1.1 \cdot 10^{2}$

Table 2: Relative error between Sp and sNSp in the regularized Bingham fluid case: *Profile 2*

Re	u-relative error	v-relative error	p-relative error
0.1	$2.0 \cdot 10^{-2}$	$3.9 \cdot 10^{-2}$	$2.0 \cdot 10^{-2}$
1	$2.2 \cdot 10^{-1}$	$3.8 \cdot 10^{-1}$	$1.9 \cdot 10^{-1}$
10	2.1	3.7	1.8
100	$1.6 \cdot 10$	$2.7 \cdot 10$	$1.4 \cdot 10$
150	$2.1 \cdot 10$	$3.4 \cdot 10$	$2.5 \cdot 10$

Table 3: Relative error between Sp and sNSp in the regularized Bingham fluid case: *Profile 3*

Re	u-relative error	v-relative error	p-relative error
0.1	$1.5 \cdot 10^{-2}$	$2.7 \cdot 10^{-2}$	$4.1 \cdot 10^{-2}$
1	$1.4 \cdot 10^{-1}$	$2.6 \cdot 10^{-1}$	$4.0 \cdot 10^{-1}$
10	1.5	2.8	4.2
100	$1.9 \cdot 10$	$3.3 \cdot 10$	$5.5 \cdot 10$
150	$4.2 \cdot 10$	$4.3 \cdot 10$	10^{2}

Table 4: Relative error between Sp and sNSp in the regularized Casson fluid case: *Profile 1*

Re	u-relative error	v-relative error	p-relative error
0.1	$7.6 \cdot 10^{-3}$	$2.0 \cdot 10^{-2}$	$1.1 \cdot 10^{-2}$
1	$7.4 \cdot 10^{-2}$	$1.9 \cdot 10^{-1}$	$1.0 \cdot 10^{-1}$
10	$7.7 \cdot 10^{-1}$	2.1	1.2
100	9.0	$2.9 \cdot 10$	$1.1 \cdot 10$
150	$1.4 \cdot 10$	$4.5 \cdot 10$	$2.2 \cdot 10$

Table 5: Relative error between Sp and sNSp in the regularized Casson fluid case: *Profile 2*

Re	u-relative error	v-relative error	p-relative error
0.1	$1.5 \cdot 10^{-2}$	$1.4 \cdot 10^{-2}$	$9.0 \cdot 10^{-3}$
1	$1.5 \cdot 10^{-1}$	$1.3 \cdot 10^{-1}$	$1.0 \cdot 10^{-2}$
10	1.4	1.5	$9.1 \cdot 10$
100	$1.2 \cdot 10$	$1.7 \cdot 10$	8.5
150	$1.6 \cdot 10$	$2.5 \cdot 10$	$1.1 \cdot 10$

Table 6: Relative error between Sp and sNSp in the regularized Casson fluid case: *Profile 3*

It is possible to observe that as Re increases, the non-linear convective term gains greater importance, albeit in different ways among the various velocity components and pressure. Furthermore, this behavior is generally more pronounced for regularized Bingham fluids, where for example, at $Re = 150$ and *profile 3*, relative percentage differences of 21%, 34%, and 25% are observed for the velocity components u, v, and pressure p, respectively, in the Bingham case, compared to only 16%, 25%, and 11% for the Casson case.

2.6.1 Unsteady planar flow

The complete system (101) will now be addressed. For temporal discretization, the *Crank-Nicolson method* is utilized (see [CN47], [QSS06]), considering the initial condition $u_0 = v_0 = p_0 = 0$. In this context, the comparison will be made with the steady-state solution of (101), using the same profiles and parameters, choosing the most appropriate final time (T_f) to reach the steady-state solution, and an adequate time step for discretization. As in the previous case, the relative differences between the results of the new code that solves the unsteady generalized Navier-Stokes problem (*uNSp*) and the stationary generalized Navier-Stokes case will be tabulated. These differences can be considered *relative errors* between the two cases, as for sufficiently large times, the unsteady solution must tend to the steady-state solution.

Re	T_f/ dt	u-relative error	v-relative error	p-relative error
0.1	1 / 0.05	$3.2 \cdot 10^{-1}$	$6.5 \cdot 10^{-1}$	$204 \cdot 10^{-1}$
1	3 / 0.25	$1.2 \cdot 10^{-1}$	$6.3 \cdot 10^{-2}$	$4.5 \cdot 10^{-2}$
10	10 / 0.40	$9.0 \cdot 10^{-2}$	$6.1 \cdot 10^{-2}$	$5.0 \cdot 10^{-2}$
100	100 / 0.5	$1.1 \cdot 10^{-1}$	$3.5 \cdot 10^{-1}$	$1.0 \cdot 10^{-1}$
150	150 / 0.5	$1.4 \cdot 10^{-1}$	$3.8 \cdot 10^{-1}$	$5.3 \cdot 10^{-1}$

Table 7: Relative error between uNSp and sNSp in the regularized Bingham fluid case (B $= 0.1,\ \delta = 0.1,\ \varepsilon = 0.01,\ p_{in} = 1,\ p_{out} = 0$): *Profile 1*

Re	T_f/ dt	u-relative error	v-relative error	p-relative error
0.1	1 / 0.05	$5.0 \cdot 10^{-1}$	$1.0 \cdot 10^{-1}$	$1.8 \cdot 10^{-1}$
1	1 / 0.05	$2.3 \cdot 10^{-1}$	$1.2 \cdot 10^{-2}$	$2.2 \cdot 10^{-2}$
10	10 / 0.25	$1.1 \cdot 10^{-2}$	$1.3 \cdot 10^{-2}$	$6.1 \cdot 10^{-3}$
100	100 / 0.33	$1.0 \cdot 10^{-1}$	$2.2 \cdot 10^{-2}$	$6.4 \cdot 10^{-2}$
150	150 / 0.38	$1.7 \cdot 10^{-1}$	$2.0 \cdot 10^{-2}$	$9.2 \cdot 10^{-2}$

Table 8: Relative error between uNSp and sNSp in the regularized Bingham fluid case (B $= 0.1,\ \delta = 0.1,\ \varepsilon = 0.01,\ p_{in} = 1,\ p_{out} = 0$): *Profile 2.*

Re	T_f/ dt	u-relative error	v-relative error	p-relative error
0.1	1 / 0.03	$5.5 \cdot 10^{-2}$	$1.1 \cdot 10^{-2}$	$1.0 \cdot 10^{-1}$
1	1 / 0.20	$6.0 \cdot 10^{-3}$	$1.2 \cdot 10^{-2}$	$1.0 \cdot 10^{-2}$
10	10 / 0.33	$1.3 \cdot 10^{-2}$	$1.2 \cdot 10^{-1}$	$8.7 \cdot 10^{-3}$
100	100 / 0.5	$9.6 \cdot 10^{-2}$	$1.4 \cdot 10^{-2}$	$3.1 \cdot 10^{-2}$
150	150 / 0.5	$1.5 \cdot 10^{-1}$	$2.2 \cdot 10^{-2}$	$4.4 \cdot 10^{-2}$

Table 9: Relative error between uNSp and sNSp in the regularized Bingham fluid case (B $= 0.1,\ \delta = 0.1,\ \varepsilon = 0.01,\ p_{in} = 1,\ p_{out} = 0$): *Profile 3.*

Re	T_f/ dt	u-relative error	v-relative error	p-relative error
0.1	1 / 0.03	$3.2 \cdot 10^{-2}$	$8.1 \cdot 10^{-3}$	$2.6 \cdot 10^{-3}$
1	1 / 0.05	$4.8 \cdot 10^{-2}$	$7.6 \cdot 10^{-3}$	$6.0 \cdot 10^{-3}$
10	10 / 0.25	$2.6 \cdot 10^{-2}$	$1.7 \cdot 10^{-2}$	$5.3 \cdot 10^{-3}$
100	100 / 0.33	$1.7 \cdot 10^{-1}$	$1.3 \cdot 10^{-1}$	$5.4 \cdot 10^{-2}$
150	150 / 0.38	$2.6 \cdot 10^{-1}$	$1.9 \cdot 10^{-1}$	$9.5 \cdot 10^{-2}$

Table 10: Relative error between uSNp and sNSp in the regularized Casson fluid case (B $= 0.1,\ \delta = 0.1,\ \varepsilon = 0.01,\ p_{in} = 1,\ p_{out} = 0$): *Profile 1.*

Re	T_f/ dt	u-relative error	v-relative error	p-relative error
0.1	1 / 0.05	$8.8 \cdot 10^{-1}$	$1.6 \cdot 10^{-2}$	$3.8 \cdot 10^{-1}$
1	1 / 0.05	$6.8 \cdot 10^{-2}$	$7.9 \cdot 10^{-3}$	$2.0 \cdot 10^{-3}$
10	10 / 0.25	$4.1 \cdot 10^{-2}$	$7.8 \cdot 10^{-3}$	$2.1 \cdot 10^{-2}$
100	100 / 0.33	$2.0 \cdot 10^{-1}$	$1.0 \cdot 10^{-2}$	$1.4 \cdot 10^{-1}$
150	150 / 0.38	$3.2 \cdot 10^{-1}$	$1.9 \cdot 10^{-2}$	$2.3 \cdot 10^{-1}$

Table 11: Relative error between uNSp and sNSp in the regularized Casson fluid case (B $= 0.1,\ \delta = 0.1,\ \varepsilon = 0.01,\ p_{in} = 1,\ p_{out} = 0$): *Profile 2*.

Re	T_f/ dt	u-relative error	v-relative error	p-relative error
0.1	1 / 0.02	$5.4 \cdot 10^{-2}$	$6.6 \cdot 10^{-3}$	$3.4 \cdot 10^{-3}$
1	1 / 0.03	$201 \cdot 10^{-2}$	$6.3 \cdot 10^{-3}$	$3.9 \cdot 10^{-3}$
10	10 / 0.03	$3.8 \cdot 10^{-2}$	$6.8 \cdot 10^{-3}$	$8.4 \cdot 10^{-3}$
100	100 / 0.5	$2.1 \cdot 10^{-1}$	$1.4 \cdot 10^{-2}$	$8.6 \cdot 10^{-2}$
150	150 / 0.5	$3.1 \cdot 10^{-1}$	$3.0 \cdot 10^{-2}$	$1.1 \cdot 10^{-1}$

Table 12: Relative error between uNSp and sNSp in the regularized Casson fluid case (B $= 0.1,\ \delta = 0.1,\ \varepsilon = 0.01,\ p_{in} = 1,\ p_{out} = 0$): *Profile 3*.

It can be observed that, except for the case of $Re = 100$ and *profile 1*, the average error is at most around 1%. Moreover, to limit the error (i.e., to converge to the steady-state solution), it is necessary to increase the final time T_f as Re increases.

Following this, graphs will be presented showing the temporal evolution for the components u, v, and p. For the sake of simplicity and graphical clarity, only an intermediate stage prior to the steady-state convergent solution will be considered, as well as the initial state (except for the transversal velocity component v). Furthermore, only the first two profiles will be analyzed, as the third is similar to the second.

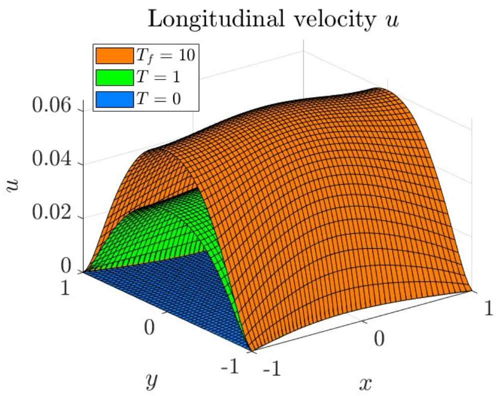

Figure 29: Temporal evolution of longitudinal velocity u.
Profile 1: $B = 0.1$, $p_{in} = 1$, $p_{out} = 0$, $\delta = 0.1$, $\varepsilon = 0.01$, $Re = 10$ (regularized Bingham).

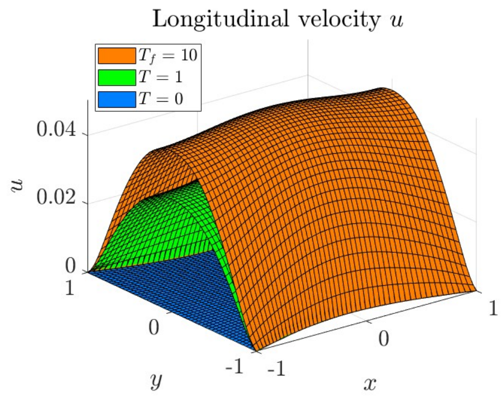

Figure 30: Temporal evolution of longitudinal velocity u.
Profile 1: $B = 0.1$, $p_{in} = 1$, $p_{out} = 0$, $\delta = 0.1$, $\varepsilon = 0.01$, $Re = 10$ (regularized Casson).

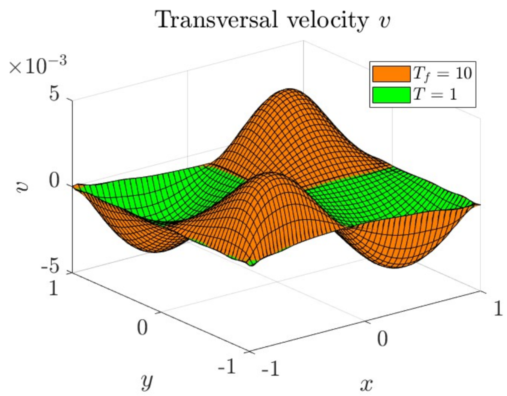

Figure 31: Temporal evolution of transversal velocity v.
Profile 1: $B = 0.1$, $p_{in} = 1$, $p_{out} = 0$, $\delta = 0.1$, $\varepsilon = 0.01$, $Re = 10$ (regularized Bingham).

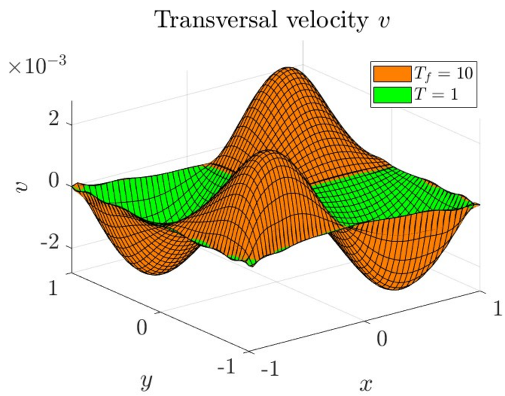

Figure 32: Temporal evolution of transversal velocity v.
Profile 1: $B = 0.1$, $p_{in} = 1$, $p_{out} = 0$, $\delta = 0.1$, $\varepsilon = 0.01$, $Re = 10$ (regularized Casson).

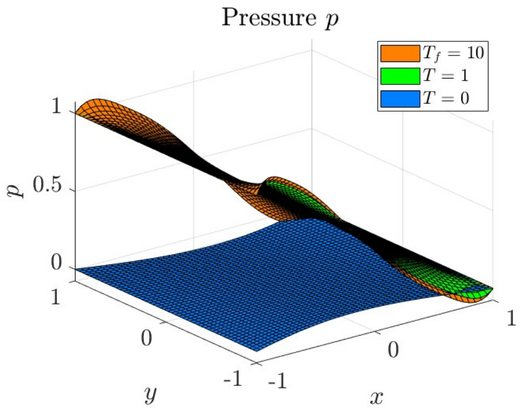

Figure 33: Temporal evolution of pressure p.
Profile 1: $B = 0.1$, $p_{in} = 1$, $p_{out} = 0$, $\delta = 0.1$, $\varepsilon = 0.01$, $Re = 10$ (regularized Bingham).

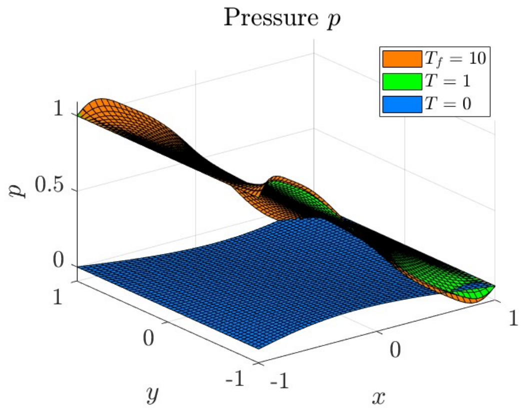

Figure 34: Temporal evolution of pressure p.
Profile 1: $B = 0.1$, $p_{in} = 1$, $p_{out} = 0$, $\delta = 0.1$, $\varepsilon = 0.01$, $Re = 10$ (regularized Casson).

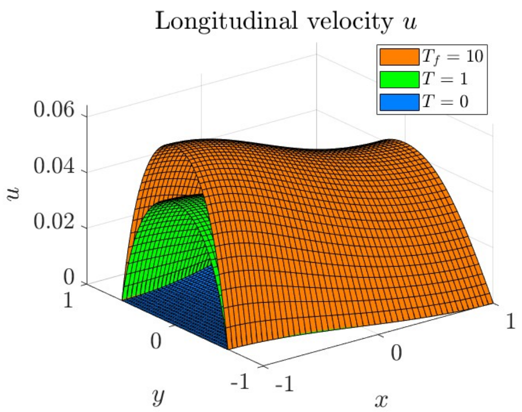

Figure 35: Temporal evolution of longitudinal velocity u.
Profile 2: $B = 0.1$, $p_{in} = 1$, $p_{out} = 0$, $\delta = 0.1$, $\varepsilon = 0.01$, $Re = 10$ (regularized Bingham).

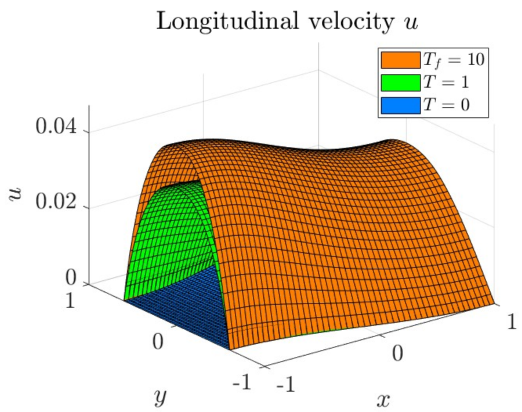

Figure 36: Temporal evolution of longitudinal velocity u.
Profile 2: $B = 0.1$, $p_{in} = 1$, $p_{out} = 0$, $\delta = 0.1$, $\varepsilon = 0.01$, $Re = 10$ (regularized Casson).

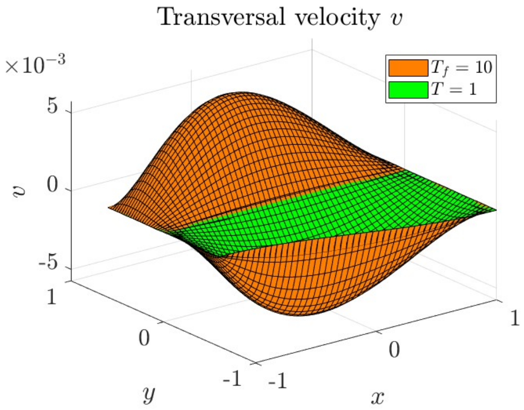

Figure 37: Temporal evolution of transversal velocity v.
Profile 2: $B = 0.1$, $p_{in} = 1$, $p_{out} = 0$, $\delta = 0.1$, $\varepsilon = 0.01$, $Re = 10$ (regularized Bingham).

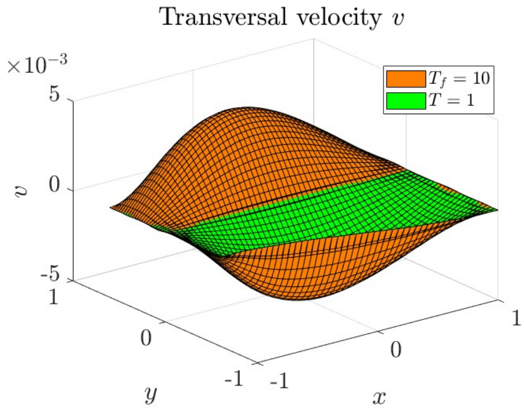

Figure 38: Temporal evolution of transversal velocity v.
Profile 2: $B = 0.1$, $p_{in} = 1$, $p_{out} = 0$, $\delta = 0.1$, $\varepsilon = 0.01$, $Re = 10$ (regularized Casson).

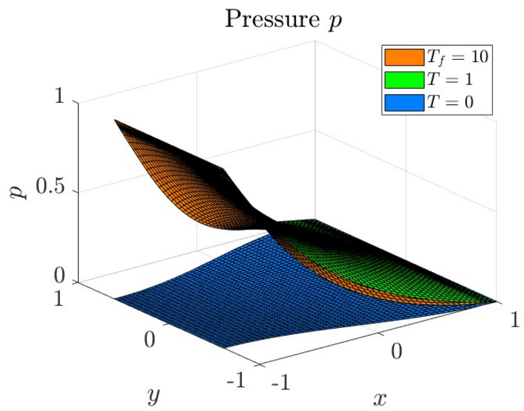

Figure 39: Temporal evolution of pressure p.
Profile 2: $B = 0.1$, $p_{in} = 1$, $p_{out} = 0$, $\delta = 0.1$, $\varepsilon = 0.01$, $Re = 10$ (regularized Bingham).

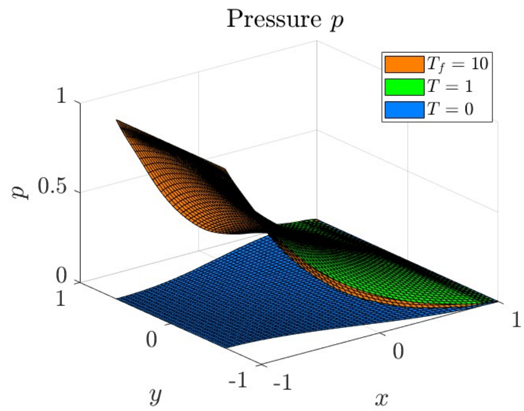

Figure 40: Temporal evolution of pressure p.
Profile 2: $B = 0.1$, $p_{in} = 1$, $p_{out} = 0$, $\delta = 0.1$, $\varepsilon = 0.01$, $Re = 10$ (regularized Casson).

For greater clarity, it is noted that the plot of the initial condition ($v = 0$) has not been included in the graphs of transverse velocity. It can be observed that there are no substantial differences between the Bingham and Casson models. Furthermore, the pressure regime close to the steady-state case is reached almost immediately (for instance, at $T = 0.1$, there are no significant differences compared to $T = 1$).

3 A spectral collocation scheme for the flow of a piezo-viscous fluid in ducts with slip conditions

This chapter is essentially an extension of the article [FG24a]. In particular, the final section will address both the stationary and non-stationary cases of the generalized Navier-Stokes problem for piezo-viscous fluids.
Since the seminal work of Bridgman [Bri31] on the physics of high pressure, the interest in fluids with pressure dependent viscosity has constantly grown within the scientific community. Fluids with pressure dependent rheology are ubiquitous in many practical applications, such as geological, environmental, industrial and biological flows. It is well known that the application of high pressure on liquids produces important changes in properties such as compressibility, viscosity, thermal conductivity, etc. The idea that the viscosity of a fluid can depend on pressure was first proposed by Stokes [Sto80]. Subsequently Barus [Bar93] provided an analytical form of the type

$$\mu^* = \mu_o^* \exp(\beta^*(T^*)p^*), \tag{103}$$

where μ_o^* is a reference viscosity and β^* is a coefficient depending on the absolute temperature T^*. Another formal expression for the viscosity is the one proposed by Andrade [And52], namely

$$\mu^* = Q^* \sqrt{\rho^*} \exp\left[\left(A^* + {\rho^*}^2 B^*\right) \frac{C^*}{T^*}\right], \tag{104}$$

where ρ^* is the density and Q^*, A^*, B^*, C^* are constants. Although the increase of the pressure produces an increase of the density, there are cases in which a variation of the pressure does not alter significantly the density but modifies in a dramatic fashion the viscosity, see [Den08], [Raj06], [Ren03]. In these cases we speak of incompressible fluids with pressure dependent viscosity, i.e. of incompressible fluid whose rheology may change with the pressure. Over the past 70 years a remarkable body of experimental evidence has proved the viscosity can depend on the pressure (and temperature), especially when the pressures involved are quite high, see [JT77], [JG80], [VdG98], [SIC17]. Here we are not interested in a precise form of the function relating the viscosity to the pressure, since we do not deal with a specific application. It is thus unnecessary to go through a detailed discussion of the experimental studies cited here. It is sufficient to pick up a regular function such as the one proposed by Barus. In practice, we shall consider a Navier-Stokes fluid in which the viscosity depends exponentially on the pressure (piezo-viscous fluid). The flow of piezo-viscous fluids has been extensively studied in the last decades. From the mathematical point of view the dependence of the viscosity on the pressure brings a nonlinearity to the momentum equation that changes the nature of the pressure itself. Indeed, in this case the pressure cannot be eliminated from the system using Helmoltz decomposition and therefore cannot be considered as a Lagrange multiplier. One of the first contribution on existence and uniqueness of solutions for piezo-viscous flows is the one by Renardy [Ren86][12] for a viscosity function that is sublinear at infinity and whose derivatives are bounded in R. Gazzola et al. [G$^+$94], [Gaz97], [GS92] have proven well posedness results for both the stationary and non-stationary case. An exhaustive treatise on the mathematical properties of piezo-viscous systems is given in [MR07].

The analytical solutions for these flows have been determined in papers such as [HMR01], [KPG11], but only for simple geometries. These analytical solutions are indeed available only in a limited number of geometrical settings and only for the steady state flow, while for more complex situations we must rely on numerical simulations. Some papers have been devoted to the detection of numerical solution and among them we cite [ZYN15], [NR11], [HMNR03]. It must be said that these works are almost entirely performed in very regular domains (such as straight channels, straight cylindrical annuli and so forth) and, to our knowledge, none of them is based on spectral collocation methods.

This part of the thesis examines the isothermal flow of an incompressible piezo-viscous fluid in a (not necessarily symmetric) duct with Navier slip boundary conditions. The numerical scheme employed here is largely based on the one presented in [FG24a] and [FG24b] in which a similar problem was considered for a generalized Newtonian fluid. The mathematical problem consists of a set of nonlinear partial differential equations (stress based formulation) that are discretized and solved via Newton-Raphson algorithm. To validate our model the numerical and analytical solution are compared in the case of a duct with small aspect ratio. Indeed, in this case the analytical solution can be obtained expanding the main variables around the "small parameter" (aspect ratio) and solving the leading order problem. It will be observed that the comparison demonstrates excellent agreement.

We consider a non-symmetric two-dimensional channel where the flow is driven by a specified pressure gradient. Subsequently, the three-dimensional flow problem in a non-straight axisymmetric conduit is investigated. In both cases the wall boundary conditions are of Navier type, i.e. the wall velocity is proportional to the tangential shear stress.

The numerical solutions will provide the behavior of the velocity field, the pressure field and viscosity. These simulations are important to understand how the flow is affected by the physical parameters appearing in the model and in particular, the Navier slip coefficient and the pressure coefficient.

The constitutive equation of the fluid under examination is

$$\mathbf{T}^* = -p^*\mathbf{I} + \mathbf{S}^*, \qquad \mathbf{S}^* = 2\mu^*(p^*)\mathbf{D}^*, \tag{105}$$

where $\mu^*(p^*)$ is a positive smooth function of the pressure p^*. In (105) $\mathbf{T}^*$ is the Cauchy stress tensor, $\mathbf{S}^*$ is the traceless part of the stress and $\mathbf{D}^*$ is the symmetric part of the velocity gradient $\mathbf{L}^* = \nabla\mathbf{v}^*$, $\mathbf{v}^* = (u^*, v^*)$ being the velocity field. For simplicity we assume that the viscosity function is given by the exponential law

$$\mu^*(p^*) = \mu_o^* \exp\Big[\beta^*(p^* - p_{out}^*)\Big], \tag{106}$$

where μ_o^* is the viscosity at pressure p_{out}^*, and β^* is a coefficient dimensionally represented as the inverse of a pressure. It should be noted that the study is not aimed at any specific application, hence, in principle, the exponential formula (106) could be substituted by any smooth positive function of the pressure. Impenetrability and slip conditions on the solid walls are imposed as follows:

$$\mathbf{v}^* \cdot \mathbf{n} = 0, \qquad \Big[\alpha^*\big(\mathbf{T}^*\mathbf{n}\big) + \mathbf{v}^*\Big] \cdot \mathbf{t} = 0, \tag{107}$$

where α^* is a constant parameter with dimensions $length^2 \cdot time/mass$ (dimensional slip parameter) and where $\mathbf{n}$, $\mathbf{t}$ are the inward normal and tangent unit vectors to the solid walls respectively. It should be noted that when $\alpha^* = 0$, the classical no-slip condition at the solid wall is recovered. In the absence of body forces, the governing equations are

$$\begin{cases} \rho^* \dot{\mathbf{v}}^* = -\nabla p^* + \nabla \cdot \mathbf{S}^*, \\ \\ \nabla \cdot \mathbf{v}^* = 0, \end{cases} \tag{108}$$

where the first represents the balance of linear momentum and the second represents mass conservation.

3.1 The mathematical model: two dimensional non-symmetric channel

This section examines the flow of a piezo-viscous fluid in a non-symmetric two-dimensional channel Ω^* bounded by the edges $x^* = \pm L^*$ and by solid walls described by $y^* = h^*(x^*)$ and $y^* = \sigma^*(x^*)$, as depicted in Fig. 41.

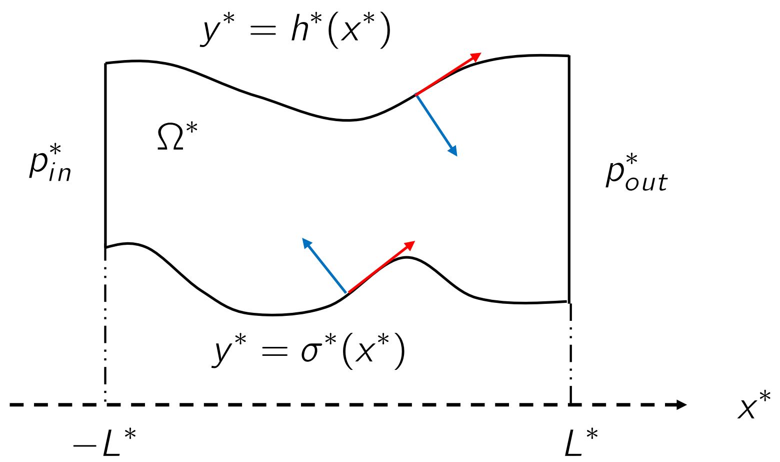

Figure 41: Sketch of the domain of the problem. Two dimensional non symmetric channel of non uniform width.

The flow is driven by a constant pressure drop $\Delta p^* = p^*_{in} - p^*_{out} > 0$, where p^*_{in}, p^*_{out} are the imposed pressures at $x^* = \pm L^*$. The lateral boundary conditions are

$p^* = p^*_{in}$, $v^* = 0$ at $x^* = -L^*$ and $p^* = p^*_{out}$, $v^* = 0$ at $x^* = L^*$. We define

$$H^* = \max_{x^* \in [-L^*, L^*]} \left[\frac{h^*(x^*) - \sigma^*(x^*)}{2} \right], \qquad \delta = \frac{H^*}{L^*}, \tag{109}$$

where H^* represents the maximum half width of the channel and δ is the aspect ratio of the channel. The variables are rescaled as follows:

$$x^* = L^* x, \quad y^* = H^* y, \qquad t^* = \left(\frac{L^*}{U^*} \right) t, \qquad u^* = U^* u, \tag{110}$$

$$v^* = \delta U^* v, \qquad \mu^* = \mu^*_o \mu(p), \qquad p^* - p^*_{out} = \left(\frac{\mu^*_o U^*}{\delta H^*} \right) p, \tag{111}$$

$$\mathbf{S}^* = \left(\frac{\mu^*_o U^*}{H^*} \right) \mathbf{S}, \qquad \mathbf{D}^* = \left(\frac{U^*}{H^*} \right) \mathbf{D}, \qquad \beta^* = \left(\frac{\delta H^*}{\mu^*_o U^*} \right) \beta, \tag{112}$$

where U^* is a characteristic velocity and $\mu(p) = \exp(\beta p)$ is the non dimensional apparent viscosity. The scaled components of the strain-rate tensor $\mathbf{D}$ and of the stress tensor $\mathbf{S}$ are

$$D_{11} = \delta u_x, \qquad D_{12} = \frac{1}{2}\big(u_y + \delta^2 v_x\big), \qquad D_{22} = \delta v_y, \tag{113}$$

$$S_{11} = 2\delta e^{\beta p} u_x, \qquad S_{12} = e^{\beta p}\big(u_y + \delta^2 v_x\big), \qquad S_{22} = 2\delta e^{\beta p} v_y, \tag{114}$$

respectively. The non dimensional governing equations are:

$$\begin{cases} \delta Re \dot{u} = -p_x + \delta (S_{11})_x + (S_{12})_y, \\ \\ \delta^3 Re \dot{u} = -p_y + \delta^2 (S_{12})_x + \delta (S_{22})_y, \\ \\ u_x + v_y = 0, \end{cases} \tag{115}$$

where $Re = (\rho^* U^* H^*)/\mu^*_o$ is the Reynolds number. The lateral boundary conditions are

$$p = p_{in}, \quad v = 0, \quad \text{on} \;\; x = -1, \qquad p = 0, \quad v = 0, \quad \text{on} \;\; x = 1. \tag{116}$$

where $p_{in} = (\delta \Delta p^* H^*)/(\mu^*_o U^*) > 0$. The impenetrability and slip conditions on

$y = h(x)$ become

$$\begin{cases} \alpha\Big[\delta h_x\big(S_{11}-S_{22}\big) - S_{12}\big(1-\delta^2 h_x^2\big)\Big] + u\big(1+\delta^2 h_x^2\big)^{\frac{3}{2}} = 0, \\ \\ u h_x - v = 0, \end{cases} \tag{117}$$

while, on $y = \sigma(x)$ we get

$$\begin{cases} \alpha\Big[-\delta\sigma_x\big(S_{11}-S_{22}\big) + S_{12}\big(1-\delta^2 \sigma_x^2\big)\Big] + u\big(1+\delta^2 \sigma_x^2\big)^{\frac{3}{2}} = 0, \\ \\ -u\sigma_x + v = 0, \end{cases} \tag{118}$$

where $\alpha = (\alpha^* \mu_o^*/H^*)$. The well posedness of problem (115)-(118) is discussed thoroughly in [MR07]. Under the assumption of creeping flow, where $Re \ll 1$, the system (115) simplifies to:

$$\begin{cases} 0 = -p_x + \delta(S_{11})_x + (S_{12})_y, \\ \\ 0 = -p_y + \delta^2(S_{12})_x + \delta(S_{22})_y, \\ \\ u_x + v_y = 0, \end{cases} \tag{119}$$

with boundary conditions (116), (117), (118). From $(117)_2$, $(118)_2$ we notice that whenever $h_x = 0$ or $\sigma_x = 0$ the transversal velocity $v = 0$ on the solid wall. We also notice that, since $v(\pm 1, y) \equiv 0$ on the inlet/oulet, the impenetrability conditions at the four corners $(\pm 1, h(\pm 1))$, $(\pm 1, \sigma(\pm 1))$ imply that

$$u(\pm 1, h(\pm 1))h_x(\pm 1) = v(\pm 1, h(\pm 1)) = 0, \tag{120}$$

$$u(\pm 1, \sigma(\pm 1))\sigma_x(\pm 1) = v(\pm 1, \sigma(\pm 1)) = 0. \tag{121}$$

In general $u \neq 0$ on the solid walls, so we conclude that, in order to have $(117)_2$, $(118)_2$ satisfied up to the four corners of the channel, the wall profiles must be such that $h_x(\pm 1) = \sigma_x(\pm 1) = 0$. In what follows we shall consider solid walls that satisfy this hypothesis.

3.1.1 Analytical solution in the case of small aspect ratio

When $\delta \ll 1$ we may look for a solution written as a power series in δ and focus on the leading order solution, i.e. the solution of the problem

$$\begin{cases} 0 = -p_x + (S_{12})_y, \qquad\qquad S_{12} = u_y e^{\beta p}, \\ \\ 0 = -p_y, \\ \\ u_x + v_y = 0. \end{cases} \tag{122}$$

Integrating the momentum equation we find $S_{12} = p_x y + c(x)$, with $c(x)$ unknown. The boundary conditions on the solid walls become

$$\begin{cases} u = \alpha e^{\beta p} u_y, \\ \\ v = u h_x, \end{cases} \quad \text{on} \quad y = h(x), \quad \begin{cases} u = -\alpha e^{\beta p} u_y, \\ \\ v = u \sigma_x, \end{cases} \quad \text{on} \quad y = \sigma(x). \tag{123}$$

The problem is thus symmetric with respect to the curve $y = (h + \sigma)/2$ and $S_{12} = 0$ on such a curve. As a consequence,

$$c(x) = -\frac{p_x}{2}(h + \sigma), \qquad \rightarrow \qquad u_y = e^{-\beta p} p_x \left[y - \frac{h + \sigma}{2} \right]. \tag{124}$$

The imposition of the boundary conditions on $y = h$ and $y = \sigma$ leads to

$$u\Big|_h = \frac{\alpha p_x}{2}(h - \sigma), \qquad u\Big|_\sigma = \frac{\alpha p_x}{2}(h - \sigma). \tag{125}$$

If we integrate u_y between y and h we find

$$u(x, y) = \frac{\alpha p_x}{2}(h - \sigma) - \frac{p_x e^{-\beta p}}{2}(h - y)(y - \sigma), \tag{126}$$

i.e. the longitudinal component of the velocity at the leading order. Notice that at this stage the pressure is unknown. From the continuity equation we have

$$v\Big|_\sigma - v\Big|_h = u\Big|_\sigma \sigma_x - u\Big|_h h_x = \int_\sigma^h -v_y dy = \int_\sigma^h u_x dy. \tag{127}$$

Next, equation (126) is differentiated with respect to x and substituted into the final integral of (127). Inserting (125) into (127) and integrating we find

$$\frac{d}{dx}\Big\{p_x\big[6\alpha(h-\sigma)^2 - e^{-\beta p}(h-\sigma)^3\big]\Big\} = 0, \tag{128}$$

which is a second order differential equation for the pressure p. Equation (128) plus the boundary conditions $p(-1) = p_{in}$, $p(1) = 0$ provides the BVP for the pressure, namely

$$\begin{cases} p_{xx} = -p_x \dfrac{\big[6\alpha(h-\sigma)^2 - e^{-\beta p}(h-\sigma)^3\big]_x}{\big[6\alpha(h-\sigma)^2 - e^{-\beta p}(h-\sigma)^3\big]}, \\ \\ p(-1) = p_{in}, \qquad p(1) = 0. \end{cases} \tag{129}$$

Once (129) is solved, and this can be done only numerically, the pressure gradient p_x can be substituted in (126) providing the longitudinal velocity u. The transversal component v of the velocity is then obtained from

$$v\Big|_y - v\Big|_h = \int_y^h -v_y dy = \int_y^h u_x dy. \tag{130}$$

After some calculations we find

$$v(x,y) = \frac{\partial}{\partial x}\left[\frac{\alpha p_x}{2}(h-\sigma)(h-y) + \frac{p_x e^{-\beta p}}{12}(h-y)^2(3\sigma - 2y - h)\right]. \tag{131}$$

From (128) we see that

$$p_x\big[6\alpha(h-\sigma)^2 - e^{-\beta p}(h-\sigma)^3\big] = const. \tag{132}$$

Hence, when $\alpha = 0$ we find

$$-p_x e^{-\beta p} = \frac{const}{(h-\sigma)^3}, \qquad v(x,y) = -\frac{\partial}{\partial x}\left[\frac{(h-y)^2(3\sigma-2y-h)}{12(h-\sigma)^3}\right], \tag{133}$$

implying

$$v(x,y) = \frac{\partial}{\partial x}\Big[\mathcal{F}(h,\sigma,y)\Big] = \mathcal{F}_h h_x + \mathcal{F}_\sigma \sigma_x. \tag{134}$$

Hence, if there exists some $\bar{x}$ such that $h_x = \sigma_x = 0$, then $v(\bar{x}, y) \equiv 0$. On the other hand, when $\beta = 0$ (Newtonian fluid)

$$p_x\Big[6\alpha(h-\sigma)^2 - (h-\sigma)^3\Big] = const, \qquad \rightarrow \qquad p_x = \mathcal{G}(h,\sigma), \tag{135}$$

and

$$v(x,y) = \frac{\partial}{\partial x}\left[\frac{\alpha p_x}{2}(h-\sigma)(h-y) + \frac{p_x}{12}(h-y)^2(3\sigma - 2y - h)\right]. \tag{136}$$

Therefore, once again, we find

$$v(x,y) = \frac{\partial}{\partial x}\Big[\mathcal{H}(h,\sigma,y)\Big] = \mathcal{H}_h h_x + \mathcal{H}_\sigma \sigma_x, \tag{137}$$

and $v \equiv 0$ at each $\bar{x}$ such that $h_x = \sigma_x = 0$.

3.1.2 The numerical scheme

In this section we solve problem (119) numerically using a spectral collocation scheme. As a first step we must transform the physical domain Ω in the computational domain $[-1,1]^2$. To this aim we consider the mappings

$$\begin{cases} \xi = x, \\ \eta = \dfrac{2y-(h+\sigma)}{(h-\sigma)}, \end{cases} \qquad\qquad \begin{cases} x = \xi, \\ y = \dfrac{1}{2}\Big[(h+\sigma) + \eta(h-\sigma)\Big]. \end{cases} \tag{138}$$

The coordinates $(\xi,\eta) \in [-1,1]^2$ are the computational coordinates. For any given function ϕ, we denote with $\hat{\phi}$ the function with respect to the variables (ξ,η), i.e. $\phi(x,y) = \hat{\phi}(\xi,\eta)$. It is easy to express the spatial derivatives with respect to the new variables

$$P_1 := \frac{\partial}{\partial x} = \frac{\partial}{\partial \xi} - \left[\frac{\eta(\hat{h}_\xi - \hat{\sigma}_\xi) + (\hat{h}_\xi + \hat{\sigma}_\xi)}{(\hat{h}-\hat{\sigma})}\right]\frac{\partial}{\partial \eta}, \tag{139}$$

$$P_2 := \frac{\partial}{\partial y} = \frac{2}{(\hat{h}-\hat{\sigma})}\frac{\partial}{\partial \eta}. \tag{140}$$

The problem (119) can be reformulated in the new coordinate system (ξ,η) for the vector function $\hat{\mathbf{X}} = (\hat{S}_{11}, \hat{S}_{12}, \hat{S}_{22}, \hat{u}, \hat{v}, \hat{p})^T$.

$$
\begin{bmatrix}
\delta P_1 & P_2 & 0 & 0 & 0 & -P_1 \\
0 & \delta^2 P_1 & \delta P_2 & 0 & 0 & -P_2 \\
1 & 0 & 0 & -2\delta e^{\beta\hat{p}} P_1 & 0 & 0 \\
0 & 1 & 0 & -e^{\beta\hat{p}} P_2 & -\delta^2 e^{\beta\hat{p}} P_1 & 0 \\
0 & 0 & 1 & 0 & -2\delta e^{\beta\hat{p}} P_2 & 0 \\
0 & 0 & 0 & P_1 & P_2 & 0
\end{bmatrix}
\begin{bmatrix}
\widehat{S}_{11} \\ \widehat{S}_{12} \\ \widehat{S}_{22} \\ \widehat{u} \\ \widehat{v} \\ \widehat{p}
\end{bmatrix}
= 0, \qquad (141)
$$

to which we must add the boundary conditions

$$
\begin{bmatrix}
\delta\alpha\hat{h}_\xi & -\alpha(1-\delta^2\hat{h}_\xi^2) & -\delta\alpha\hat{h}_\xi & (1+\delta^2\hat{h}_\xi^2)^{(3/2)} & 0 & 0 \\
0 & 0 & 0 & \hat{h}_\xi & -1 & 0
\end{bmatrix}
\hat{\mathbf{X}} = 0, \qquad \text{on} \quad \eta = 1, \qquad (142)
$$

$$
\begin{bmatrix}
-\delta\alpha\hat{\sigma}_\xi & \alpha(1-\delta^2\hat{\sigma}_\xi^2) & -\delta\alpha\hat{\sigma}_\xi & (1+\delta^2\hat{\sigma}_\xi^2)^{(3/2)} & 0 & 0 \\
0 & 0 & 0 & -\hat{\sigma}_\xi & 1 & 0
\end{bmatrix}
\hat{\mathbf{X}} = 0, \qquad \text{on} \quad \eta = -1, \qquad (143)
$$

and

$$
\hat{p} = p_{in}, \quad \hat{v} = 0 \quad \text{on} \quad \xi = -1, \qquad \hat{p} = \hat{v} = 0 \quad \text{on} \quad \xi = 1. \qquad (144)
$$

Problem (141) with BCs (142)-(144) is discretized as in [FG24a] and [FG24b] producing an overdetermined non-square nonlinear system

$$
\mathbf{F}(\hat{\mathbf{X}}) = \mathbf{0}, \qquad (145)
$$

that is solved via Newton-Raphson algorithm

$$
\left[\mathbf{J}(\hat{\mathbf{X}}^n)\right]\Delta\hat{\mathbf{X}}^n = -\mathbf{F}(\hat{\mathbf{X}}^n), \qquad \hat{\mathbf{X}}^{n+1} = \hat{\mathbf{X}}^n + \Delta\hat{\mathbf{X}}^n, \qquad (146)
$$

where $\mathbf{J}(\hat{\mathbf{X}}^n)$ is the Jacobian of $\mathbf{F}(\hat{\mathbf{X}})$ evaluated at iteration n. The matrix $\mathbf{J}(\hat{\mathbf{X}}^n)$ is not square and $\Delta\hat{\mathbf{X}}^n$ is a least-square solution of $(146)_1$.

3.1.3 Numerical results and discussion: non-symmetric channel

In this section, numerical simulations are conducted to investigate the behavior of the main physical variables of the problem. The number of Gauss-Lobatto points for the numerical grid is taken $N = 20$, as in [FG24b]. This number was selected because for $N > 20$, the variation of the sup norm of the solution is within the sixth decimal digit (attributable to the high accuracy of the spectral collocation method). Various general wall functions $h(x)$ and $\sigma(x)$ will be considered, along with different values of the parameters α, β, and δ. The analysis begins with the profiles:

$$h(x) = \frac{9}{10} + \frac{1}{10}\cos\left(\frac{\pi}{2}(x+1)\right), \quad \sigma(x) = \frac{3}{10} + \frac{2}{10}\cos\left(\frac{\pi}{2}(x+1)\right), \tag{147}$$

i.e. a non symmetric channel satisfying the compatibility conditions $h_x(\pm 1) = \sigma_x(\pm 1) = 0$. Initially, the numerical scheme is validated against the analytical solution established in Section 3.1.1, applicable under the condition that the aspect ratio of the channel δ is small. For this purpose, the sup norm is considered:

$$\epsilon(\delta) = \|(u_N, v_N, p_N) - (u, v, p)\|_\infty, \tag{148}$$

where (u_N, v_N, p_N) is the numerical solution and (u, v, p) is the analytical solution determined in Section 3.1.1. The function $\epsilon(\delta)$ defined in (148) clearly makes sense only for small values of δ. The values $\alpha = -1$ and $\beta = 1$ are chosen, although other values for these parameters could also be used. Table 13 displays the values of ϵ as δ decreases. As expected ϵ decrease for decreasing δ, showing the validity of our numerical scheme.

$\epsilon(\delta)$	δ
1.641076333340799	1
0.349446431546098	0.5
0.013604396600548	0.1
0.003368633037444	0.05
$5.450549014254116 \cdot 10^{-4}$	0.01
$3.444601416401797 \cdot 10^{-5}$	0.001

Table 13: Norm (148) representing the absolute error between the numerical and analytical solution. $N = 20$, $\alpha = -1$ and $\beta = 1$.

Let us now perform some numerical simulations to investigate the behavior of the numerical solution for different values of the physical parameters involved in the model and for various wall profiles. For these numerical simulations we take $\delta = 1$, i.e. a channel whose characteristic length is equal to the characteristic half width. In Figs. 42-45 we show the 3D plots of the velocity components, of the pressure and of the apparent viscosity for $\alpha = -1$, $\beta = 1$ and $\delta = 1$ and for the channel profile (147). On the $(x, y, 0)$ plane we have also plotted the wall profiles (dashed line). We observe that the longitudinal velocity is larger in the narrow part of the channel and that the apparent viscosity diminishes along the channel because of the decrease of the pressure. One can easily check that the boundary conditions at the inlet/outlet (116) and the compatibility conditions (120) and (121) are satisfied.

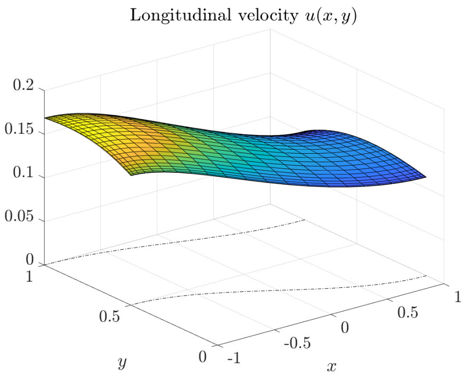

Figure 42: Wall profiles (147). Velocity $u(x, y)$, $\alpha = -1$, $\beta = 1$, $\delta = 1$.

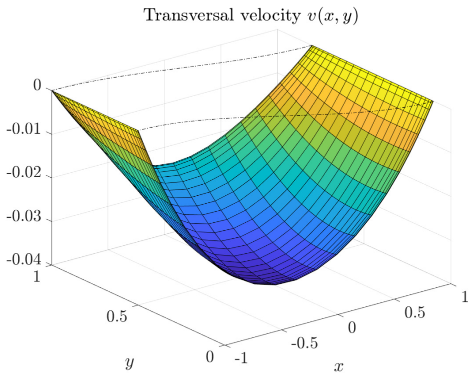

Figure 43: Wall profiles (147). Velocity $v(x, y)$, $\alpha = -1$, $\beta = 1$, $\delta = 1$.

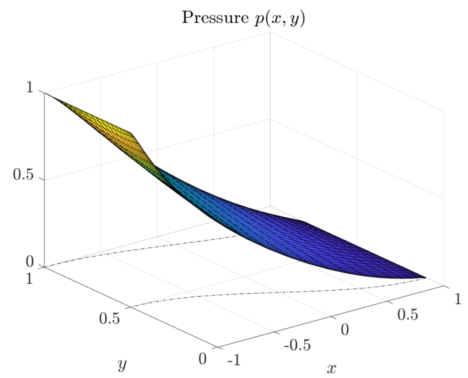

Figure 44: Wall profiles (147). Pressure $p(x, y)$, $\alpha = -1$, $\beta = 1$, $\delta = 1$.

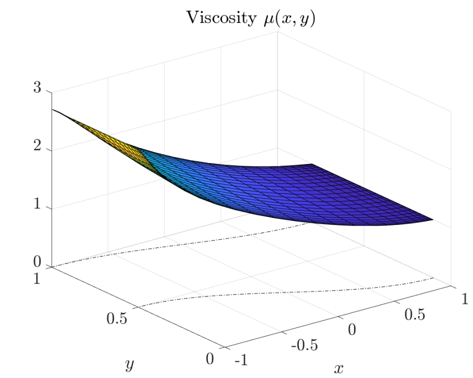

Figure 45: Wall profiles (147). Viscosity $\mu(x, y)$, $\alpha = -1$, $\beta = 1$, $\delta = 1$.

Let us now consider the wall profiles

$$h(x) = \frac{9}{10} + \frac{1}{10}\cos\left(\frac{\pi}{2}(x+1)\right), \quad \sigma(x) \equiv -0.3, \tag{149}$$

with $\alpha = -1$, $\beta = 1$ and $\delta = 1$. The 3D plots for u, v, p and μ are shown in Figs 46-49. Once again, we notice that the longitudinal velocity is larger in the narrow part of the channel, that is in the final section of the channel where the pressure is smaller. This result shows that the increase of the longitudinal velocity is not due to the increase of the pressure but only to the shrinking of the channel gap, since in the last part of the channel the pressure p is reduced whereas u increases. The apparent viscosity follows the behavior of the pressure, since μ is an increasing function of the pressure ($\beta > 0$). We also see that the transversal velocity $v \equiv 0$ on $y = \sigma$, since $\sigma_x \equiv 0$, see the boundary conditions $(118)_2$. Differently from the case in which the channel walls are given by (147), here the pressure and the apparent viscosity are not monotone in x in the proximity of the upper wall. This last result shows that the monotonicity of the pressure is strictly influenced by the geometry of the channel.

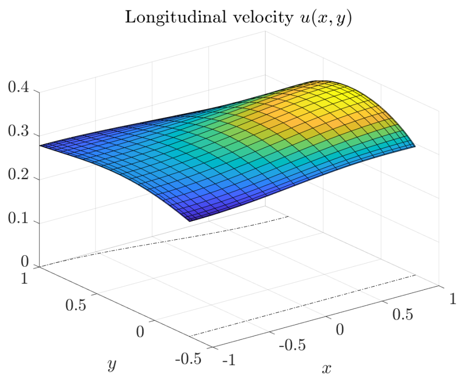

Figure 46: Wall profiles (149). Velocity $u(x,y)$, $\alpha = -1$, $\beta = 1$, $\delta = 1$.

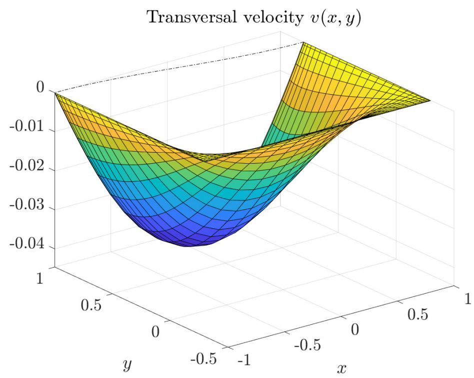

Figure 47: Wall profiles (149). Velocity $v(x,y)$, $\alpha = -1$, $\beta = 1$, $\delta = 1$.

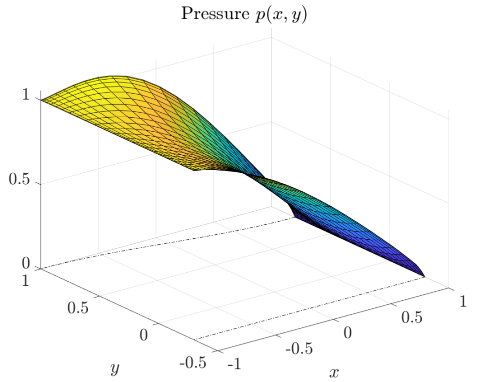

Figure 48: Wall profiles (149).Pressure $p(x, y)$, $\alpha = -1$, $\beta = 1$, $\delta = 1$.

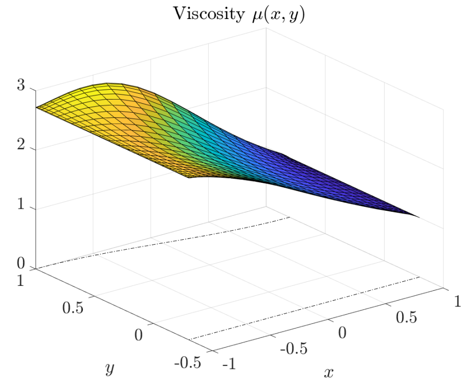

Figure 49: Wall profiles (149).Viscosity $\mu(x, y)$, $\alpha = -1$, $\beta = 1$, $\delta = 1$.

Let us now pass to investigate the effects of the parameters α and β on the solution of the problem. The analysis starts with a consideration of fixed α and varying β, representing a scenario of changing apparent viscosity. In Figs 50-53, the variables u, v, p, and μ are plotted for the wall functions (147) with $\alpha = -1$, $\delta = 1$ and $\beta = -1, 0, 1$. Looking at Figs 50, 51, we immediately observe that the velocity components u, v decrease (in modulus) with β. This is physically consistent, since a small value of β is characteristic of a "less viscous" fluid, i.e. a fluid that flows "more easily" and hence "more rapidly". The pressure distribution does not show significant variations for the three values of β considered, even though it seems to be a bit larger for smaller values of β (this behavior is inverted in the proximity of the channel corners, see Fig. 52). The apparent viscosity is strongly influenced by the parameter β and μ increases with β, as expected, see Fig. 53. From this plot it is evident how the deviation from the Newtonian model (corresponding to $\beta = 0$) alters the flow properties of the fluid. In particular, it is evident that, for fixed value of α and p_{in} and for a viscosity function which grows with pressure, the flow is slower than in the Newtonian case.

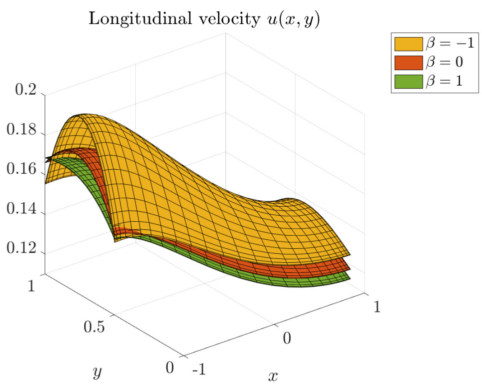

Figure 50: Wall profiles (147).Velocity $u(x,y)$, $\alpha=-1$, $\delta=1$, $\beta=-1,0,1$.

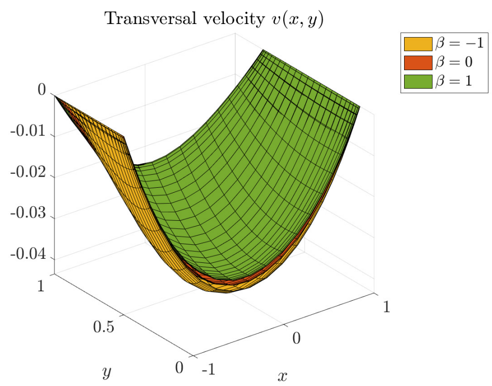

Figure 51: Wall profiles (147).Velocity $v(x,y)$, $\alpha=-1$, $\delta=1$, $\beta=-1,0,1$.

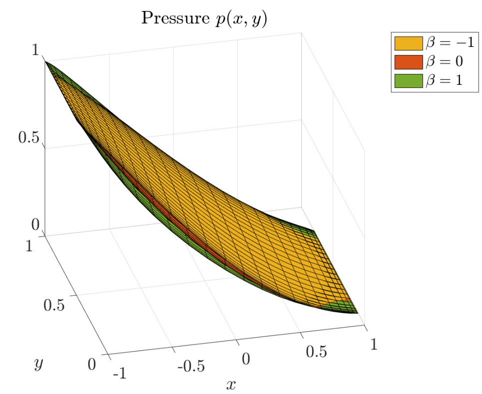

Figure 52: Wall profiles (147).Pressure $p(x,y)$, $\alpha=-1$, $\delta=1$, $\beta=-1,0,1$.

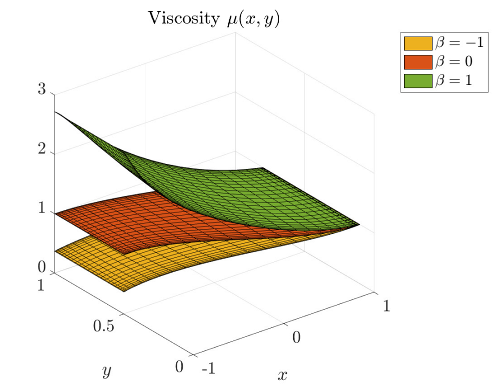

Figure 53: Wall profiles (147).Viscosity $\mu(x,y)$, $\alpha=-1$, $\delta=1$, $\beta=-1,0,1$.

Let us now consider the case in which β is kept fixed and α varies. This situation is representative of different types of channel walls, i.e. different slip conditions. In Figs 54-57 we plot the variables u, v, p, μ for wall profiles (147) with $\beta=1$, $\delta=1$ and $\alpha=-2,-1,0$. The increase (in modulus) of the slip parameter α induces an increase of the velocity components (in modulus). This is physically consistent, since the resistance exerted by the solid walls is reduced when $|\alpha|$ is increased and the fluid flows more easily. The pressure, and hence the viscosity, seems to be less affected by the value of α. Indeed, looking at Fig. 56, 57, we notice that the pressure and the apparent viscosity do not show significant changes for increasing $|\alpha|$ and that there are regions in which the three surfaces corresponding to the different values of α overlap.

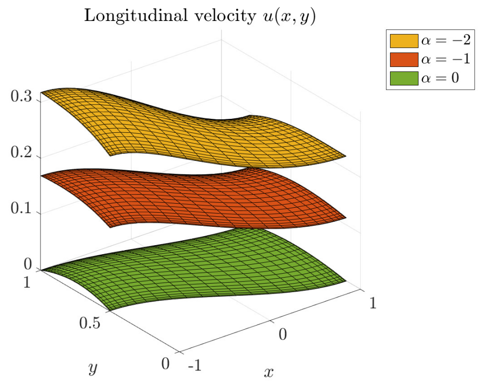

Figure 54: Wall profiles (147).Velocity $u(x,y)$, $\beta = 1$, $\delta = 1$, $\alpha = -2,-1,0$.

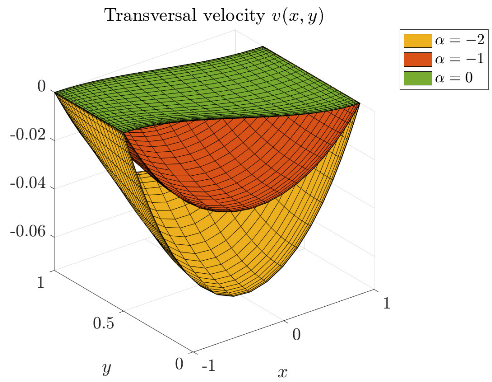

Figure 55: Wall profiles (147).Velocity $v(x,y)$, $\beta = 1$, $\delta = 1$, $\alpha = -2,-1,0$.

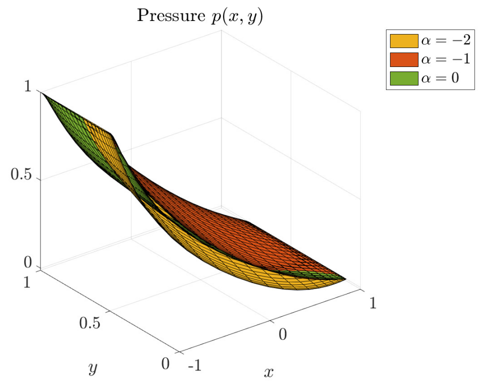

Figure 56: Wall profiles (147).Pressure $p(x,y)$, $\beta = 1$, $\delta = 1$, $\alpha = -2,-1,0$.

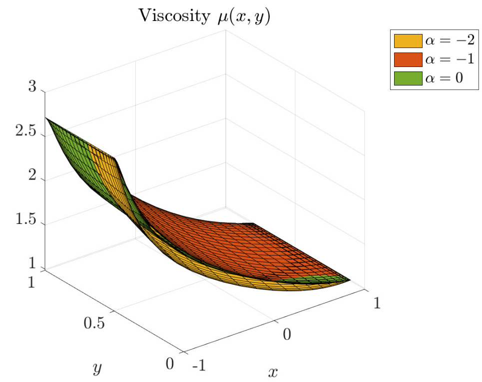

Figure 57: Wall profiles (147).Viscosity $\mu(x,y)$, $\beta = 1$, $\delta = 1$, $\alpha = -2,-1,0$.

3.2 Flow in an axisymmetric cylindrical channel with slip conditions

Let us consider the flow of a piezo-viscous fluid in a axisymmetric tube of non constant radius $r^* = h^*(z^*)$ and length $2L^*$, like the one depicted in Fig. 58.

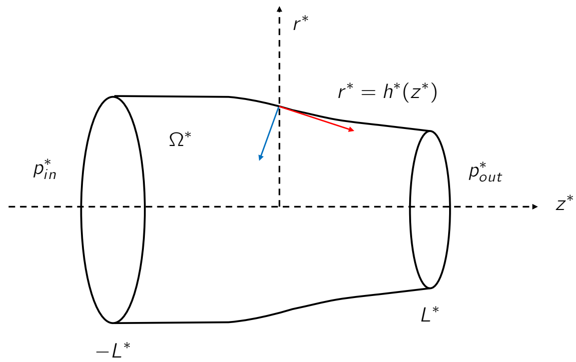

Figure 58: Sketch of the domain of the problem. Cylindrical axisymmetric channel of non constant radius $r^* = h^*(z^*)$.

Because of symmetry, the steady state velocity field in the cylindrical coordinates system (r^*, θ, z^*) acquires the form $\mathbf{v}^*(r^*, z^*) = v^*(r^*, z^*)\mathbf{e}_r + w^*(r^*, z^*)\mathbf{e}_z$. The only non zero components of the deviatoric stress $\mathbf{S}^*$ defined in (105) are

$$S^*_{rr} = 2\mu^* v^*_r, \quad S^*_{\theta\theta} = \frac{2\mu^* v^*}{r^*}, \quad S^*_{rz} = \mu^*(w^*_r + v^*_z), \quad S^*_{zz} = 2\mu^* w^*_z. \tag{150}$$

We define $R^* = \max h^*(z^*)$ and $\delta = R^*/L^*$. The variables r^*, z^*, v^* and w^* are scaled with R^*, L^*, U^*, δU^*, respectively. The pressure, stress and symmetric part of the velocity gradient are scaled as in (111), (112) (with H^* replaced by R^*). In the hypothesis of creeping flow, the system of non-dimensional governing equations is given by

$$\begin{cases} 0 = -rp_r + \delta r\left(S_{rr}\right)_r + \delta\left(S_{rr} - S_{\theta\theta}\right) + \delta^2 r\left(S_{rz}\right)_z, \\[2ex] 0 = -rp_z + S_{rz} + r\left(S_{rz}\right)_r + \delta r\left(S_{zz}\right)_z, \\[2ex] \left(rv\right)_r + rw_z = 0, \\[2ex] S_{rr} = 2\mu\delta v_r, \qquad S_{rz} = \mu\left(w_r + \delta^2 v_z\right), \\[2ex] S_{\theta\theta} = 2\mu v/r, \qquad S_{zz} = 2\mu\delta w_z. \end{cases} \tag{151}$$

The non dimensional boundary conditions are now given by

$$p = p_{in}, \quad v = 0, \quad \text{on} \quad z = -1, \qquad p = 0, \quad v = 0, \quad \text{on} \quad z = 1, \tag{152}$$

$$\begin{cases} \alpha\left[\delta h_z\left(S_{zz} - S_{rr}\right) - S_{rz}\left(1 - \delta^2 h_z^2\right)\right] + w\left(1 + \delta^2 h_z^2\right)^{\frac{3}{2}} = 0, \\[2ex] wh_z - v = 0, \end{cases} \tag{153}$$

on $r = h(z)$ and

$$w_r = 0, \qquad v = 0, \quad \text{on} \quad r = 0, \qquad \text{(symmetry)}. \tag{154}$$

Again, the well posedness of problem (151)-(154) is proven [MR07]. Proceeding as in Section 3.1.1, we can prove that the leading order solution of the lubrication flow $\delta \ll 1$ is given by (we skip all the calculation because they are very similar to those of section 3.1.1)

$$u(r,z) = \frac{\alpha p_z h}{2} + \frac{p_z e^{-\beta p}}{4}(r^2 - h^2), \tag{155}$$

$$v(r,z) = -\frac{\partial}{\partial z}\left[\frac{\alpha p_z h}{4} + \frac{p_z e^{-\beta p}}{16}(r^3 - 2h^2 r)\right], \tag{156}$$

where $p = p(z)$ is the solution of the second order BVP

$$\begin{cases} p_{zz} = -p_z \dfrac{\left[4\alpha h^3 - e^{-\beta p} h^4\right]_z}{\left[4\alpha h^3 - e^{-\beta p} h^4\right]}, \\ \\ p(-1) = p_{in}, \qquad p(1) = 0. \end{cases} \tag{157}$$

3.2.1 Numerical results and discussion: axisymmetric conduit

In this section we present the numerical simulations for the system (151), (152), (153) and (154) obtained, once again, with the use of a spectral collocation scheme analogous to the one of Section 3.1.2 (we skip all the details that are similar to those of the planar case). The number of Gauss-Lobatto points for the numerical grid is still $N = 20$. We consider the wall function

$$h(z) = \frac{9}{10} + \frac{1}{10}\cos\left(\frac{\pi}{2}(z+1)\right), \tag{158}$$

which satisfy the compatibility condition $h_z(\pm 1) = 0$. We validate our model, comparing the numerical solution with the analytical solution in the case $\delta < 1$. Recalling the definition of $\epsilon(\delta)$ given in (148) we obtain the sequence shown in Table 14, proving the validity of our numerical scheme.

$\epsilon(\delta)$	δ
3.624850411161941	1
0.865293190703391	0.5
0.034789099947078	0.1
0.009016829486871	0.05
0.002197874463444	0.01
$1.984851997393461 \cdot 10^{-4}$	0.001

Table 14: Norm (148) representing the absolute error between the numerical and analytical solution. $N = 20$, $\alpha = -1$ and $\beta = 1$.

In Figs. 59-62 we plot the velocity components, pressure and apparent viscosity for $\delta = 1$, $\alpha = -1$ and $\beta = 1$. We notice that the longitudinal component increases in the narrow part of the channel, as observed for the planar case. One can easily notice that the overall behavior of the solution is very similar to that of the planar case, as expected.

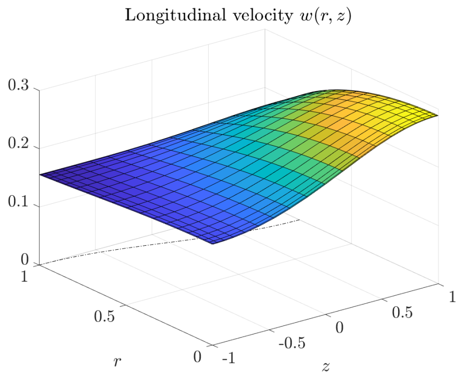

Figure 59: Wall profiles (158). Velocity $u(r,z)$, $\beta = 1$, $\delta = 1$, $\alpha = -1$.

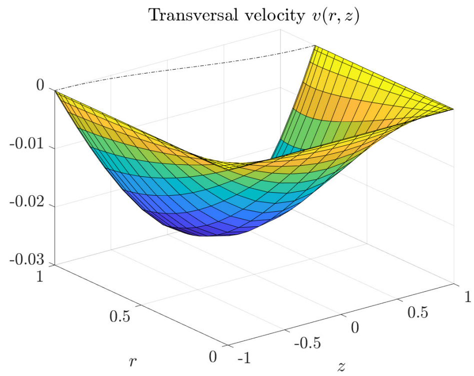

Figure 60: Wall profiles (158). Velocity $v(r,z)$, $\beta = 1$, $\delta = 1$, $\alpha = -1$.

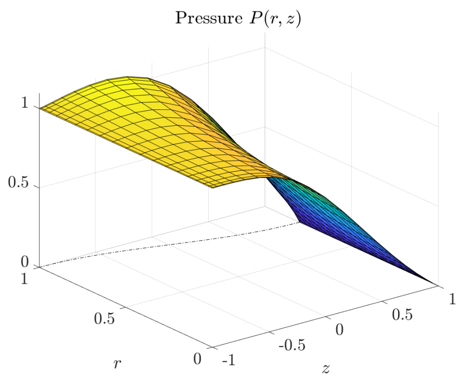

Figure 61: Wall profiles (158). Pressure $p(r,z)$, $\beta = 1$, $\delta = 1$, $\alpha = -1$.

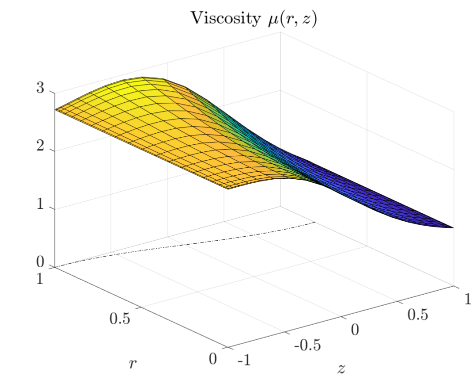

Figure 62: Wall profiles (158). Viscosity $\mu(r,z)$, $\beta = 1$, $\delta = 1$, $\alpha = -1$.

We then consider a wall function that is not monotone, namely

$$h(z) = 1 - \frac{1}{5}(z^2 - 1)^2. \tag{159}$$

The solution for the profile (159) with $\delta = 1$, $\alpha = -1$ and $\beta = 1$ is depicted in Figs. 63-66. Once again we notice how the pressure (and consequently the apparent viscosity) is influenced by the geometry of the channel.

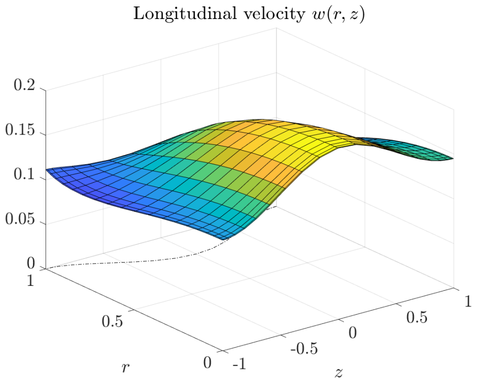

Figure 63: Wall profiles (159).Velocity $u(r,z)$, $\beta = 1$, $\delta = 1$, $\alpha = -1$.

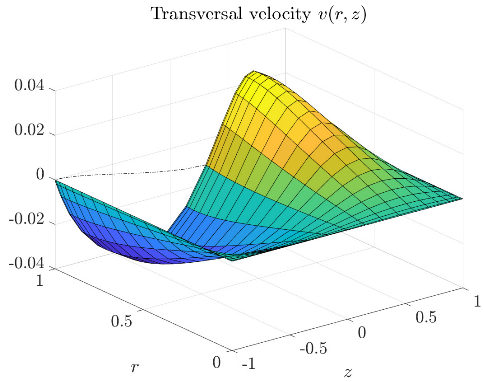

Figure 64: Wall profiles (159).Velocity $v(r,z)$, $\beta = 1$, $\delta = 1$, $\alpha = -1$.

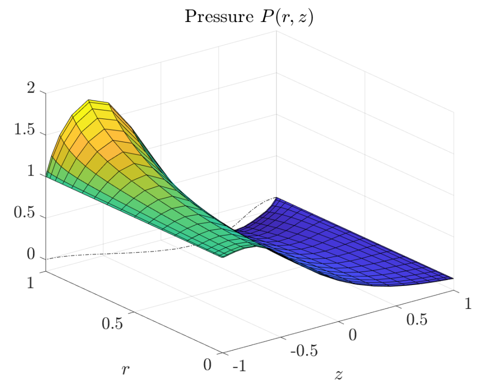

Figure 65: Wall profiles (159).Pressure $p(r,z)$, $\beta = 1$, $\delta = 1$, $\alpha = -1$.

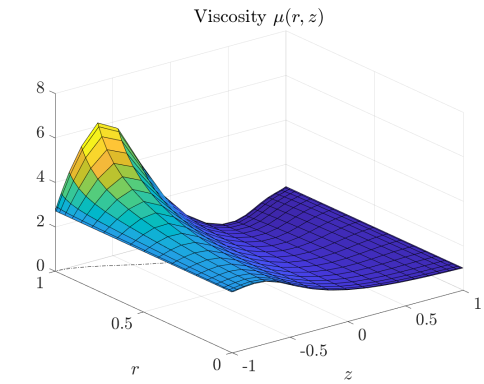

Figure 66: Wall profiles (159).Viscosity $\mu(r,z)$, $\alpha = -1$, $\delta = 1$, $\beta = -1, 0, 1$.

In Figs 67-70, the effects of the pressure coefficient β on the solution with wall function (159) are illustrated. We again observe that, as β increases the flow is slowed down because of the increase of viscosity (larger flow resistance). In Figs 71-74, the effects of the slip coefficient α on the solution with wall function (159) are depicted.

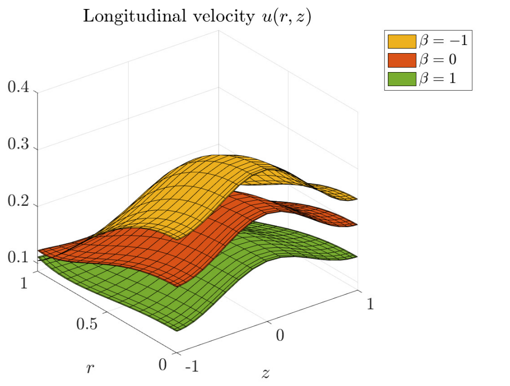

Figure 67: Wall profiles (159).Velocity $u(r,z)$, $\alpha = -1$, $\delta = 1$, $\beta = -1, 0, 1$.

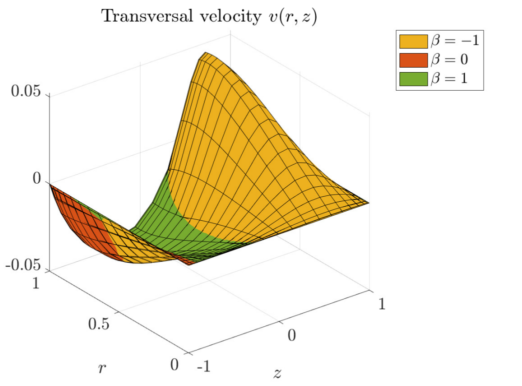

Figure 68: Wall profiles (159).Velocity $v(r,z)$, $\alpha = -1$, $\delta = 1$, $\beta = -1, 0, 1$.

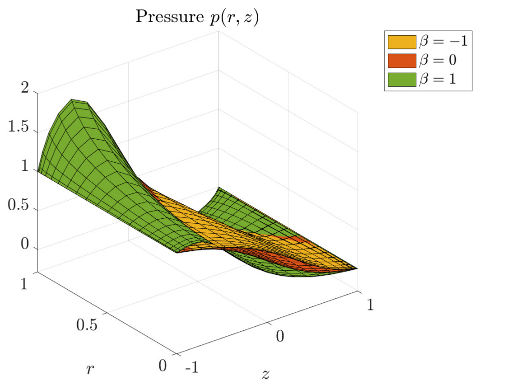

Figure 69: Wall profiles (159).Pressure $p(r,z)$, $\alpha = -1$, $\delta = 1$, $\beta = -1, 0, 1$.

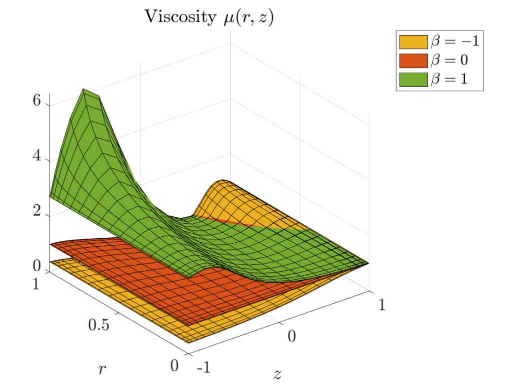

Figure 70: Wall profiles (159).Viscosity $\mu(r,z)$, $\alpha = -1$, $\delta = 1$, $\beta = -1, 0, 1$.

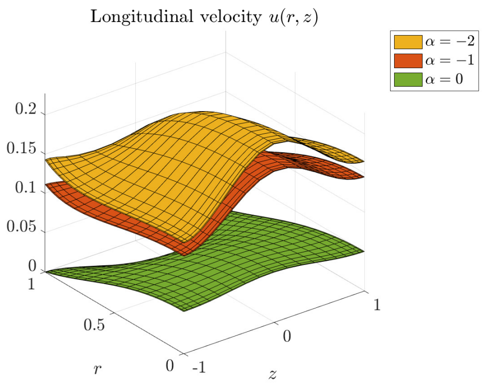

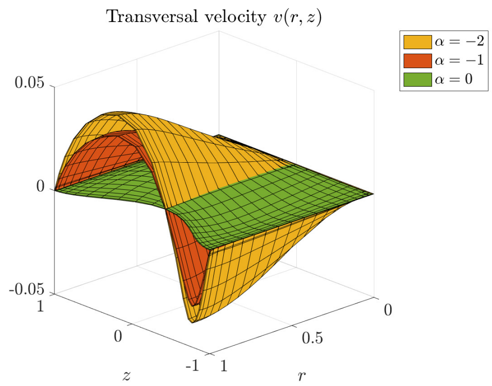

Figure 71: Wall profiles (159).Viscosity $\mu(r,z)$, $\beta = -1$, $\delta = 1$, $\alpha = -2, -1, 0$.

Figure 72: Wall profiles (159).Viscosity $\mu(r,z)$, $\beta = -1$, $\delta = 1$, $\alpha = -2, -1, 0$.

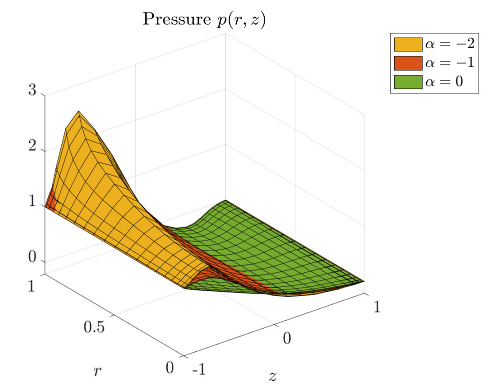

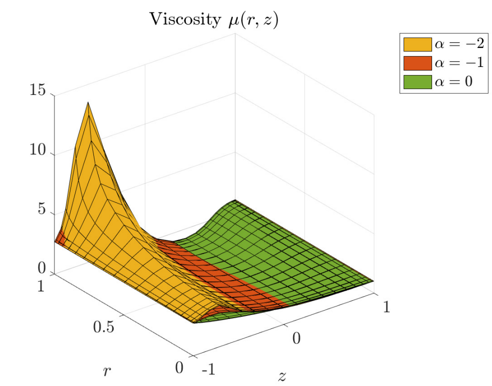

Figure 73: Wall profiles (159).Viscosity $\mu(r,z)$, $\beta = -1$, $\delta = 1$, $\alpha = -2, -1, 0$.

Figure 74: Wall profiles (159).Viscosity $\mu(r,z)$, $\beta = -1$, $\delta = 1$, $\alpha = -2, -1, 0$.

3.3 Extension of the results to the steady generalized Navier-Stokes case

In this section, the same approach as in Section 2.6 will be followed, both for the various profiles of the flow case in a non-symmetric channel and for the profiles of the case of an axisymmetric duct. In the *non-symmetric channel* configuration, we shall consider both the extension involving the nonlinear term $\nabla\mathbf{v}[\mathbf{v}]$, corresponding to the *steady case*, and the more intricate time-dependent formulation incorporating the term $\partial_t\mathbf{v} = \left(u_t,\ v_t\right)^T$. For this purpose, it is necessary to introduce additional terms into the *Jacobian matrix* to account for the nonlinear component of the Generalized Navier-Stokes system, as already shown in Section 2.6. In both cases, the range of Reynolds numbers $Re = 0.1,\ 1,\ 10,\ 100,\ 150$ will be considered. To validate the codes, the relative difference—computed using (102)—will be evaluated between the Stokes problem (*Sp*) and the steady Navier-Stokes problem (*sNSp*), and between the unsteady Navier-Stokes problem (*uNSp*) and the steady Navier-Stokes problem.
The concluding section will consider the *axisymmetric cylindrical duct case*, and we will analyze only the steady Navier-Stokes problem. At the moment, the accuracy in the analysis of the unsteady Navier-Stokes problem for this specific case is not as satisfactory as in the previous settings. At any rate, the considerations about the error evaluation are the same as in the previous case.

3.3.1 Non-symmetric duct case

The generalized Navier-Stokes problem as described in (115)-(118) will then be considered in the steady-state case (referred to again as sNSp), with its numerical solutions compared to those of the generalized Stokes problem (referred to as Sp). The comparison will be made only for the fundamental quantities, namely the velocity components u and v and the pressure p.
For brevity, it has been referred to as *Profile 1*:

$$h(x) = \frac{9}{10} + \frac{1}{10}\cos\left(\frac{\pi}{2}(x+1)\right), \quad \sigma(x) = \frac{3}{10} + \frac{2}{10}\cos\left(\frac{\pi}{2}(x+1)\right)$$

and *Profile 2*:

$$h(x) = \frac{9}{10} + \frac{1}{10}\cos\left(\frac{\pi}{2}(x+1)\right), \quad \sigma(x) = -0.3.$$

Re	u-relative error	v-relative error	p-relative error
0.1	$8.2 \cdot 10^{-3}$	$3.8 \cdot 10^{-2}$	$1.0 \cdot 10^{-2}$
1	$8.3 \cdot 10^{-2}$	$3.8 \cdot 10^{-1}$	$1.1 \cdot 10^{-1}$
10	$8.4 \cdot 10^{-1}$	3.3	1.1
100	10	10	$1.2 \cdot 10$
150	$1.7 \cdot 10$	$1.8 \cdot 10$	$2.1 \cdot 10$

Table 15: Relative error between sNSp and Sp
($\beta = 1,\ \delta = 0.1,\ \alpha = -1,\ p_{in} = 1,\ p_{out} = 0$):
Profile 1.

Re	u-relative error	v-relative error	p-relative error
0.1	$2.0 \cdot 10^{-2}$	$8.3 \cdot 10^{-1}$	$2.5 \cdot 10^{-2}$
1	$1.9 \cdot 10^{-1}$	8.1	$2.5 \cdot 10^{-1}$
10	1.9	$2.7 \cdot 10$	2.5
100	$1.5 \cdot 10$	$8.7 \cdot 10$	$1.9 \cdot 10$
150	$1.9 \cdot 10$	$8.8 \cdot 10$	$2.5 \cdot 10$

Table 16: Relative error between sNSp and Sp
($\beta = 1,\ \delta = 0.1,\ \alpha = -1,\ p_{in} = 1,\ p_{out} = 0$):
Profile 2.

It can be observed that as the Reynolds number increases, the *relative percentage difference* for the quantities considered between the solutions of sNSp and Sp increases considerably. This is always true regardless of the parameters considered, although for brevity, only the following parameters are considered here (and also later): $\beta = 1,\ \delta = 0.1,\ \alpha = -1,\ p_{in} = 1,\ p_{out} = 0$. Tables (17) and (18) below show the *relative error* between uNSp and sNSp for sufficiently long times, similarly to what was done in Section 2.6.

Re	T_f/ *dt*	u-relative error	v-relative error	p-relative error
0.1	1 / 0.02	$4.8 \cdot 10^{-3}$	$1.2 \cdot 10^{-1}$	$7.4 \cdot 10^{-3}$
1	1 / 0.02	$5.1 \cdot 10^{-3}$	$1.2 \cdot 10^{-1}$	$7.8 \cdot 10^{-3}$
10	10 / 0.1	$3.5 \cdot 10^{-3}$	$7.9 \cdot 10^{-2}$	$6.0 \cdot 10^{-3}$
100	100 / 0.5	$8.3 \cdot 10^{-3}$	$1.6 \cdot 10^{-1}$	$1.0 \cdot 10^{-2}$
150	150 / 0.5	$2.5 \cdot 10^{-2}$	$4.8 \cdot 10^{-1}$	$3.6 \cdot 10^{-2}$

Table 17: Relative error between uNSp and sNSp
($\beta = 1,\ \delta = 0.1,\ \alpha = -1,\ p_{in} = 1,\ p_{out} = 0$):
Profile 1.

Re	T_f/ *dt*	u-relative error	v-relative error	p-relative error
0.1	1 / 0.01	$3.7 \cdot 10^{-2}$	$3.6 \cdot 10^{-1}$	$2.1 \cdot 10^{-1}$
1	1 / 0.01	$3.1 \cdot 10^{-3}$	$4.5 \cdot 10^{-1}$	$1.7 \cdot 10^{-1}$
10	10 / 0.1	$1.0 \cdot 10^{-2}$	$5.7 \cdot 10^{-2}$	$1.2 \cdot 10^{-3}$
100	100 / 1	$1.0 \cdot 10^{-2}$	$1.4 \cdot 10^{-1}$	$2.5 \cdot 10^{-2}$
150	150 / 1	$2.3 \cdot 10^{-2}$	$1.6 \cdot 10^{-1}$	$4.6 \cdot 10^{-2}$

Table 18: Relative error between uNSp and sNSp
($\beta = 1,\ \delta = 0.1,\ \alpha = -1,\ p_{in} = 1,\ p_{out} = 0$):
Profile 2.

The following six figures show the time evolution of the velocity field and pressure in the cases of *Profile 1* and *Profile 2*, in analogy with what was done in Section 2.6.

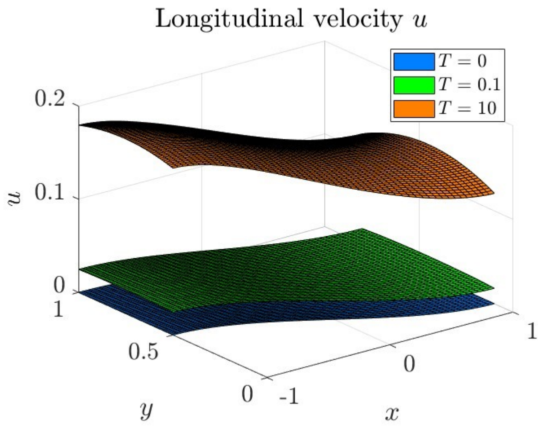

Figure 75: Profile 1: Temporal evolution of longitudinal velocity u. ($\beta = 1$, $\alpha = -1$, $p_{in} = 1$, $p_{out} = 0$, $\delta = 0.1$, $Re = 10$).

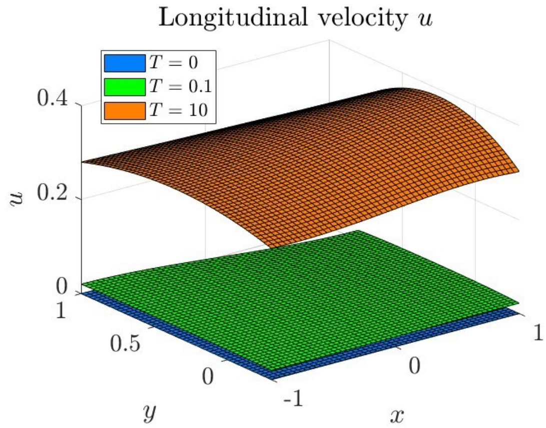

Figure 76: Profile 2: Temporal evolution of longitudinal velocity u. ($\beta = 1$, $\alpha = -1$, $p_{in} = 1$, $p_{out} = 0$, $\delta = 0.1$, $Re = 10$).

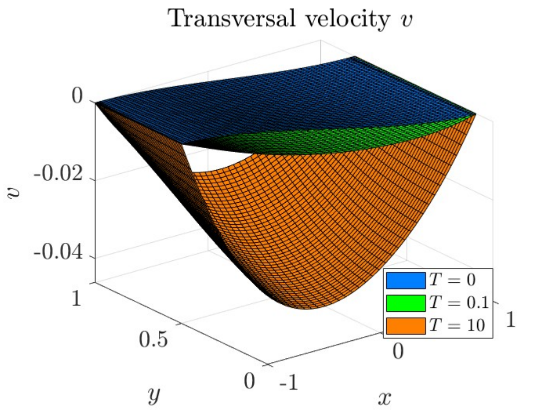

Figure 77: Profile 1: Temporal evolution of transversal velocity v. ($\beta = 1$, $\alpha = -1$, $p_{in} = 1$, $p_{out} = 0$, $\delta = 0.1$, $Re = 10$).

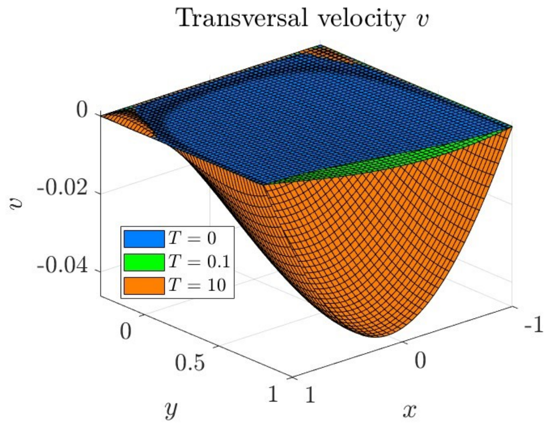

Figure 78: Profile 2: Temporal evolution of transversal velocity v. ($\beta = 1$, $\alpha = -1$, $p_{in} = 1$, $p_{out} = 0$, $\delta = 0.1$, $Re = 10$).

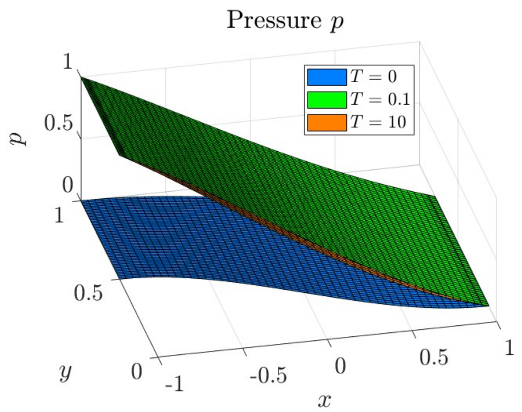

Figure 79: Profile 1: Temporal evolution of pressure p. ($\beta = 1$, $\alpha = -1$, $p_{in} = 1$, $p_{out} = 0$, $\delta = 0.1$, $Re = 10$).

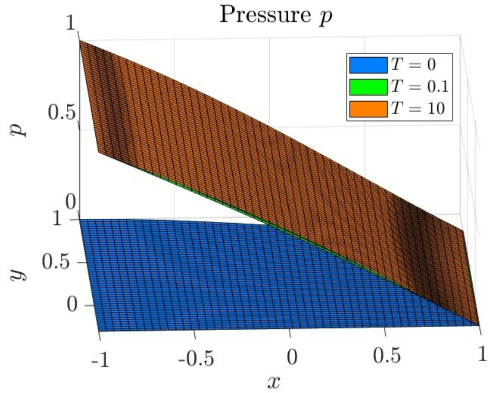

Figure 80: Profile 2: Temporal evolution of pressure p. ($\beta = 1$, $\alpha = -1$, $p_{in} = 1$, $p_{out} = 0$, $\delta = 0.1$, $Re = 10$).

3.3.2 Axisymmetric cylindrical channel case

The unsteady and non-linear version of equations (151)-(154) is presented below. As for the planar case we consider the comparison between the steady-state case (sNSp) and the Stokes problem (Sp). The general problem is given by

$$\begin{cases} Re\delta^3 r\big(v_t + vv_r + wv_z\big) = -rp_r + \delta r\big(S_{rr}\big)_r + \delta\big(S_{rr} - S_{\theta\theta}\big) + \delta^2 r\big(S_{rz}\big)_z, \\ \\ Re\delta r\big(w_t + vw_r + ww_z\big) = -rp_z + S_{rz} + r\big(S_{rz}\big)_r + \delta r\big(S_{zz}\big)_z, \\ \\ \big(rv\big)_r + rw_z = 0, \\ \\ S_{rr} = 2\mu\delta v_r, \qquad S_{rz} = \mu\big(w_r + \delta^2 v_z\big), \\ \\ S_{\theta\theta} = 2\mu v/r, \qquad S_{zz} = 2\mu\delta w_z, \end{cases} \tag{160}$$

with boundary conditions

$$\begin{cases} p = p_{in}, \quad v = 0, \quad \text{on} \;\; z = -1, \\ p = 0, \qquad v = 0, \quad \text{on} \;\; z = 1, \\ \\ \alpha\Big[\delta h_z\big(S_{zz} - S_{rr}\big) - S_{rz}\big(1 - \delta^2 h_z^2\big)\Big] + w\big(1 + \delta^2 h_z^2\big)^{\frac{3}{2}} = 0, \quad \text{on} \quad r = h(z), \\ w h_z - v = 0, \qquad\qquad\qquad\qquad\qquad\qquad\qquad\qquad \text{on} \quad r = h(z), \\ \\ w_r = 0, \quad v = 0, \quad \text{on} \;\; r = 0, \qquad \text{(symmetry)}. \end{cases} \tag{161}$$

We consider the following profiles:

$$\textit{Profile 1}: \qquad h(z) = \frac{9}{10} + \frac{1}{10}\cos\left(\frac{\pi}{2}(z+1)\right), \quad \sigma(z) = 0; \tag{162}$$

$$\textit{Profile 2}: \qquad h(z) = 1 + \frac{1}{5}\cos\left(z^2 - 1\right)^2, \quad \sigma(z) = 0. \tag{163}$$

Re	u-relative error	v-relative error	p-relative error
0.1	$3.1 \cdot 10^{-2}$	$3.5 \cdot 10^{-1}$	$3.1 \cdot 10^{-2}$
1	$3.1 \cdot 10^{-1}$	3.4	$3.1 \cdot 10^{-1}$
10	2.9	$2.6 \cdot 10$	3.0
100	$2.0 \cdot 10$	$4.3 \cdot 10$	$2.2 \cdot 10$
150	$2.6 \cdot 10$	$6.8 \cdot 10$	$2.8 \cdot 10$

Table 19: Relative error between sNSp and Sp
($\beta = 1, \; \delta = 0.1, \; \alpha = -1, \; p_{in} = 1, \; p_{out} = 0$):
Profile 1.

Re	u-relative error	v-relative error	p-relative error
0.1	$3.7 \cdot 10^{-3}$	$1.8 \cdot 10^{-1}$	$7.0 \cdot 10^{-2}$
1	$3.7 \cdot 10^{-2}$	1.7	$7.1 \cdot 10^{-2}$
10	$3.8 \cdot 10^{-1}$	$1.5 \cdot 10$	7.2
100	4.6	$6.9 \cdot 10$	$7.2 \cdot 10$
150	7.1	$1.0 \cdot 10^2$	$1.1 \cdot 10^2$

Table 20: Relative error between sNSp and Sp
($\beta = 1, \; \delta = 0.1, \; \alpha = -1, \; p_{in} = 1, \; p_{out} = 0$):
Profile 2.

Tables (19) and (20) qualitatively show the same results as Tables (15) and (16), namely that as the Reynolds number increases, the nonlinear term $\nabla v[v]$ becomes increasingly significant in equations $(160)_{1,2}$, and consequently in the solution of the problem itself.

4 Conclusions and Future Perspectives

In light of the results from the two previous sections, it can be asserted that, in the case of two-dimensional flows governed by a pressure gradient, both the Stokes problem and the generalized steady-state Navier-Stokes problem (i.e., with viscosity dependent on strain-rate tensor $\dot{\gamma}^*$, or on the pressure p^*) can be treated using spectral collocation methods (SCM). The case where the flow is confined in channels with symmetric walls proves to be simpler. In this case, it can be stated that the numerical errors, due to the numerous iterations especially related to the use of the Newton-Raphson method, are more contained than in the case of channels with non-symmetric walls or cylindrical geometry. The extension to the nonlinear case, where the term $\nabla\mathbf{v}[\mathbf{v}]$ is introduced, involves a further complication that the SCM nevertheless allow one to solve with good accuracy and quite quickly even on a common laptop. In this case, the differential problem is strongly nonlinear due to the viscosity ($\mu^* := \mu^*(\dot{\gamma}^*)$ or $\mu^* := \mu^*(p^*)$) and obviously because of the convective term.

Certainly, the analysis of the full time-dependent problem, including the term $\partial_t\mathbf{v}$, entails a significant complication: the nonlinear problem (due to the complex rheology of the fluid and the term $\nabla\mathbf{v}[\mathbf{v}]$) is compounded by the time discretization (solved using the Crank-Nicolson algorithm). This dual complication (essentially requiring, at each time step, a sufficient number of cycles with the Newton-Raphson algorithm to accurately solve the nonlinear differential problem) is still well handled by the SCM; however, the time evolution obviously requires longer code execution times (in any case never exceeding 55 seconds). The extension of the problem to the time-dependent case is well solved using the SCM when the channel profile is symmetric (see Section 2.6.1) or non-symmetric (see Section 3.3.1). The extension to the axisymmetric case using SCM is not yet sufficiently accurate and is, to date, still the subject of ongoing research. In all analyzed cases, it was observed that the optimal number of Gauss-Lobatto nodes is $N = 20$ along the two principal directions (thus totaling N^2 nodes on which the equations are projected). Indeed, even with $N = 25, 30, 35, 40$ or higher, the solution accuracy is not significantly affected, while convergence times ob-

viously increase progressively. Obviously, as with all numerical methods, it is important to consider the mathematical problem to be solved and consequently choose the most suitable numerical method. Nevertheless, from the present work, some useful insights can be drawn to understand when it may be advantageous to apply Spectral Collocation Methods. Indeed, for steady linear and nonlinear differential problems with even complex boundary conditions (see, for instance, Section 3), as long as they join smoothly, SCMs are certainly highly effective. Essentially, these methods allow the strong form of the problem to be directly solved, avoiding the need to complicate the formulation itself — a common issue in nonlinear problems solved, for example, using the finite difference method. Furthermore, planar domains, even with relatively intricate geometries, can be analyzed using codes that are not overly complex, yet still yield highly accurate results. Possible future developments of the present work could include the study of the generalized Navier-Stokes equations using higher performance methods for time integration (these approaches might address the time-dependent problem in the axisymmetric channel). Another extension could be considering domains with curved boundaries that can be mapped to a "pseudo-square." By exploiting the Gordon-Hall transformation (see [GH73], [QSS06]), it is always possible to map the domain to a square centered at the origin with a side length of 2. This would be necessary for a further conclusive extension, namely to consider complex domains that can be decomposed into subdomains of the "pseudo-square" type, each of which is mapped using the aforementioned Gordon-Hall transformation, and joined together while ensuring the continuity of the normal components of the various unknowns (see [TW04]).
The problems addressed thus far have considered apparent viscosities that depend either on the strain-rate tensor or on pressure. However, within the framework of Spectral Collocation Methods, it would be possible to investigate problems in which the viscosity depends simultaneously on both the strain-rate tensor and the pressure. A further extension could involve accounting for temperature-dependent viscosity, which, as stated in Section 1.7, has been assumed to be negligible. The analysis of the pressure and velocity fields in the aforementioned extensions could certainly be undertaken using SCM, provided that smooth bound-

ary conditions are prescribed, since the analytical formulation is expressed in strong form and discontinuous boundary conditions might be poorly handled by this numerical approach. It would also be of interest to explore the application of SCM to compressible fluids, given that, to the best of the author's knowledge, no results employing SCM are currently available in this context. Indeed, while numerous studies can be cited that have addressed this type of problem through numerical analysis based on the Finite Element Method (for instance see [ZTN15]) and, to a lesser extent yet still significantly, through Spectral Element Methods (see [CHQZ06] and [CQHZJ07])—both employing a weak-form approach—there appear to be no comparable results in the literature obtained using Spectral Collocation Methods (SCM).

5 Appendix

Here we report the components of the Jacobian matrix defined in (146). We write

$$\widehat{\dot{\beta}}_{N,i,j} = \frac{1}{\widehat{\dot{\gamma}}_{N,i,j}}, \qquad \widehat{\dot{\gamma}}_N = \left(\widehat{\dot{\gamma}}_{N,i,j}\right)_{i,j=1,\dots,(N+1)^2}, \tag{164}$$

$$\begin{gathered}
\frac{\partial \widehat{\mu}_N}{\partial \widehat{u}_N} = \left\{ \mathbb{1}_N \otimes_K \left[\delta^2 \frac{d\widehat{\mu}_N}{d\widehat{\dot{\gamma}}_N} \otimes_H \widehat{\dot{\beta}}_N \otimes_H \left(P_{1,N} \widehat{u}_N \right) \right] \right\} \otimes_H P_{1,N} + \\
\left\{ \mathbb{1}_N \otimes_K \left[\frac{d\widehat{\mu}_N}{d\widehat{\dot{\gamma}}_N} \otimes_H 4\widehat{\dot{\beta}}_N \otimes_H \left(P_{2,N} \widehat{u}_N + \delta^2 P_{1,N} \widehat{v}_N \right) \right] \right\} \otimes_H P_{2,N}, \\
\frac{\partial \widehat{\mu}_N}{\partial \widehat{v}_N} = \left\{ \mathbb{1}_N \otimes_K \left[\frac{d\widehat{\mu}_N}{d\widehat{\dot{\gamma}}_N} \otimes_H 4\delta^2 \widehat{\dot{\beta}}_N \otimes_H \left(P_{2,N} \widehat{u}_N + \delta^2 P_{1,N} \widehat{v}_N \right) \right] \right\} \otimes_H P_{1,N},
\end{gathered} \tag{165}$$

where $\otimes_H$ is the *Hadamard product* and $\otimes_K$ is the *Kronecker product*[5], and where

$$\begin{aligned}
&\mathbb{1}_N = [1, \dots, 1] \in \mathbb{R}^{1 \times (N+1)^2}, && \text{(unit row vector)}, \\
&\mathbb{I}_N \in \mathbb{R}^{(N+1)^2 \times (N+1)^2}, && \text{(identity matrix)}, \\
&\mathbb{O}_N \in \mathbb{R}^{(N+1)^2 \times (N+1)^2}, && \text{(null matrix)}.
\end{aligned} \tag{166}$$

The components (blocks) of the Jacobian are:

$$\begin{aligned}
&J_{12} = J_{13} = J_{16} = \mathbb{O}_N, \qquad J_{11} = \mathbb{I}_N, \\
&J_{14} = -2\delta \left[\frac{\partial \widehat{\mu}_N}{\partial \widehat{u}_N} \otimes_H \left(\mathbb{1}_N \otimes_K \left(P_{1,N} \widehat{u}_N \right) \right) + \left(\mathbb{1}_N \otimes_K \widehat{\mu}_N \right) \otimes_H P_{1,N} \right], \\
&J_{15} = -2\delta \left[\frac{\partial \widehat{\mu}_N}{\partial \widehat{v}_N} \otimes_H \left(\mathbb{1}_N \otimes_K \left(P_{1,N} \widehat{u}_N \right) \right) \right],
\end{aligned}$$

[5] If $A = (a_{i,j}),\ B = (b_{i,j}) \in \mathbb{R}^{m \times n}$ and $C = (c_{i,j}) \in \mathbb{R}^{p \times q}$, $A \otimes_H B = \sum_{\substack{i=1,\dots,n \\ j=1,\dots,m}} a_{i,j} b_{i,j} \mathbf{e}_i \otimes \mathbf{e}_j$ and $A \otimes_K C = (a_{i,j} C) \ \in \mathbb{R}^{mp \times nq}$.

$$J_{21} = J_{23} = J_{26} = \mathbb{O}_N, \qquad J_{22} = \mathbb{I}_N,$$
$$J_{24} = -\left[\frac{\partial\widehat{\mu}_N}{\partial\widehat{u}_N} \otimes_H \left(\mathbb{1}_N \otimes_K \left(P_{2,N}\widehat{u}_N + \delta^2 P_{1,N}\widehat{v}_N\right)\right) + (\mathbb{1}_N \otimes_K \widehat{\mu}_N) \otimes_H P_{2,N}\right],$$
$$J_{25} = -\left[\frac{\partial\widehat{\mu}_N}{\partial\widehat{v}_N} \otimes_H \left(\mathbb{1}_N \otimes_K \left(P_{2,N}\widehat{u}_N + \delta^2 P_{1,N}\widehat{v}_N\right)\right) + (\mathbb{1}_N \otimes_K \widehat{\mu}_N) \otimes_H \delta^2 P_{1,N}\right],$$

$$J_{31} = J_{32} = J_{36} = \mathbb{O}_N, \qquad J_{33} = \mathbb{I}_N,$$
$$J_{34} = -2\delta\left[\frac{\partial\widehat{\mu}_N}{\partial\widehat{u}_N} \otimes_H \left(\mathbb{1}_N \otimes_K \left(P_{2,N}\widehat{v}_N\right)\right)\right],$$
$$J_{35} = -2\delta\left[\frac{\partial\widehat{\mu}_N}{\partial\widehat{v}_N} \otimes_H \left(\mathbb{1}_N \otimes_K P_{2,N}\widehat{v}_N\right) + (\mathbb{1}_N \otimes_K \widehat{\mu}_N) \otimes_H P_{2,N}\right],$$

$$J_{43} = J_{44} = J_{45} = \mathbb{O}_N, \qquad J_{41} = \delta P_{1,N}, \qquad J_{42} = P_{2,N}, \qquad J_{46} = -P_{1,N},$$

$$J_{51} = J_{54} = J_{55} = \mathbb{O}_N, \qquad J_{52} = \delta^2 P_{1,N}, \qquad J_{53} = \delta P_{2,N}, \qquad J_{56} = -P_{2,N},$$

$$J_{61} = J_{62} = J_{63} = J_{66} = \mathbb{O}_N, \qquad J_{64} = P_{1,N}, \qquad J_{65} = P_{2,N}.$$

Below, the terms $J_{14},\ J_{15},\ J_{24},\ J_{25}$ are redefined with reference to the Section (2.6):

$$J_{14} = \delta Re\left\{\left[\mathrm{diag}\left(P_{1,N}\widehat{u}_N\right) + (\mathbb{1}_N \otimes_K \widehat{u}_N)\right] \otimes_H P_{1,N} + (\mathbb{1}_N \otimes_K \widehat{v}_N) \otimes_H P_{2,N}\right\},$$

$$J_{15} = \delta Re\ \mathrm{diag}\left(P_{2,N}\widehat{u}_N\right),$$

$$J_{24} = \delta^3 Re\ \mathrm{diag}\left(P_{1,N}\widehat{v}_N\right),$$

$$J_{25} = \delta^3 Re\left\{\left[\mathrm{diag}\left(P_{2,N}\widehat{v}_N\right) + (\mathbb{1}_N \otimes_K \widehat{v}_N)\right] \otimes_H P_{2,N} + (\mathbb{1}_N \otimes_K \widehat{u}_N) \otimes_H P_{1,N}\right\}.$$

Acknowledgments

For these three years spent in the field of scientific research in continuum mechanics, I would like to thank my supervisor, Prof. Lorenzo Fusi, without whom certainly nothing of what has been accomplished would have been possible. He has been a continuous support, always present and an inspiring source to follow, even when solutions to problems were slow to come or difficult to find. Furthermore, I can certainly say that, also on a personal level, he has always been exceptional and extraordinary, so much so that I can affirm that having built a friendship with him has perhaps been more important than the scientific results themselves.

A second thank you goes to my life partner, Sibilla, who has shown unlimited patience and tenacity. Having her by my side, solid and always present, has been a constant source of encouragement and admiration.

References

[AFS00] M Allouche, IA Frigaard, and G Sona. Static wall layers in the displacement of two visco-plastic fluids in a plane channel. *Journal of Fluid Mechanics*, 424:243–277, 2000.

[AM74] Giovanni Astarita and Giuseppe Marrucci. Principles of non-Newtonian fluid mechanics. 1974.

[And30] EN da C Andrade. The viscosity of liquids. *Nature*, 125(3148):309–310, 1930.

[And52] Edward Neville Da Costa Andrade. Viscosity of liquids. *Proceedings of the Royal Society of London. Series A. Mathematical and Physical Sciences*, 215(1120):36–43, 1952.

[Bar93] Carl Barus. Art. x.–isothermals, isopiestics and isometrics relative to viscosity. *American Journal of Science (1880-1910)*, 45(266):87, 1893.

[Bar97] Howard A Barnes. Thixotropy—a review. *Journal of Non-Newtonian fluid mechanics*, 70(1-2):1–33, 1997.

[BB87] R Byron Bird. Dynamics of polymetric liquids. *Kinetic Theory 2*, 1987.

[BBF+13] Daniele Boffi, Franco Brezzi, Michel Fortin, et al. *Mixed finite element methods and applications*, volume 44. Springer, 2013.

[BCM91] Christine Bernardi, Claudio Canuto, and Yvon Maday. Spectral approximations of the Stokes equations with boundary conditions on the pressure. *SIAM Journal on Numerical Analysis*, 28(2):333–362, 1991.

[BE80] Michel Bercovier and Michael Engelman. A finite-element method for incompressible non-Newtonian flows. *Journal of Computational Physics*, 36(3):313–326, 1980.

[BFS01] John T Bendler, John J Fontanella, and Michael F Shlesinger. A new Vogel-like law: Ionic conductivity, dielectric relaxation, and viscosity near the glass transition. *Physical Review Letters*, 87(19):195503, 2001.

[Bin22] Eugene Cook Bingham. *Fluidity and plasticity*. McGraw-Hill, 1922.

[BK03] Scott Bair and Peter Kottke. Pressure-viscosity relationships for elastohydrodynamics. *Tribology transactions*, 46(3):289–295, 2003.

[Bri31] Percy Williams Bridgman. The physics of high pressure. *(No Title)*, 1931.

[BW12] David V Boger and Kenneth Walters. *Rheological phenomena in focus*. Elsevier, 2012.

[Cas59] N Casson. Flow equation for pigment-oil suspensions of the printing ink-type. *Rheology of disperse systems*, pages 84–104, 1959.

[CB08] R Casalini and S Bair. The inflection point in the pressure dependence of viscosity under high pressure: A comprehensive study of the temperature and pressure dependence of the viscosity of propylene carbonate. *The Journal of Chemical Physics*, 128(8), 2008.

[CC89] MG Cawkwell and ME Charles. Characterization of canadian arctic thixotropic gelled crude oils utilizing an eight-parameter model. *J. Pipelines*, 7:251–264, 1989.

[CDKC21] Pierre J Carreau, Daniel CR De Kee, and Raj P Chhabra. *Rheology of polymeric systems: principles and applications*. Carl Hanser Verlag GmbH Co KG, 2021.

[CHQZ06] Claudio Canuto, M Youssuff Hussaini, Alfio Quarteroni, and Thomas A Zang. *Spectral methods: fundamentals in single domains*. Springer, 2006.

[CMWS58] Warren Gale Cutler, RH McMickle, W Webb, and RW Schiessler. Study of the compressions of several high molecular weight hydrocarbons. *The Journal of Chemical Physics*, 29(4):727–740, 1958.

[CN47] John Crank and Phyllis Nicolson. A practical method for numerical evaluation of solutions of partial differential equations of the heat-conduction type. In *Mathematical proceedings of the Cambridge philosophical society*, volume 43, pages 50–67. Cambridge University Press, 1947.

[CQHZJ07] Claudio Canuto, Alfio Quarteroni, M Yousuff Hussaini, and Thomas A Zang Jr. *Spectral methods: evolution to complex geometries and applications to fluid dynamics*. Springer, 2007.

[CR11] Raj P Chhabra and John Francis Richardson. *Non-Newtonian flow and applied rheology: engineering applications*. Butterworth-Heinemann, 2011.

[Den08] Morton M Denn. *Polymer melt processing: foundations in fluid mechanics and heat transfer*. Cambridge University Press, 2008.

[DM05] Konraad Dullaert and Jan Mewis. Thixotropy: Build-up and breakdown curves during flow. *Journal of Rheology*, 49(6):1213–1230, 2005.

[DM06] Konraad Dullaert and Jan Mewis. A structural kinetics model for thixotropy. *Journal of non-newtonian fluid mechanics*, 139(1-2):21–30, 2006.

[FF04] Lorenzo Fusi and Angiolo Farina. A mathematical model for Bingham-like fluids with visco-elastic core. *Zeitschrift für angewandte Mathematik und Physik ZAMP*, 55:826–847, 2004.

[FFR16] Lorenzo Fusi, Angiolo Farina, and Fabio Rosso. Squeeze flow of a Bingham-type fluid with elastic core. *International Journal of Non-Linear Mechanics*, 78:59–65, 2016.

[FFRR15] Lorenzo Fusi, Angiolo Farina, Fabio Rosso, and Sabrina Roscani. Pressure driven lubrication flow of a Bingham fluid in a channel: A novel approach. *Journal of Non-Newtonian fluid mechanics*, 221:66–75, 2015.

[FFRV22] Lorenzo Fusi, Angiolo Farina, Kumbakonam R Rajagopal, and Luigi Vergori. Channel flows of shear-thinning fluids that mimic the mechanical response of a Bingham fluid. *International Journal of Non-Linear Mechanics*, 138:103847, 2022.

[FG24a] Lorenzo Fusi and Antonio Giovinetto. A spectral collocation scheme for the flow of a piezo-viscous fluid in ducts with slip conditions. *Theoretical and Computational Fluid Dynamics*, 38:879–900, 2024.

[FG24b] Lorenzo Fusi and Antonio Giovinetto. A spectral collocation scheme for the two dimensional flow of a regularized viscoplastic fluid: Numerical results and comparison with analytical solution. *Mathematics and Computers in Simulation*, 225:1237–1256, 2024.

[FN05] IA Frigaard and Cherif Nouar. On the usage of viscosity regularisation methods for visco-plastic fluid flow computation. *Journal of non-newtonian fluid mechanics*, 127(1):1–26, 2005.

[FR04] IA Frigaard and DP Ryan. Flow of a visco-plastic fluid in a channel of slowly varying width. *Journal of Non-Newtonian fluid mechanics*, 123(1):67–83, 2004.

[G+94] Filippo Gazzola et al. On stationary Navier-Stokes equations with a pressure-dependent viscosity. In *Rendiconti Istituto Lombardo (Scienze) 128*. 1994.

[GA72] George Wheeler Govier and Khalid Aziz. *The flow of complex mixtures in pipes*, volume 469. Van Nostrand Reinhold Company New York, 1972.

[Gaz97] F Gazzolad. A note on the evolution Navier-Stokes equations with a pressure-dependent viscosity. *Zeitschrift für angewandte Mathematik und Physik ZAMP*, 48:760–773, 1997.

[GH73] William J Gordon and Charles A Hall. Construction of curvilinear coordinate systems and applications to mesh generation. *International Journal for Numerical Methods in Engineering*, 7(4):461–477, 1973.

[GS92] Filippo Gazzola and Paolo Secchi. *Some Results on Stationary Navier Stokes Equations with a Pressure Dependent Viscosity*. Dipartimento di Matematica, 1992.

[GW11] Roland Glowinski and Anthony Wachs. On the numerical simulation of viscoplastic fluid flow. In *Handbook of numerical analysis*, volume 16, pages 483–717. Elsevier, 2011.

[GWS58] Edward M Griest, Wayne Webb, and Robert W Schiessler. Effect of pressure on viscosity of higher hydrocarbons and their mixtures. *The Journal of Chemical Physics*, 29(4):711–720, 1958.

[HB26] Winslow H Herschel and Ronald Bulkley. Konsistenzmessungen von gummi-benzollösungen. *Kolloid-Zeitschrift*, 39:291–300, 1926.

[HB07] Kenneth R Harris and Scott Bair. Temperature and pressure dependence of the viscosity of diisodecyl phthalate at temperatures between (0 and 100) c and at pressures to 1 gpa. *Journal of Chemical & Engineering Data*, 52(1):272–278, 2007.

[Hei04] Wilhelm Heinrichs. Least-squares spectral collocation for the Navier–Stokes equations. *Journal of Scientific Computing*, 21:81–90, 2004.

[Hei06] Wilhelm Heinrichs. Least-squares spectral collocation with the overlapping Schwarz method for the incompressible Navier–Stokes equations. *Numerical Algorithms*, 43:61–73, 2006.

[Her26] WH Herschel. Measurement of consistency of rubber-benzene solutions. *Kolloid-zeitschrift*, 39:291–298, 1926.

[HG20] Raja R Huilgol and Georgios C Georgiou. A fast numerical scheme for the Poiseuille flow in a concentric annulus. *Journal of Non-Newtonian Fluid Mechanics*, 285:104401, 2020.

[HMNR03] Jaroslav Hron, Josef Málek, J Nečas, and KR Rajagopal. Numerical simulations and global existence of solutions of two-dimensional flows of fluids with pressure-and shear-dependent viscosities. *Mathematics and Computers in Simulation*, 61(3-6):297–315, 2003.

[HMR01] J Hron, J Málek, and KR Rajagopal. Simple flows of fluids with pressure–dependent viscosities. *Proceedings of the Royal Society of London. Series A: Mathematical, Physical and Engineering Sciences*, 457(2011):1603–1622, 2001.

[Hou81] M Houska. Engineering aspects of the rheology of thixotropic liquids. *D, Czech Technical University of Prague, Prague*, 1981.

[Hui15] Raja R Huilgol. *Fluid mechanics of viscoplasticity.* Springer, 2015.

[JG80] KL Johnson and JA Greenwood. Thermal analysis of an Eyring fluid in elastohydrodynamic traction. *Wear*, 61(2):353–374, 1980.

[JT77] KL Johnson and JL Tevaarwerk. Shear behaviour of elastohydrodynamic oil films. *Proceedings of the Royal Society of London. A. Mathematical and Physical Sciences*, 356(1685):215–236, 1977.

[KKJ90] DS Keller and DV Keller Jr. An investigation of the shear thickening and antithixotropic behavior of concentrated coal–water dispersions. *Journal of Rheology*, 34(8):1267–1291, 1990.

[KPG11] Anna Kalogirou, Stella Poyiadji, and Georgios C Georgiou. Incompressible Poiseuille flows of Newtonian liquids with a pressure-dependent viscosity. *Journal of Non-Newtonian Fluid Mechanics*, 166(7-8):413–419, 2011.

[Lar99] Ronald G Larson. The structure and rheology of complex fluids. 1999.

[MBM02] Ashutosh Mujumdar, Antony N Beris, and Arthur B Metzner. Transient phenomena in thixotropic systems. *Journal of Non-Newtonian Fluid Mechanics*, 102(2):157–178, 2002.

[Mew79] Joannes Mewis. Thixotropy-a general review. *Journal of Non-Newtonian Fluid Mechanics*, 6(1):1–20, 1979.

[Mor01] Faith A Morrison. Understanding rheology. *(No Title)*, 2001.

[MR07] J Málek and KR Rajagopal. Mathematical properties of the solutions to the equations governing the flow of fluids with pressure and shear rate dependent viscosities. *Handbook of mathematical fluid dynamics*, 4:407–444, 2007.

[NR11] KB Nakshatrala and KR Rajagopal. A numerical study of fluids with pressure-dependent viscosity flowing through a rigid porous medium. *International Journal for Numerical Methods in Fluids*, 67(3):342–368, 2011.

[Pap87] Tasos C Papanastasiou. Flows of materials with yield. *Journal of Rheology*, 31(5):385–404, 1987.

[PDGH18] Pandelitsa Panaseti, Yiolanda Damianou, Georgios C Georgiou, and Kostas D Housiadas. Pressure-driven flow of a Herschel-Bulkley fluid with pressure-dependent rheological parameters. *Physics of fluids*, 30(3), 2018.

[PDR99] M Paluch, Z Dendzik, and SJ Rzoska. Scaling of high-pressure viscosity data in low-molecular-weight glass-forming liquids. *Physical Review B*, 60(5):2979, 1999.

[PFM09] A Putz, IA Frigaard, and DM Martinez. On the lubrication paradox and the use of regularisation methods for lubrication flows. *Journal of Non-Newtonian fluid mechanics*, 163(1-3):62–77, 2009.

[PR77] Pasawadee Pradipasena and Chokyun Rha. Pseudoplastic and rheopectic properties of a globular protein (β-lactoglobulin) solution 1. *Journal of Texture Studies*, 8(3):311–325, 1977.

[QSS06] Alfio Quarteroni, Riccardo Sacco, and Fausto Saleri. *Numerical mathematics*, volume 37. Springer Science & Business Media, 2006.

[Raj06] Kumbakonam R Rajagopal. On implicit constitutive theories for fluids. *Journal of Fluid Mechanics*, 550:243–249, 2006.

[Ren86] Michael Renardy. Some remarks on the Navier-Stokes equations with a pressure-dependent viscosity: Somk remarks on the Navier-Stokes equations with a pressure-dependent viscosity. *Communications in Partial Differential Equations*, 11(7):779–793, 1986.

[Ren03] Michael Renardy. Parallel shear flows of fluids with a pressure-dependent viscosity. *Journal of non-Newtonian fluid mechanics*, 114(2-3):229–236, 2003.

[Sar16] Pierre Saramito. *Complex fluids*. Springer, 2016.

[Sch00] Theodore Schwedoff. La rigidité des fluides. *Rapports du Congrès intern. de Physique*, 1:478–486, 1900.

[Sch78] William Raymond Schowalter. *Mechanics of non-Newtonian fluids*. Pergamon, 1978.

[Sch94] Gebhard Schramm. *A practical approach to rheology and rheometry*. Haake Karlsruhe, 1994.

[SIC17] Lokendra P Singh, Bruno Issenmann, and Frédéric Caupin. Pressure dependence of viscosity in supercooled water and a unified approach for thermodynamic and dynamic anomalies of water. *Proceedings of the National Academy of Sciences*, 114(17):4312–4317, 2017.

[SK65] I Steg and D Katz. Rheopexy in some polar fluids and in their concentrated solutions in slightly polar solvents. *Journal of Applied Polymer Science*, 9(9):3177–3193, 1965.

[SR10] Shriram Srinivasan and KR Rajagopal. A note on the flow of a fluid with pressure-dependent viscosity in the annulus of two infinitely long coaxial cylinders. *Applied Mathematical Modelling*, 34(11):3255–3263, 2010.

[Sto80] GG Stokes. On the theories of the internal friction of fluids in motion, and of the equilibrium and motion of elastic solids. *Transactions of the Cambridge Philosophical Society*, 8, 1880.

[SW17] Pierre Saramito and Anthony Wachs. Progress in numerical simulation of yield stress fluid flows. *Rheologica Acta*, 56:211–230, 2017.

[TM83] R.I. Tanner and J.F. Milthorpe. Numerical simulation of the flow of fluids with yield stress. Proceedings of 3^{rd} international conference on numerical methods in laminar and turbulent flow. *Pineridge Press*, pages 680–690, 1983.

[TNTN04] Clifford Truesdell, Walter Noll, C Truesdell, and W Noll. *The non-linear field theories of mechanics*. Springer, 2004.

[TR00] Clifford Truesdell and Kumbakonam Ramamani Rajagopal. *An introduction to the mechanics of fluids*. Springer Science & Business Media, 2000.

[Tre00] Lloyd N Trefethen. *Spectral methods in MATLAB*. SIAM, 2000.

[TW98] Roger I Tanner and Kenneth Walters. *Rheology: an historical perspective*, volume 7. Elsevier, 1998.

[TW04] Andrea Toselli and Olof Widlund. *Domain decomposition methods-algorithms and theory*, volume 34. Springer Science & Business Media, 2004.

[VdG98] PS Van der Gulik. The linear pressure dependence of the viscosity at high densities. *Physica A: Statistical Mechanics and its Applications*, 256(1-2):39–56, 1998.

[YHM08] Zhen You, Raja Ramesh Huilgol, and E Mitsoulis. Application of the Lambert w function to steady shearing flows of the Papanastasiou model. *International Journal of Engineering Science*, 46(8):799–808, 2008.

[ZTN15] Olek C Zienkiewicz, Robert Leroy Taylor, and Perumal Nithiarasu. *The finite element method for fluid dynamics*, volume 6. Elsevier Amsterdam, The Netherlands, 2015.

[ZYN15] Iffat Zehra, Malik Muhammad Yousaf, and Sohail Nadeem. Numerical solutions of Williamson fluid with pressure dependent viscosity. *Results in Physics*, 5:20–25, 2015.